Università degli Studi di Roma "La Sapienza"
Facoltà di Ingegneria
Corso di Laurea in Ingegneria Elettronica

Tesi di Laurea

Time Transient Effects in Superconducting Magnets

Candidato:
Riccardo de Maria

Relatore: Prof. Luigi Palumbo
Correlatore: Univ.Doz. Dr.Ing. Stephan Russenschuck
Controrelatore: Prof. Fabrizio Frezza

Anno Accademico 2003/04

Università degli Studi di Roma "La Sapienza"
Facoltà di Ingegneria
Corso di Laurea in Ingegneria Elettronica

Tesi di Laurea

Effetti transitori nei magneti superconduttori

Candidato:
Riccardo de Maria

Relatore: Prof. Luigi Palumbo
Correlatore: Univ.Doz. Dr.Ing. Stephan Russenschuck
Controrelatore: Prof. Fabrizio Frezza

Anno Accademico 2003/04

Ai miei genitori
che mi hanno permesso
di firmare col mio nome
quel che è poco più del frutto
dei loro sforzi e sacrifici

Acknowledgement

I wish to thank my supervisors Stephan Russenschuck and Luigi Palumbo for having offered me the possibility to work at CERN and for their guide; Bernhard Auchmann and Andrea Mostacci for all the helpful discussions, advices, corrections during all my stay at CERN; Luca Bottura, Arian Verweij, Walter Scandale for the discussions, ideas and contributions that they offered me during my work; the Italian community and the other students at CERN for their logistic support and their company during all my stay in Geneva; my friends Lorenzo e Domenico for having been present when I was in need; all my friends in Rome who made my leave to Geneva easier; my friends of inCHIOSTROrosso for having given a public spirit to my last year at university; last, but no least my parents and my sisters for having borne me, better than aided, during my studies, without them I could not have brought my thesis to its conclusion; everyone that, for accident, I have forgot to mention to which, without a doubt, I owe part of my success, hoping I succeded in remedying my ingratitude with this last sentence.

Ringraziamenti

Vorrei ringraziare i miei supervisori Stephan Russenschuck e Luigi Palumbo per avermi offerto la possibilità di svolgere la mia tesi al CERN e per avermi guidato durante il mio lavoro; Bernhard Auchmann e Andrea Mostacci per le discussioni, consigli e correzioni; Luca Bottura, Arian Verweij e Walter Scandale per le discussioni, idee e contributi che hanno dato al mio lavoro; la "comunità" italiana e gli altri studenti del CERN per il loro supporto logistico nei primi mesi dal mio trasferimento e la compagnia durante tutta la mia permanenza a Ginevra; i miei amici Lorenzo e Domenico per essere stati presenti nel momento del bisogno; tutti i miei amici di Roma per aver reso più facile la mia partenza per Ginevra; gli amici di inCHIOSTROrosso per aver dato un valore civico ai miei ultimi anni di università; non ultimi i miei genitori e le mie sorelle che mi hanno sopportato, prima che aiutato, durante tutti i miei studi, senza di loro non avrei potuto firmare questa tesi; tutti quelli che per accidente ho scordato di menzionare a cui senz'altro devo parte dei miei risultati, sperando di poter rimediare alla mia ingratitudine con quest'ultima frase.

Contents

Capitolo 1

Sintesi

1.1 Introduzione

L'oggetto di questa tesi riguarda lo studio di alcuni effetti transitori dovuti al campo magnetico non costante nei magneti superconduttori, con particolare attenzione per i magneti per acceleratori di particelle, e la realizzazione di un codice numerico atto a simularli. Il lavoro è stato svolto presso il CERN (Conseil European pour la Recherché Nucleaire) di Ginevra, nell'ambito del progetto LHC (Large Hadron Collider).

Quando si vogliono raggiungere campi magnetici che vanno oltre la saturazione del ferro o quando si hanno requisiti di consumo di potenza e generazione di calore particolarmente stringenti, l'unica scelta possibile è l'uso dei magneti superconduttori.

Questo è il caso per i grandi acceleratori di particelle di ultima generazione come LHC, attualmente in costruzione al CERN. LHC è un sincrotrone, un particolare tipo di acceleratore circolare, costruito per far collidere due fasci di protoni. L'energia di centro di massa nominale che si vorrebbe raggiungere è di $14\,\mathrm{TeV}$. Forti campi magnetici sono usati per guidare e controllare il moto delle particelle e farli collidere.

La dinamica delle particelle si basa sull'applicazione della legge di Lorentz:

$$\boldsymbol{F} = qe(\boldsymbol{E} + \boldsymbol{v} \times \boldsymbol{B}), \tag{1.1.1}$$

dove e è la carica dell'elettrone e q è la carica della particella in unità della carica dell'elettrone.

Per curvare le particelle è necessario un campo magnetico ortogonale al piano dell'orbita che produce la necessaria forze centripeta per mantenere la traiettoria di progetto. Man mano che l'energia aumenta, prima la

velocità, poi la massa aumentano richiedendo una forza curvante sempre maggiore. La relazione che lega campo magnetico B, raggio dell'orbita r, momento $p = mv$, carica q è

$$Br[\,\mathrm{T\,m}] = .3356pq[\,\mathrm{GeV}/c]. \tag{1.1.2}$$

Si può vedere come il momento, quindi l'energia per particelle relativistiche, l'energia, a parità di raggio, dipende linearmente dal campo magnetico. Ecco quindi il motivo che lo rende uno dei parametri più importanti che caratterizzano l'acceleratore su cui sono concentrati i maggiori sforzi per massimizzarlo.

Dall'ultima relazione (1.1.2) si vede anche che se si vuole mantenere il raggio costante, man mano che le particelle guadagnano energia, si deve incrementare il campo magnetico. Un campo magnetico variabile da origine ad un campo elettrico il quale è fonte di correnti parassite all'interno dei materiali conduttori che costituiscono il magnete. Queste correnti producono perdite per effetto Joule e ulteriore campo magnetico che perturba il campo principale. Le perdite sono particolarmente deleterie perchè si verificano tra l'altro nei cavi superconduttori stessi che in genere contengono una percentuale di rame o altro conduttore normale. La generazione di calore e quindi l'aumento di temperatura sono una delle cause di perdita dello stato di superconduttività.

Quando il campo magnetico è giunto al massimo di solito viene mantenuto per il tempo necessario agli esperimenti con le particelle. A questo punto il campo elettrico si riduce a zero e le correnti parassite si attenuano fino a scomparire. Le correnti parassite sono dunque la causa di alcuni dei più importanti effetti transienti all'interno dei magneti superconduttori.

1.2 Superconduttività

La superconduttività è uno stato della materia che alcuni conduttori presentano a basse temperature [Mes96]. È caratterizzato dalla scomparsa della resistenza elettrica. Oltre alla temperatura lo stato di superconduttività dipende dalla densità di corrente presente e dal campo magnetico. Esistono due tipi di materiali superconduttori. Il tipo I non accetta campo magnetico al suo interno, al contrario del tipo II. Quest'ultimo quindi è il tipo a cui appartengo i materiali candidati per essere usati nei magneti. È possibile definire una superficie critica nelle variabili di stato T, B, J che separa la regione dove il materiale è supercondutore da quella in cui è un normale conduttore. Un magnete superconduttore deve far operare i cavi

superconduttori entro questa regione. Se anche localmente una regione del cavo perde la superconduttività, la corrente che prima non dissipava ora produce calore che riscalda le regioni circostanti. Si instaura una reazione a catena chiamata "quench" che molto rapidamente scalda tutto il magnete. Le correnti parassite possono provocare o, quanto meno, favorire l'insorgere di questo fenomeno. Il materiale usato per i cavi superconduttori è una lega NbTi. I cavi sono formati da "strands" arrotolati in modo da far assumere al cavo una sezione trapezoidale (cavo Rutherford). Ogni strand è formato da una gran numero di filamenti di NbTi, arrotolati anch'essi, immersi in una matrice di rame. La sua presenza è necessaria per garantire buone prestazione meccaniche, buona conduzione di calore e di corrente indispensabili per prevenire danni in caso di quench.

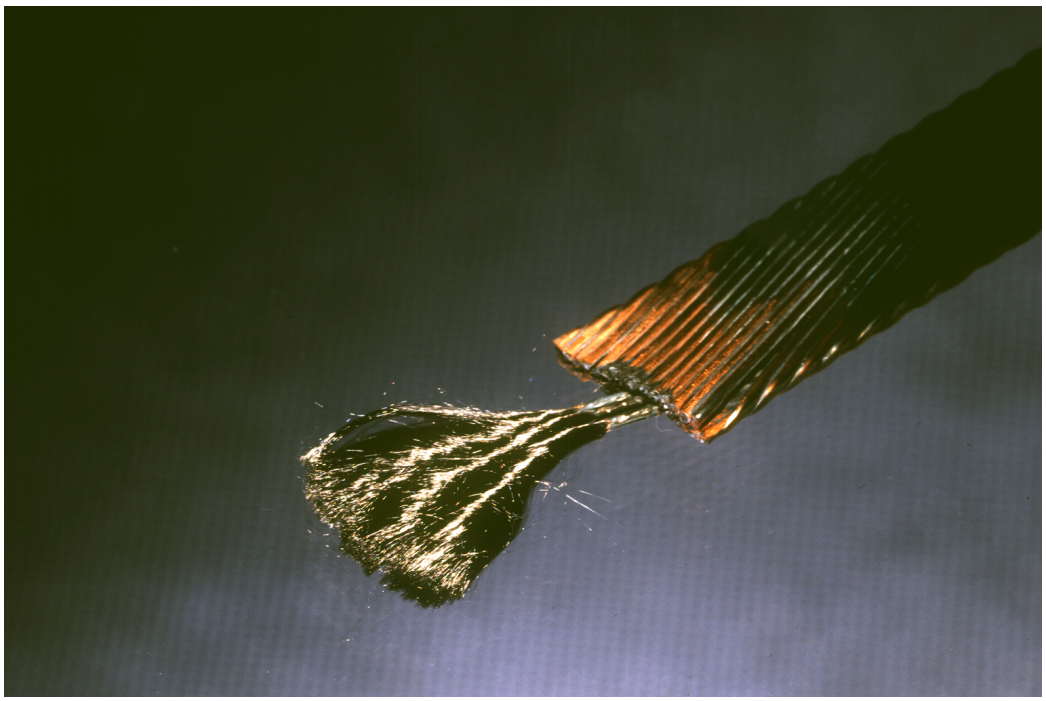

Figura 1.2.1 Strand e filamenti di un cavo superconduttore di tipo Rutherford.

La presenza di rame, proprio dove viene prodotto il campo magnetico, dà origine alle correnti parassite che provocano maggiori perdite, errori di campo e sono capaci di interferire con lo stato di superconduttività. Per questo motivo la capacità di simulare le correnti parassite è importante.

1.3 Diffusione magnetica

Tipicamente nei magneti per accelleratori le frequenze in gioco sono molto basse. Per esempio in LHC i magneti impiegano circa mezz'ora per passare dal campo all'iniezione delle particelle ($\approx 0\,\mathrm{T}$) a quello finale ($\approx 8\,\mathrm{T}$). La variazione di campo è dell'ordine dei $10\,\mathrm{mT/s}$. I cosiddetti "fast pulsed magnets" arrivano ai $4\,\mathrm{T/s}$. In queste condizioni, basse frequenze e alte conducibilità, il termine legato alla corrente di spostamento nelle equazioni di Maxwell può essere ignorato:

$$\nabla \times \boldsymbol{B} \approx \mu\sigma\boldsymbol{E}. \tag{1.3.1}$$

Questa approssimaione è chiamata magneto quasi statica. Una conseguenza è che le correnti sono solenoidali; un'altra è che le equazioni di Maxwell danno origine ad equazioni di diffusione.

1.4 Modello circuitale per il cavo Rutherford

Vista la complessità della struttura di un cavo Rutherford è comodo usare un approccio circuitale per discretizzare e risolvere il problema [Mor73]. L'approccio usato per modellizare gli elementi del circuito è conosciuto come PEEC (partial element equivalent circuit) [Rue74]. L'approssimazione magneto quasi statica ci porterà ad avere solo resistenze, induttanze e sorgenti di tensioni come elementi circuitali.

Nella figura 1.4.2 è rappresentato il circuito che modellizza una porzione di cavo.

Le resistenze modellizzano il rame all'interno degli strand superconduttori e i contatti tra gli strand. Per questo motivo queste correnti parassite sono chiamate anche "inter-strand coupling currents". Le induttanze modellizzano l'accoppiamento induttivo tra le correnti parassite, le sorgenti di tensione il contributo della variazione di flusso all'interno delle maglie nelle vesti dell'intelrale di linea del potenziale vettore su ogni ramo.

Le resistenze sono un dato del problema. La loro modellizzazione è particolarmente difficile in quanto dipendono essenzialmente dall'ossido di rame che si forma all'esterno degli strand difficile da controllare. Inoltre quando assemblati nei magneti i cavi subiscono deformazioni che variano i maniera non prevedibile e non riproducibile le superfici di contatto, variando dunque la resistenza anche di un ordine di grandezza nello stesso cavo di uno stesso magnete. Per questo motivo vengono assunte note o al più vengono lasciate variare casualmente.

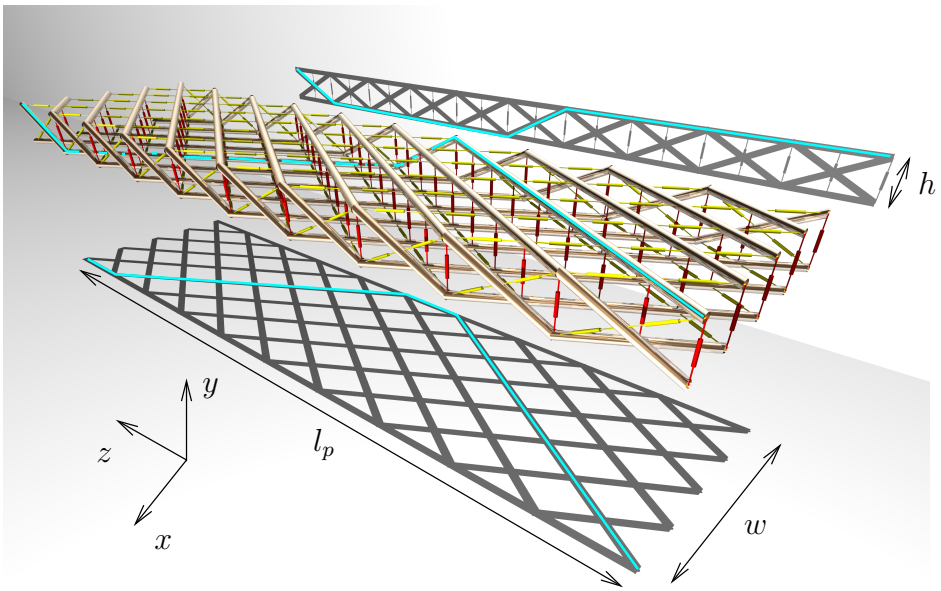

Figura 1.4.2 Modello circuitale di una porzione di un cavo Rutherford di 10 strand. In giallo e rosso sono rappresentate le resistenze, mentre i tubi argentati rappresentano gli strand superconduttori. La linea azzurra evidenzia il periodo di torsione del cavo.

Le induttanze auto e mutue vengono modellizate utilizzando la formula:

$$L_{ij} = \frac{\mu}{4\pi}\frac{1}{S_i S_j}\int_{V_i}\int_{V_j}\frac{\boldsymbol{w}_i \cdot \boldsymbol{w}_j}{r_{ij}} dV_i dV_j, \tag{1.4.1}$$

dove V_i, V_j sono i volumi dei conduttori, S_i, S_j sono le superfici attraverso le quali scorre la corrente, r_{ij} la distanza tra i punti dei conduttori, $\boldsymbol{w}_i$, $\boldsymbol{w}_j$ i versori direzione della densità di corrente.

Per le autoinduttanze i rami sono assunti rettilinei a sezione circolare. È stata ricavata una espressione approssimata della formula precedente, a differenza di quelle presenti in letteratura [Gro46] è semplice ed è accurata anche quando la lunghezza del conduttore è piccola in confronto al raggio:

$$\begin{aligned} L &= \frac{\mu}{4\pi} 2l \left[\log\left(\frac{l}{d} + \sqrt{1+\frac{l^2}{d^2}}\right) - \sqrt{1+\frac{d^2}{l^2}} + \frac{d}{l}\right], \\ d &= Kr, \\ K &= 0.7788 - \frac{0.123178}{l/r + 0.6283}, \end{aligned} \tag{1.4.2}$$

dove l è la lunghezza del condurrore e r è il raggio.

Per le mutue induttanze è stata usata una approssimazione più grossolana:

$$L_{ij} = \frac{\mu}{4\pi} \frac{l_i l_j (\boldsymbol{w}_i \cdot \boldsymbol{w}_j)}{\langle r_{ij} \rangle}, \tag{1.4.3}$$

dove si è usato il fatto che per conduttori lontani l'integrano della formula (1.4.1) non varia molto e quindi:

$$\frac{1}{V_i V_j} \int_{V_i} \int_{V_j} \frac{1}{r_{ij}} dV_i dV_j = \left\langle \frac{1}{r_{ij}} \right\rangle \approx \frac{1}{\langle r_{ij} \rangle}. \tag{1.4.4}$$

Il motivo è il loro alto numero che rende necessario un modo computazionalmente veloce per rendere i tempi di calcolo ragionevoli.

1.5 Evidenze sperimentali delle correnti parassite

L'effetto delle correnti parassite è facilmente misurabile nei magneti superconduttori. Si trovano infatti perdite e errori di campo correlati linearmente con la variazione di campo. Si osservano inoltre modulazioni del campo lungo l'asse longitudinale dal periodo compatibile con la lunghezza di arrotolamento, detto twist pitch, nonostante la struttura sia omogenea lungo tale direzione. Il motivo è che a causa di imperfezioni e a causa della presenza di conduttori a resistenza nulla, vengono eccitate correnti parassite anche molto elevate che scorrono prevalentemente negli strand superconduttori. Queste correnti non sono responsabili di perdite apprezzabile e anche gli errori di campo che generano, essendo a media nulla lungo l'asse principale, non disturbano la dinamica delle particelle. Tuttavia sono in grado di far superare localmente la corrente critica provocando l'insorgere prematuro dei quench. Inoltre interagiscono con le correnti persistenti dei filamenti supercondoduttori il cui comportamento non lineare, produce un effetto non più a media nulla (fenomeno del decay e snapback).

Le scale temporali in cui le correnti agiscono variano dai secondi per le correnti che producono più perdite e scorrono nel rame, ai giorni per quelle che scorrono prevalentemente nei supercoduttori.

1.6 Analisi del circuito

Il circuito che modellizza il cavo (vedi figura 1.4.2) è analizzato su base maglie. L'approccio usato è completamente matriciale [Kam98]. La relazioni

costitutive possono essere scritte come:

$$\mathcal{V} = \mathcal{R}\mathcal{I} + \mathcal{L}\frac{\partial}{\partial t}\mathcal{I} + \mathcal{U}, \tag{1.6.1}$$

dove $\mathcal{V}$ è il vettore delle tensioni, $\mathcal{R}$ è la matrice delle resistenze, $\mathcal{I}$ è il vettore delle correnti, $\mathcal{U}$ il vettore delle sorgenti di tensione.

Si può definire una matrice delle maglie $\mathcal{M}$ tale che:

$$\mathcal{M}_{ab} = \begin{cases} 1 & \text{se il ramo } b \text{ appartiene alla maglia } a \text{ con lo stesso verso,} \\ -1 & \text{se il ramo } b \text{ appartiene alla maglia } a \text{ con il verso opposto,} \\ 0 & \text{altrimenti.} \end{cases} \tag{1.6.2}$$

La matrice $\mathcal{M}$ permette il passaggio dal vettore delle correnti dei nodi $\mathcal{I}$ a quello delle correnti di maglia $\mathcal{I}_M$ infatti:

$$\begin{aligned} \mathcal{I} &= \mathcal{M}^T\mathcal{I}_M, \\ \mathcal{I}_M &= \mathcal{M}\mathcal{I}. \end{aligned} \tag{1.6.3}$$

Inoltre può essere usato per esprime la legge di Kirchoff alle tensioni:

$$\mathcal{M}\mathcal{V} = 0. \tag{1.6.4}$$

Usando queste relazioni si giunge al sistema per le correnti di maglia. Per l'analisi a regime:

$$\mathcal{M}\mathcal{R}\mathcal{M}^T\mathcal{I}_M + \mathcal{M}\mathcal{U} = 0. \tag{1.6.5}$$

Per l'analisi transitoria può essere scritta l'equazione:

$$\mathcal{R}_M\mathcal{I}_M + \mathcal{L}_M\frac{\partial}{\partial t}\mathcal{I}_M + \mathcal{U}_M = 0, \tag{1.6.6}$$

dove

$$\begin{aligned} \mathcal{R}_M &= \mathcal{M}\mathcal{R}\mathcal{M}^T, \\ \mathcal{L}_M &= \mathcal{M}\mathcal{L}\mathcal{M}^T, \\ \mathcal{U}_M &= \mathcal{M}\mathcal{U}. \end{aligned} \tag{1.6.7}$$

Il metodo trapezoidale è usato per integrare l'equazione differenziale ottenendo:

$$\begin{aligned} \mathcal{M}\left(\mathcal{R} + \frac{2}{h}\mathcal{L}\right)\mathcal{M}^T\mathcal{I}_M(k+1) = \\ -\mathcal{M}\left(\mathcal{R} - \frac{2}{h}\mathcal{L}\right)\mathcal{M}^T\mathcal{I}_M(k) - \mathcal{M}\mathcal{U}(k) - \mathcal{M}\mathcal{U}(k+1). \end{aligned} \tag{1.6.8}$$

Il termine di sorgente è calcolato dal potenziale vettore conosciuto su ogni nodo. L'integrale sul ramo è ottenuto assumendo che vari linearmente tra un nodo e l'altro, dunque il valore dell'integrale è approssimato alla media del potenziale vettore sui due nodi moltiplicato scalarmente per il vettore del ramo:

$$\int \boldsymbol{A} \cdot \boldsymbol{dl} \approx \frac{\boldsymbol{A}_n + \boldsymbol{A}_{n+1}}{2} \cdot (\boldsymbol{r}_{n+1} - \boldsymbol{r}_n). \tag{1.6.9}$$

Usando l'approccio matriciale è agevole effettuare una analisi spettrale delle soluzioni, sia nel caso a regime sia in quello transitorio.

Nel caso a regime il sistema (1.6.5) può essere scritto come:

$$\begin{aligned} \mathcal{I}_M &= -(\mathcal{M}\mathcal{R}\mathcal{M}^T)^{-1}\mathcal{M}\mathcal{U} \\ \mathcal{I} &= -\mathcal{M}^T\mathcal{R}_M^{-1}\mathcal{U}_M, \end{aligned} \tag{1.6.10}$$

dove $\mathcal{R}_M = \mathcal{M}\mathcal{R}\mathcal{M}^T$ e $\mathcal{U}_M = \mathcal{M}\mathcal{U}$.

La matrice $\mathcal{R}_M$ può essere diagonalizzata:

$$\mathcal{R}_M = \mathcal{D}\mathcal{R}_D\mathcal{D}^{-1}, \tag{1.6.11}$$

dove $\mathcal{D}$ è la matrice della trasformazione e $\mathcal{R}_D$ è la matrice diagonalizzata.

Gli autovettori $\mathcal{P}_\lambda$ relativi all'autovalore r_λ sono una combinazione lineare di correnti di maglie, dunque sono una soluzione del sistema e possono essere scritti in termini delle correnti dei rami tramite:

$$\mathcal{Q}_\lambda = \mathcal{M}^T\mathcal{P}_\lambda. \tag{1.6.12}$$

Il vettore $\mathcal{Q}_\lambda$ rappresenta un modo del sistema ed è chiamato auto-maglia.

Ogni soluzione del sistema può essere scritto come:

$$\mathcal{I} = -\sum_\lambda \frac{u_\lambda}{r_\lambda}\mathcal{Q}_\lambda, \tag{1.6.13}$$

dove u_λ è il termine di eccitazione relativo all'autovalore r_λ e al modo $\mathcal{Q}_\lambda$. Questi termini possono essere calcolati usando:

$$\mathcal{U}_D = \mathcal{D}^T\mathcal{M}\mathcal{U}, \tag{1.6.14}$$

dove il vettore $\mathcal{U}_D$ contiene tutti i termini u_λ.

Per il caso transitorio è interessante diagonalizzare la matrice responsabile delle costanti di tempo. Infatti il sistema (1.6.10) ha come soluzione analitica [Akh98]

$$\mathcal{I}_M = (\mathcal{E} - e^{\mathcal{L}_M^{-1}\mathcal{R}_M t})\mathcal{R}_M^{-1}\mathcal{U} = \left(\mathcal{E} - \sum_{\lambda} \exp(w_\lambda t) \prod_{\lambda \neq \lambda'} \frac{\mathcal{W} - w_\lambda \mathcal{E}}{w_{\lambda'} - w_\lambda}\right) \mathcal{R}_M^{-1}\mathcal{U}, \tag{1.6.15}$$

dove $\mathcal{W} = \mathcal{L}_M^{-1}\mathcal{R}_M$ i cui autovalori w_λ rappresentano l'inverso delle costanti di tempo.

Due tipi di condizioni al contorno possono essere applicate al cavo. La prima considera il cavo tagliato alle estremità, la seconda permette di considerare un cavo infinitamente lungo imponendo che le correnti alle estremità di una porzione di cavo siano identiche. Queste ultime condizioni sono chiamate condizione spaziali al contorno periodiche.

1.7 Risultati numerici

Il codice sviluppato è piuttosto generale e permette l'analisi di cavi Rutherford di dimensioni e numero di strand arbitrari. Il codice può analizzare più cavi contemporaneamente includendo la loro interazione e è stato integrato in ROXIE [Rus99], un ambiente integrato per la simulazione, il progetto e l'ottimizzazione di magneti superconduttori per acceleratori. Questo permette l'analisi di correnti parassite direttamente durante il processo di progettazione e ottimizzazione.

Come esempi sono stati analizzati casi 2D, 3D, analisi transitoriore e a regime, su singolo cavo o all'interno di magneti, effetti aleatori e analisi spettrali.

Per 2D si intende lo studio della più piccola porzione di cavo possibile usando condizione spaziali a contorno periodiche. Questa analisi permette di studiare le correnti a basse costanti di tempo e ad alta dissipazione. In queste condizioni sono state effettuate analisi a regime, transitorie (figura 1.7.3), effetti aleatori per il singolo cavo e a regime per un intero magnete (figura 1.7.4).

Per 3D si intende l'analisi di un cavo di una certa lunghezza (figure 1.7.5), in questa situazione è stata effettuata una analisi transitoria e spettrale senza condizioni spaziali a contorno periodiche e un analisi spettrale con condizioni spaziali a contorno periodiche.

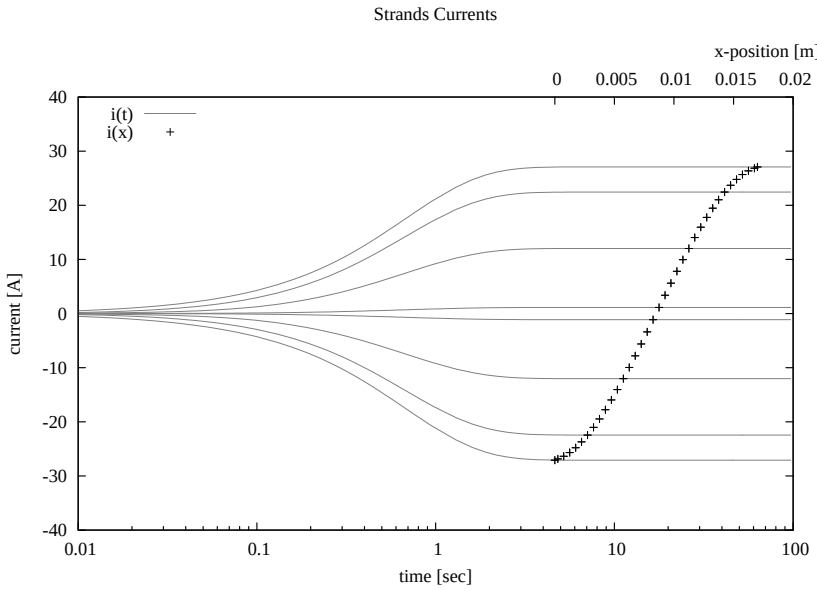

Figura 1.7.3 Evoluzione temporale della corrente negli strand di un cavo Rutherford dovuto ad una variazione del campo magnetico.

1.8 Implementazione

L'alto numero di rami per casi pratici impone l'utilizzo di codice particolarmente ottimizzato. L'esistenza di diverse scale temporali impone la necessità di poter variare l'intervallo temporale tra uno step all'altro.

Tutte le matrici sono sparse, l'unica matrice non sparsa, quella delle induttanze, è resa sparsa trascurando i termini piccoli. Le matrici sono registrate in modo particolare per evitare di usare memoria per gli elementi nulli. Le matrici delle resistenze e delle induttanze non sono memorizzate, ma sono funzioni. Le moltiplicazioni tra matrici sono realizzati tramite algoritmi adattati alla loro struttura. Il sistema lineare è risolto usando la decomposizione LU, tramite un codice open source (SuperLU [XD98]) ottimizzato per matrici sparse. La decomposizione della matrice è effettuata solo quando serve, in particolare quando cambia l'intervallo di tempo e il contributo delle induttanze cambia.

1.9 Conclusioni

In questa tesi è mostrato uno studio su alcuni effetti transitori dovuti alle coerenti parassite all'interno dei magneti superconduttori che usano un

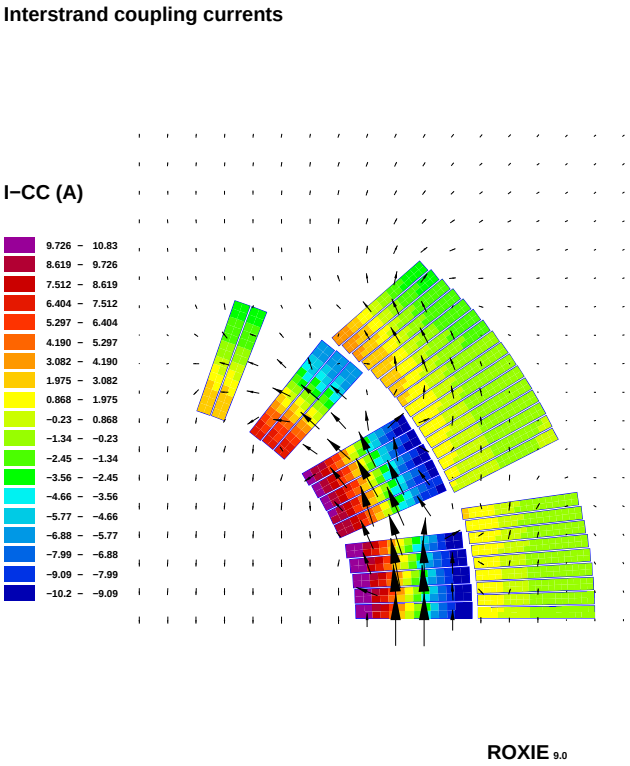

Figura 1.7.4 Correnti parassiti e campo prodotto in un dipolo durante una rampa di corrente.

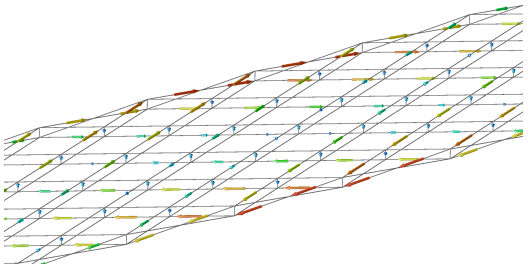

Figura 1.7.5 Dettaglio delle correnti parassite in un campione di cavo superconduttore soggetto ad una variazione di campo magnetico.

cavo Rutherford. Un codice generale è stato sviluppato per lo studio degli effetti sul singolo cavo e nei magneti grazie all'integrazione col programma ROXIE. Alcuni esempi sono stati sviluppati, ma non esaurisco le possibilità del codice. Infatti sarà possibile studiare l'interazione delle correnti parassite con la magnetizzazione dei cavi o le dinamica delle correnti ai bordi del magnete dove gli avvolgimenti hanno una complessa disposizione nello spazio. L'uso di questo codice potrà essere usato durante il processo di progettazione di nuovi magneti e la validazione con i risultati sperimentali dei modelli usati per descrivere i magneti.

Chapter 2

Introduction

The subject of this thesis is the study of time transient effects in superconducting magnets, with applications to accelerator magnnets, and the development of a software code in order to simulte them. The work has been performed at CERN (Conseil European pour la Recherché Nucleaire) at Geneva, in the LHC project.

2.1 Large Hadron Collider

The Large Hadron Collider (LHC), presently in construction at CERN, the European Organisation for Nuclear Research near Geneva (Switzerland), will be upon its completion the world's most advanced high-energy physics tool. The LHC basically consists of two interleaved synchrotrons, 26.7km in circumference, accelerating and bringing into collision two intense counter-rotating beams of protons, at a centre-of-mass energy of 14 TeV and a luminosity (rate of interaction per unit cross-section) of $10^{34}/\text{cm}^2\text{s}$. The LHC will also be able to collide heavy ions, such as lead ions, up to an energy level of about 1100 TeV. These collisions are estimated to cause phase transition of nuclear matter into quark-gluon plasma as it existed around 10^{-6} seconds after the Big Bang. Two large detectors, ATLAS (A Toroidal LHC Apparatus) and CMS (Compact Muon Solenoid), will detect and record the results of these collisions. Together with ALICE and LHC-b, 4 experiments will be located around the accelerator, all equipped with large particle detector.

The LHC will be installed in the existing tunnel of the Large Electron Positron Collider (LEP), see figure 2.1.1. LHC and LEP are both synchrotrons, in which the particle beam is held in a circular orbit by more than one thousand dipole magnets, see figure 2.1.2. The guiding field in-

creases with the particle energy as to keep the orbit stationary. The maximum energy of the leptons accelerated in LEP is limited to about 100 GeV due to synchrotron radiation emitted as the loaded particles are bent into a circular path. For the heavier protons, synchrotron radiation only occurs at much higher energies, and therefore the maximum energy is limited by the field in the dipole magnets. Using superconducting magnets with a nominal field of 8.33 T will allow the storage of proton beams with an energy of up to 7 TeV per beam, with the bending radius given by the existing LEP tunnel. To produce the anti-parallel fields required for bending the counter-rotating beams along their paths in the tunnel, the collider needs two separate magnetic channels. In the LHC dipoles (see picture 2.1.3), two sets of windings are combined in a common mechanical and magnetic structure to constitute twin-aperture magnets, a more compact and efficient solution, as the return flux of one aperture contributes to increasing the field in the other.

The LHC will make use of the existing injector chain (see figure 2.1.4). The beams will be injected into the LHC from the SPS at an energy of 450 GeV and be accelerated to 7 TeV in about 30 minutes.

The pre-accelerators are operational and the modifications required to achieve the LHC beam parameters will be finished before the LHC comes into operation. The civil engineering for the LHC is limited to the construction of two large underground caverns for the ATLAS and CMS experiments, and the two transfer tunnels (each 2.5 km long) from the SPS to the LHC.

2.2 Motivation

The absence of electrical resistance in the superconducting coil and the fact that they can produce magnetic field greater than normal conducting magnets (limited by the iron saturation) is the main reason of their use for particle accelerators. In particular in synchrotrons they are the main component that limits the maximum energy reachable. In fact particles are guided by a magnetic field in order to follow a close circle orbit and accelerated by an electric field in order to increase their energy. More the particle gains in energy, higher is the magnetic field necessary to make particles follow the same path.

For storing particle for long time it is necessary to produce a magnetic field whose relative deviation from the ideal field is in the order of 10^{-4}. A great effort is needed in order to control every effects that can damage field quality.

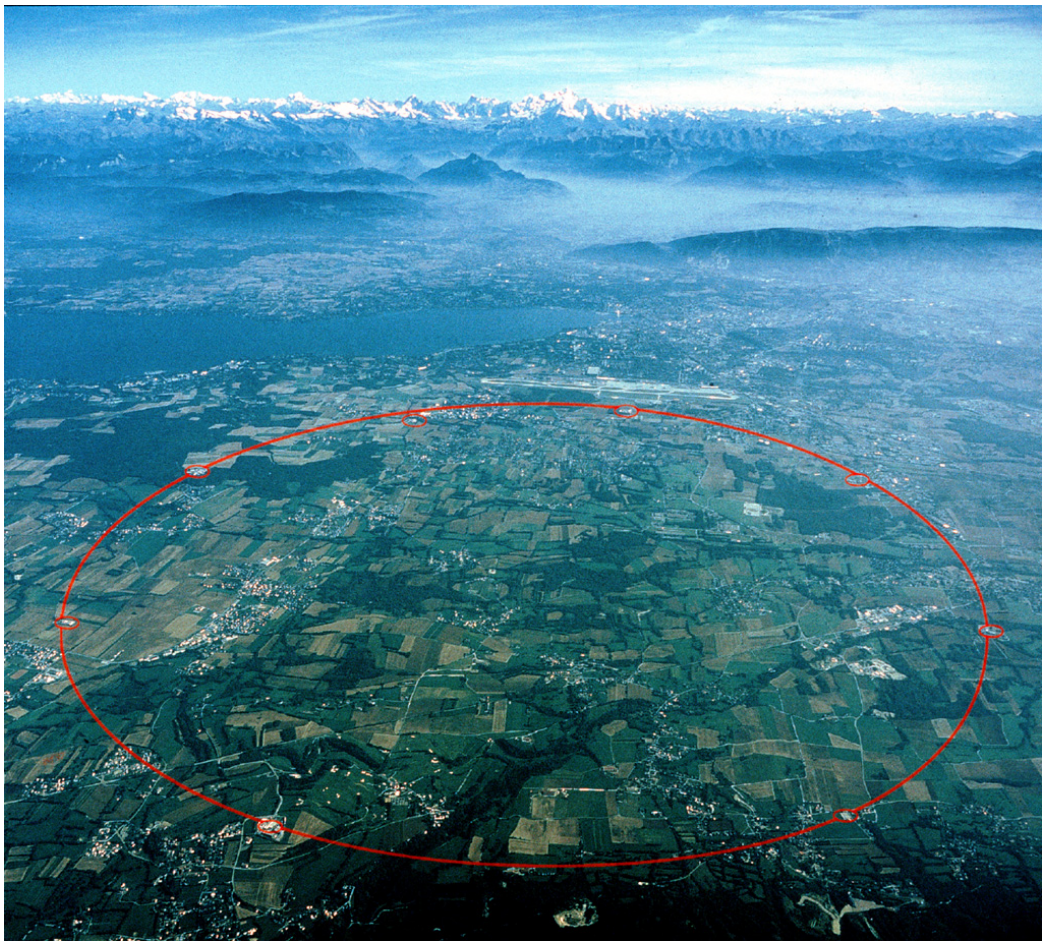

Figure 2.1.1 Aerial view of CERN site. Path of LEP/LHC tunnel is highlighted.

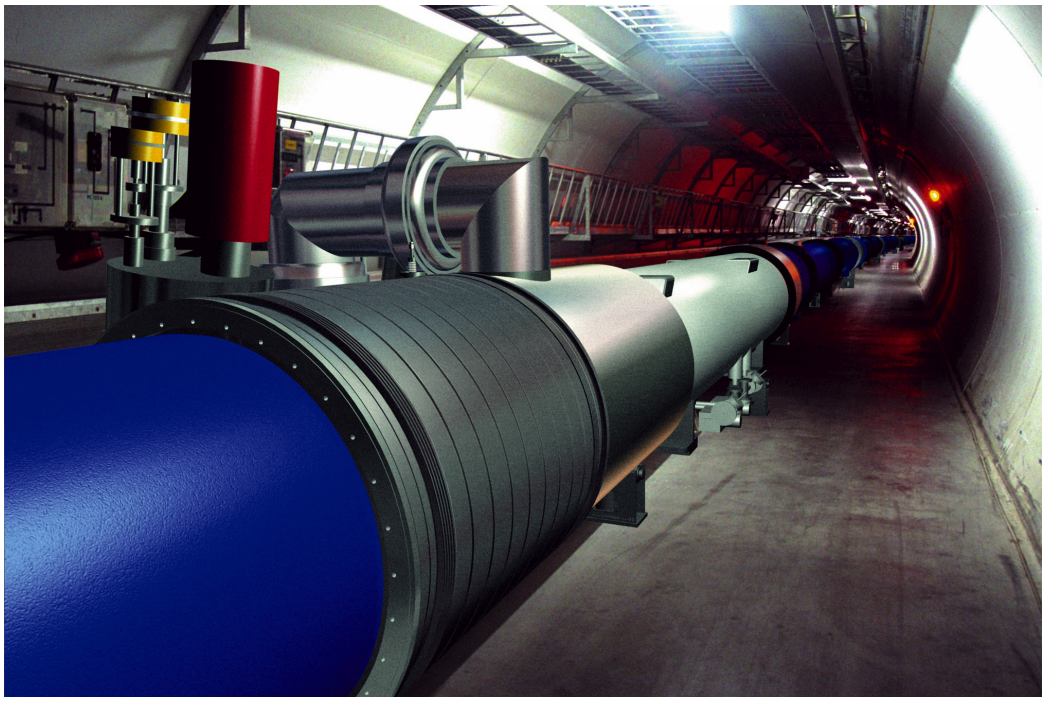

Figure 2.1.2 View of LHC tunnel once finished.

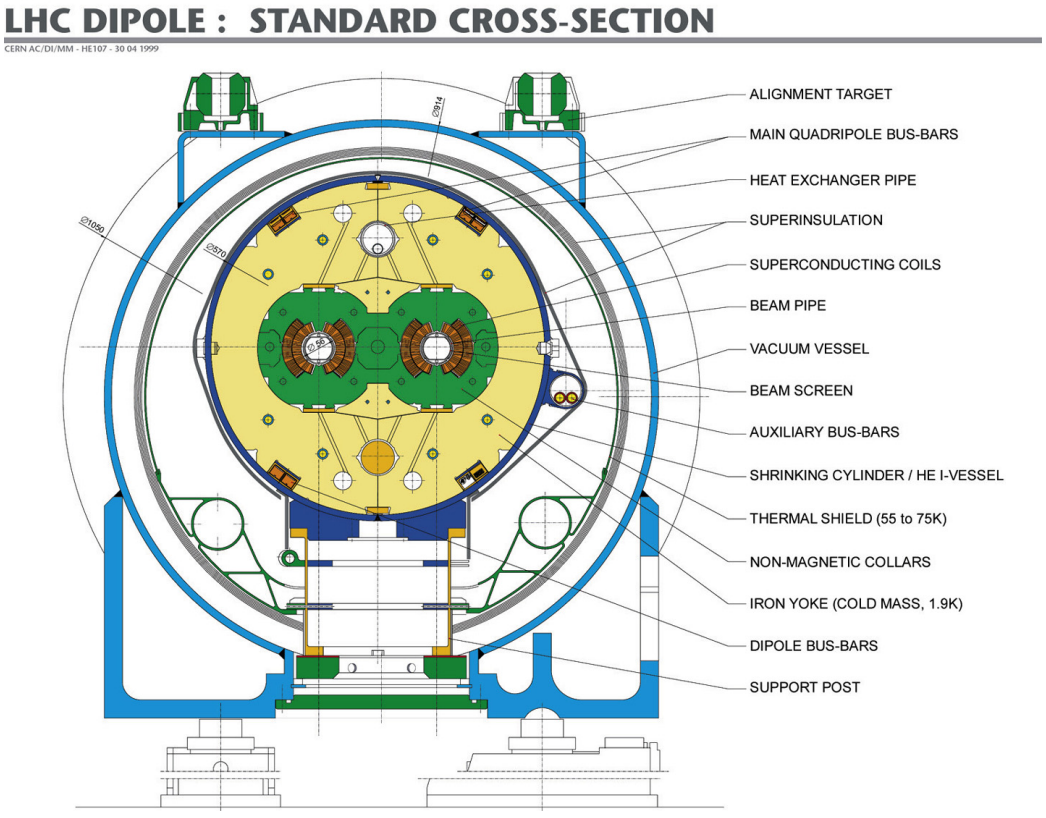

Figure 2.1.3 Cross section scheme of LHC dipole.

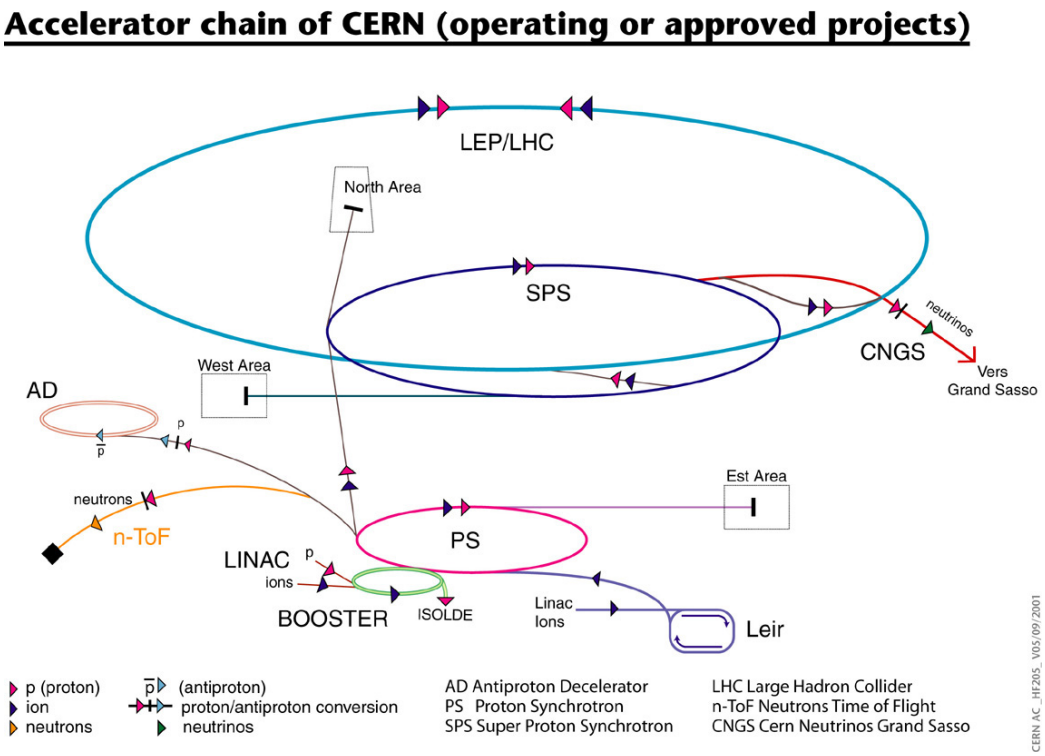

Figure 2.1.4 CERN accelerators chain.

In synchrotrons the magnetic field has to follow the time variation of accelerated particle that is, in the first approximation linear, thus it is important to control field quality during ramping (see figure 2.3.6. During this period errors are different from the steady state case, change with time and depend on the ramp rate and the previous excitation of the magnet. The main sources of these errors are eddy currents generated by the time-varying magnetic field, in particular inside superconducting cable, where resistivity is lower than the other parts.

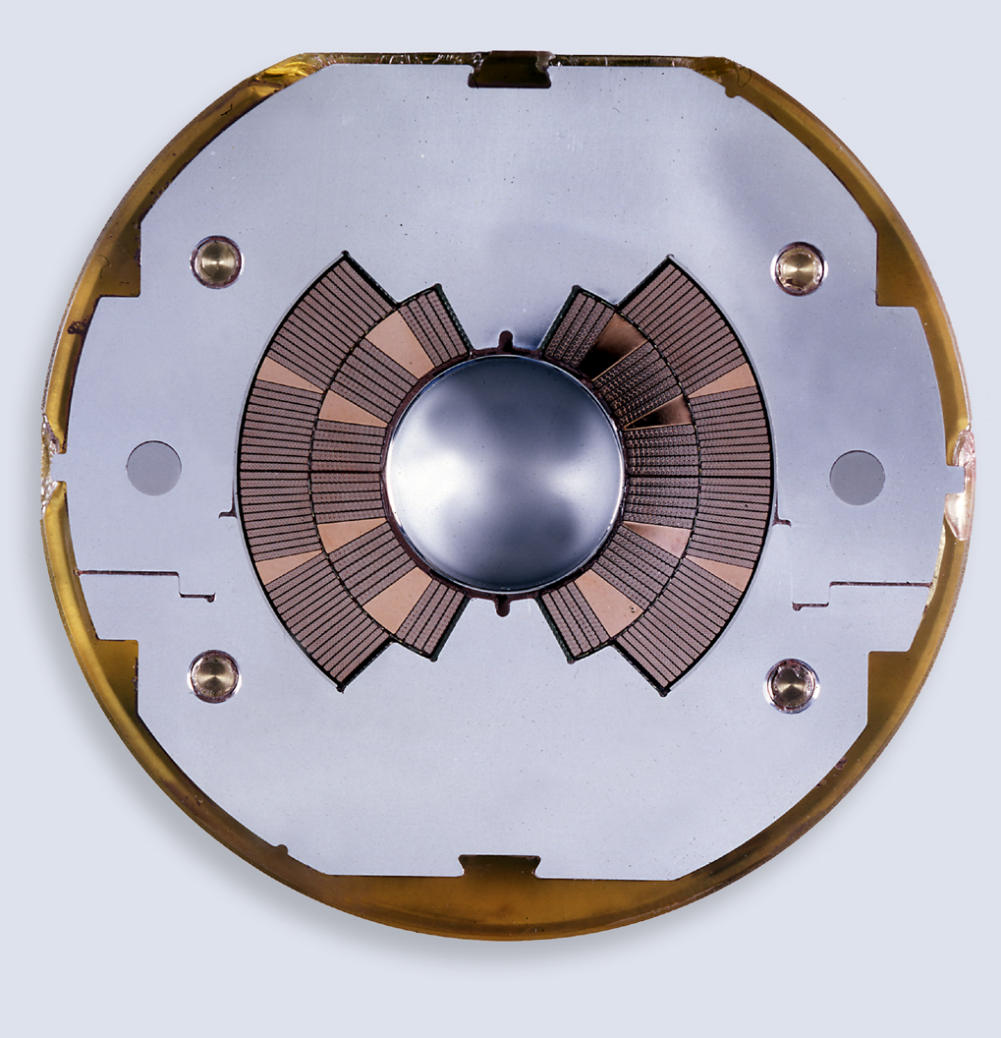

Figure 2.2.5 Particular LHC dipole coil cross section. Collars in stainless steel keep in the right position superconducting cable. In the centre there the vacuum pipe where beam flows.

Calculation of eddy currents is superconducting cables is the subject of this thesis.

From 1970s to today eddy currents, also called coupling currents, have been studied with several models and performing measure to validate them. Few efforts have been made to integrate this model in a magnet design tool in order to take this effect into account during design and testing process. In this thesis is shown how to efficiently integrate a model for eddy currents into the CERN magnet design program ROXIE [Rus99].

ROXIE is a integrated tool for simulating and optimise magnets design taking into account the effects of iron yoke, persistent current magnetisation and coil ends. Integration of a eddy currents model for superconducting cables will make possible to study magnetic field during ramping either for a better understanding of transient effects, or for helping in design process for future magnets.

Even if LHC magnets are in the production line, research and development is still in progress. After approximately ten years of operation several magnets close to the interaction region will be damaged by radiation, their replacement could be a opportunity for a luminosity upgrade. Several new synchrotron using fast pulsed superconducting magnets are going to be built in the next decades, a tool for calculating a ramp rate dependent error could be a great aid during design process.

2.3 Synchrotron Basics

A is a particle accelerator that use electric field of resonant cavities to accelerate particle. Magnets are used to bend particles in order to make a circular trajectory so that can pass several time through cavities to be accelerated. It is a very simple application of Lorentz force:

$$\boldsymbol{F} = qe(\boldsymbol{E} + \boldsymbol{v} \times \boldsymbol{B}), \tag{2.3.1}$$

where e is the charge of electron, q is the charge of the particle in unit of electron charge, $\boldsymbol{E}$ the electric field, $\boldsymbol{v}$ the velocity and $\boldsymbol{B}$ the magnetic field.

From (2.3.1) we see that we can use only electric field to accelerate a particle in order to increase its energy. Moreover we can see that efficiently bend high velocity particle with magnetic field, because force is proportional to the velocity.

Magnets are also used to control trajectory of particles and stabilise it using magnetic field as lens.

If the magnetic field is homogeneous particles follow a circular path. Momentum, radius and magnetic field are related by the formula:

$$Br[\,\mathrm{T\,m}] = 0.3356pq[\,\mathrm{GeV}/c] \tag{2.3.2}$$

where r is the radius of the circle and p the momentum and q is the number of electron charge of the particles.

From this relation we can argue that if we want particle accelerated to have more energy we have to increase magnetic field and radius. Maximum radius depends on cost we can afford, but magnetic field strange depends on technology. High magnetic field can be produced only with superconducting coil where high currents can flow without ohmic losses and produce magnetic field beyond iron saturation.

Moreover, relation (2.3.2) means that if we can keep the radius constant, while the particle get energy and increase the momentum, we have to increase the magnet field. Thus magnets have to follow a ramp in order to bend particle from injection energy to extraction or collision. In the figure 2.3.6 the excitation current for a dipole is shown.

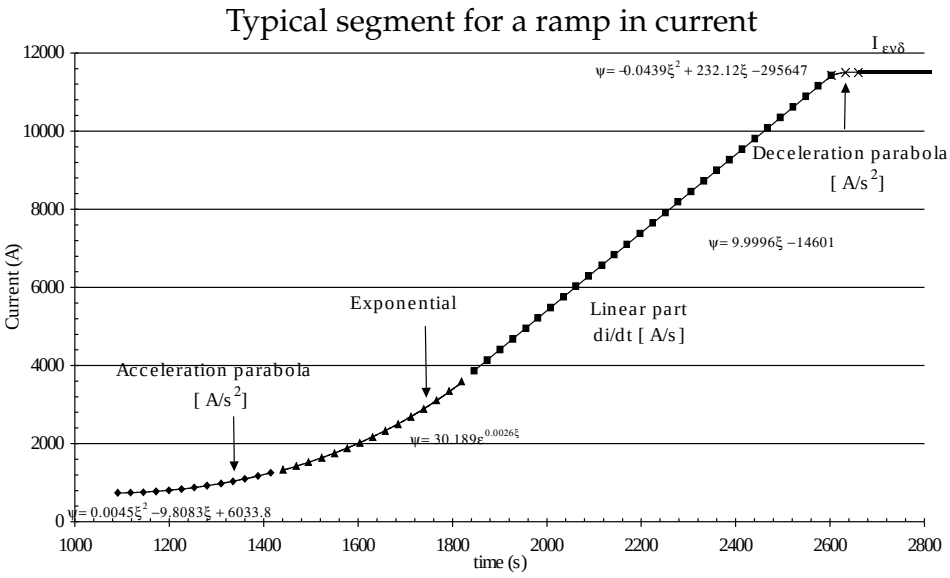

Figure 2.3.6 Proposed excitation function from injection to final energy for a LHC dipole.

The fact that magnets are used during ramp implies that the transients effects should be taken into account in magnet design.

2.4 Eddy currents

Main transient effects are due to the fact that magnetic field it is not constant in time. When magnetic field is not constant, an electric field is created due to the induction law. If there are material with low resistivity the electric field produces eddy currents that are responsible for ohmic losses and field errors. In accelerator magnets there are several parts with low resistivity where eddy currents are produced such as beam screen, copper wedge and superconducting cables. In the latter the resistivity is very low due to the fact that are made by a Nb-Ti alloy in superconducting state and copper and this leads to the highest currents.

2.5 Field errors

Deviations in the nominal field of the dipole bending magnets distort the central closed orbit (the path on which an ideal particle not performing oscillations will travel through the machine) and thus reduce the available machine aperture. Nonlinear field imperfections can cause resonances and limit the dynamic aperture (the maximum initial amplitude of oscillations around the closed orbit below which the particle motion is stable) particularly at injection, where the errors are large due to the remanent fields, and where the beam has a large emittance.

The magnetic field errors in the aperture of accelerator magnets can be expressed as the coefficients of the Fourier-series expansion of the radial field component at a given reference radius (in the 2-dimensional case). In the 3-dimensional case, the transverse field components are integrated over the entire length of the magnet. For beam tracking it is sufficient to consider the transverse field components, since the effect of the longitudinal component of the field (present only in the magnet ends) on the particle motion can be neglected. Assuming that the radial component of the magnetic flux density B_r at a given reference radius $r = r_0$ inside the aperture of a magnet is measured or calculated as a function of the angular position φ, we get for the Fourier-series expansion of the radial field component

$$B_r(r_0, \varphi) = \sum_{n=1}^{\infty} (B_n(r_0) \sin n\varphi + A_n(r_0) \cos n\varphi), \tag{2.5.1}$$

with

$$A_n(r_0) = \frac{1}{\pi}\int_{-\pi}^{\pi} B_r(r_0,\varphi)\cos n\varphi d\varphi,$$
$$B_n(r_0) = \frac{1}{\pi}\int_{-\pi}^{\pi} B_r(r_0,\varphi)\sin n\varphi d\varphi. \tag{2.5.2}$$

If the field components are related to the main field component B_N we get with N=1 for the dipole, N=2 for the quadrupole, etc.

$$B_r(r_0,\varphi) = B_N(r_0)\sum_{n=1}^{\infty}\left(b_n(r_0)\sin n\varphi + a_n(r_0)\cos n\varphi\right) \tag{2.5.3}$$

The B_n are called the normal and the A_n the skew components of the field given in Tesla, b_n the normal relative, and a_n the skew relative field components. The latter are dimensionless and are usually given in units of 10^{-4} at a 17 mm reference radius (about 2/3 of the aperture). For a good field quality these multipole components have to be less than one unit in 10^{-4}.

As an example we show a pure dipole field where all but b_1 components are equal 0, a quadrupole field where only $b_2 \neq 0$ and a sextupole field where $b_3 \neq 0$.

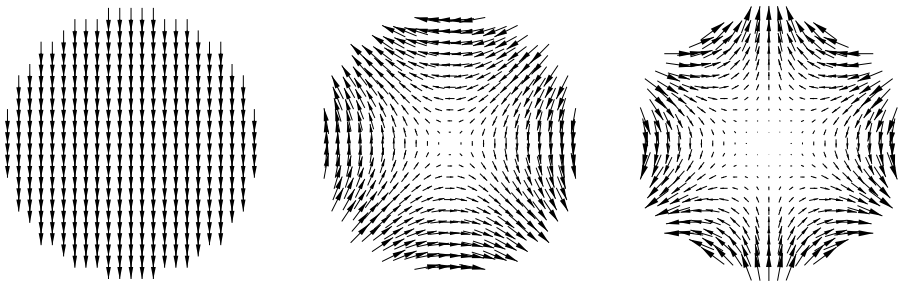

Figure 2.5.7 First three normal field component: left B_1, centre B_2, right B_3.

2.6 Quench

A quench is the transition from the superconducting to the normal state for an entire magnets. When a local increase of temperature, current or magnetic field such that superconductivity is broken, the current begins to

dissipate heat that propagates in the neighbours region provoking a new transitions. This produces is fast (milliseconds) and can be destructive if it is not detected.

Chapter 3

Superconductivity

3.1 Classic Theory

Superconductivity it is a property of some metals or alloys whose resistivity is unmeasurable low below a certain critical temperature. Transition between normal conducting and superconducting state is stepwise. Critical temperature depends from the material and the presence of currents or magnetic field that are able to increase the internal energy of the material. For this reason there is a limit in the current and magnetic field generated by superconducting coils. It can be defined a critical surface in the space of three state variable, current, magnetic field and temperature (see figure 3.1.1).

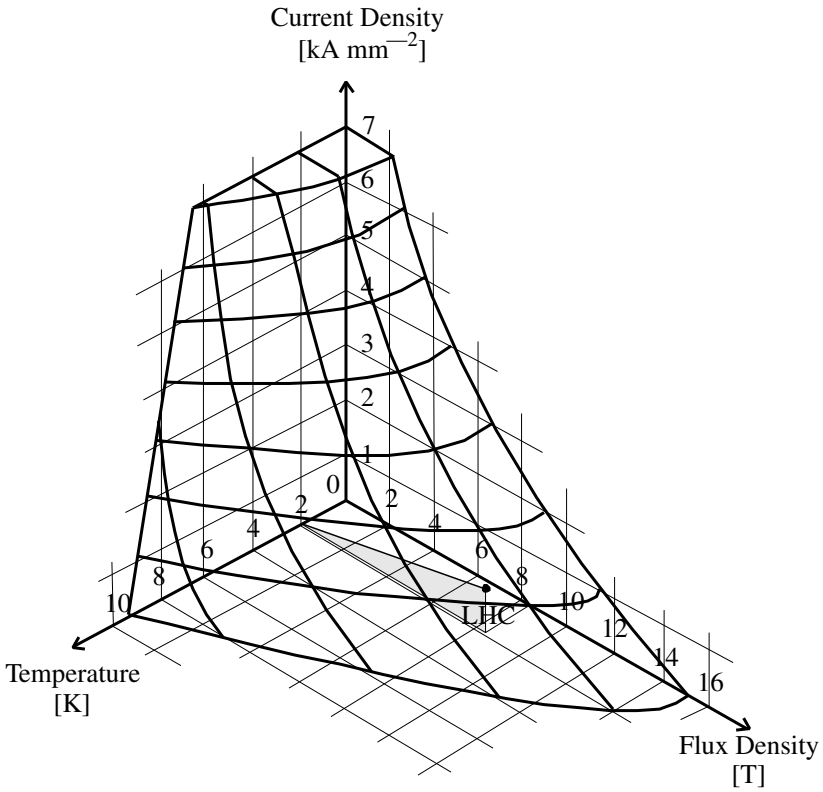

Figure 3.1.1 Critical current surface of the NbTi alloy as a function of temperature and field with the load-line of the LHC dipoles. Note that for the multi-strand cable the critical current density is about 15% lower than for pure NbTi.

3.2 Superconducting Materials

There are two type of superconducting material: type I and type II. The former cannot have magnetic field inside in the superconducting state, they produce current in the surface in order to shield external magnetic field. The latter can have magnetic field inside. Usually type II superconducting materials have a higher critical magnetic field, thus they are well suited for superconducting magnets.

Magnetic field is not distributed continuously inside a type II superconductor, but it is located flux tubes called fluxoids. Inside a fluxoid superconductor is in normal conducting state, fluxoid are surrounded by currents that shield the part in superconducting state. When a current flow in the superconductor the fluxoids, due the Lorentz force, tends to move generating heat. For this reason it has been developed material with pinning centre, impurity or defects, that take fluxoids fixed in a position. For example in the NbTi alloy, the normal conducting titanium precipitated in small region facilitate the creation of pinning centres. The materials with strong pinning centre are called hard superconductor and are the material to be used in superconducting magnets.

In superconducting magnets field distribution is dominated by coil shape, and not by iron yoke as in the normal conducting magnet. For this reason it is important to choose a material with good mechanics properties. This needs limit superconducting material to NbTi and Nb_3Sn alloys. The former have better mechanical properties but a lower critical field, the contrary for the latter. Nowadays the most used alloy is NbTi, but a great effort in R&D is made Nb_3Sn alloys in order to use it in superconducting magnets.

3.3 Rutherford-type Cable

Cables used for superconducting magnets have a complex structure. They are composed of strands twisted together in order to assume a flat form. In figure 3.3.2 we can see a 36 strands Rutherford-type cable. Strands are compressed together in order to make the cut assume a trapezoidal form (see figure 3.3.4). Each strand is composed of filaments included in a copper matrix. Photo 3.3.3 gives an idea.

In the figure 3.3.4 we can see a cut of four cables. We can recognise the strands, some of which are deformed in order to obtain the desired shape of the cables. In the figure 3.3.5 is shown an enlarged cut of a strand in which are clearly visible the superconducting filament.

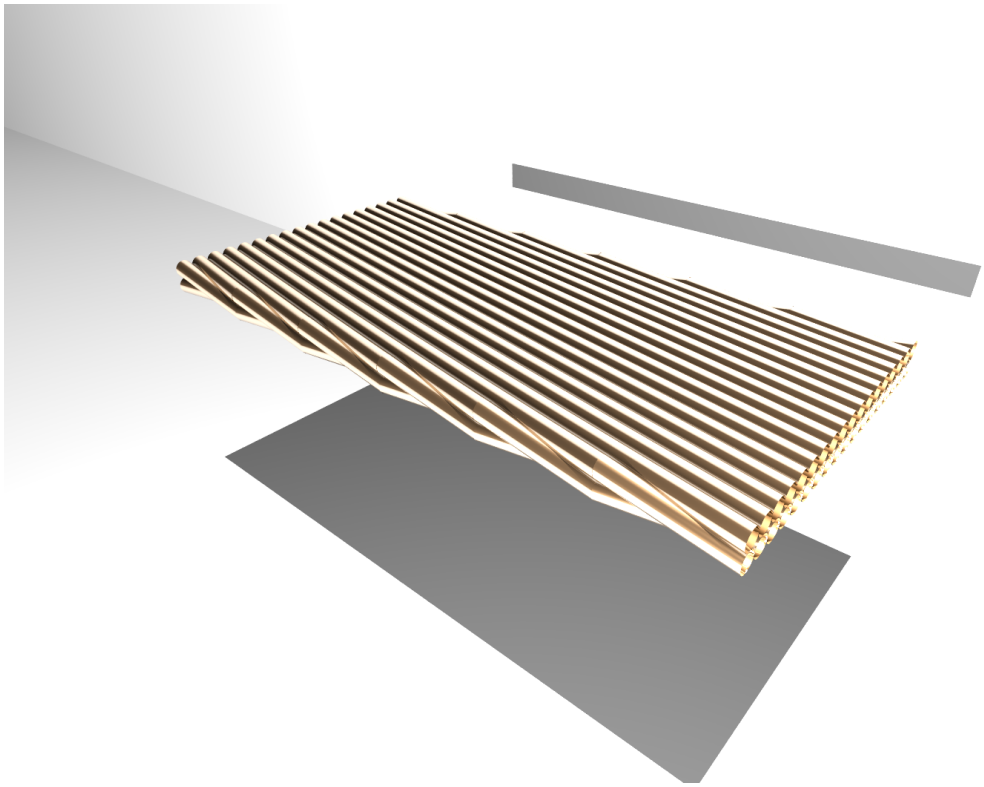

Figure 3.3.2 Strands of a Rutherford type cable.

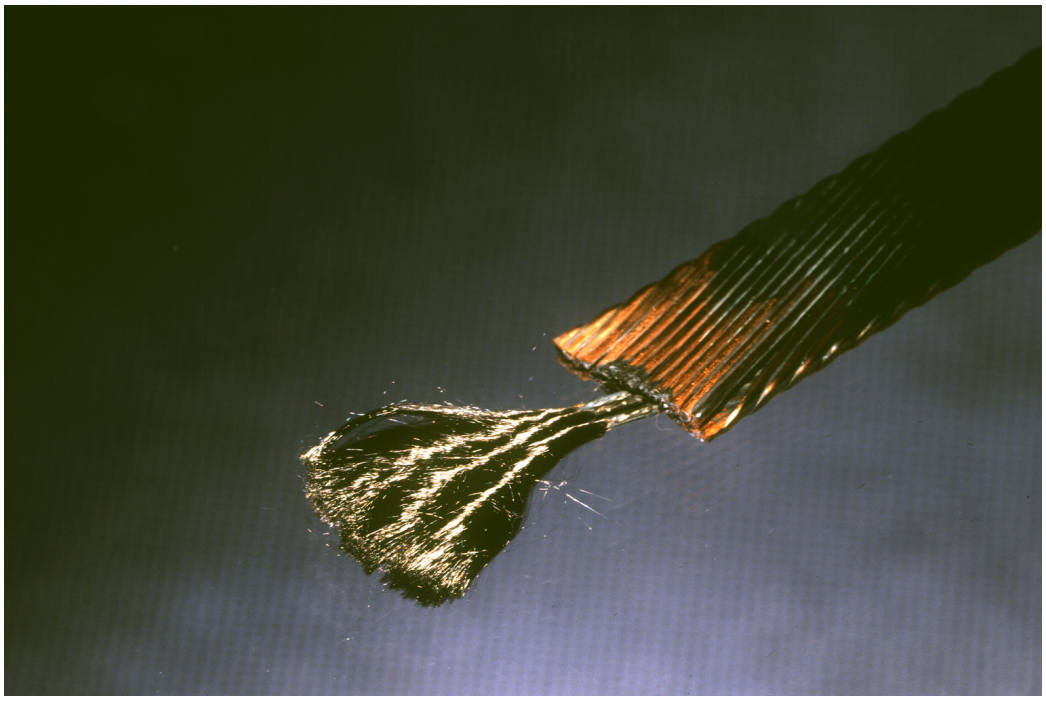

Figure 3.3.3 Strands and filaments of a Rutherford type cable.

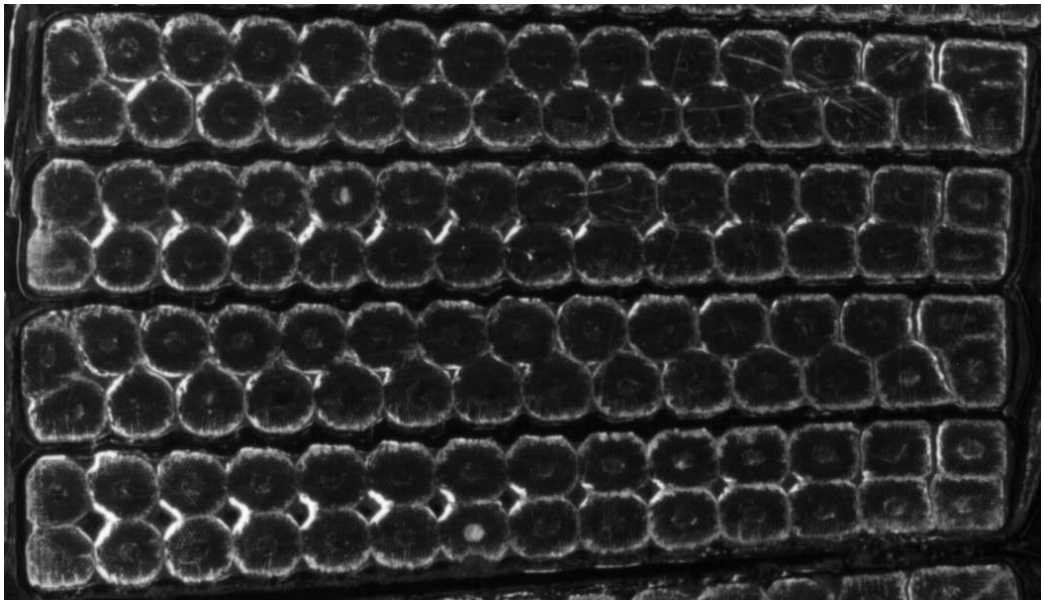

Figure 3.3.4 Cut through a block of conductors showing the cables composed of superconducting strands

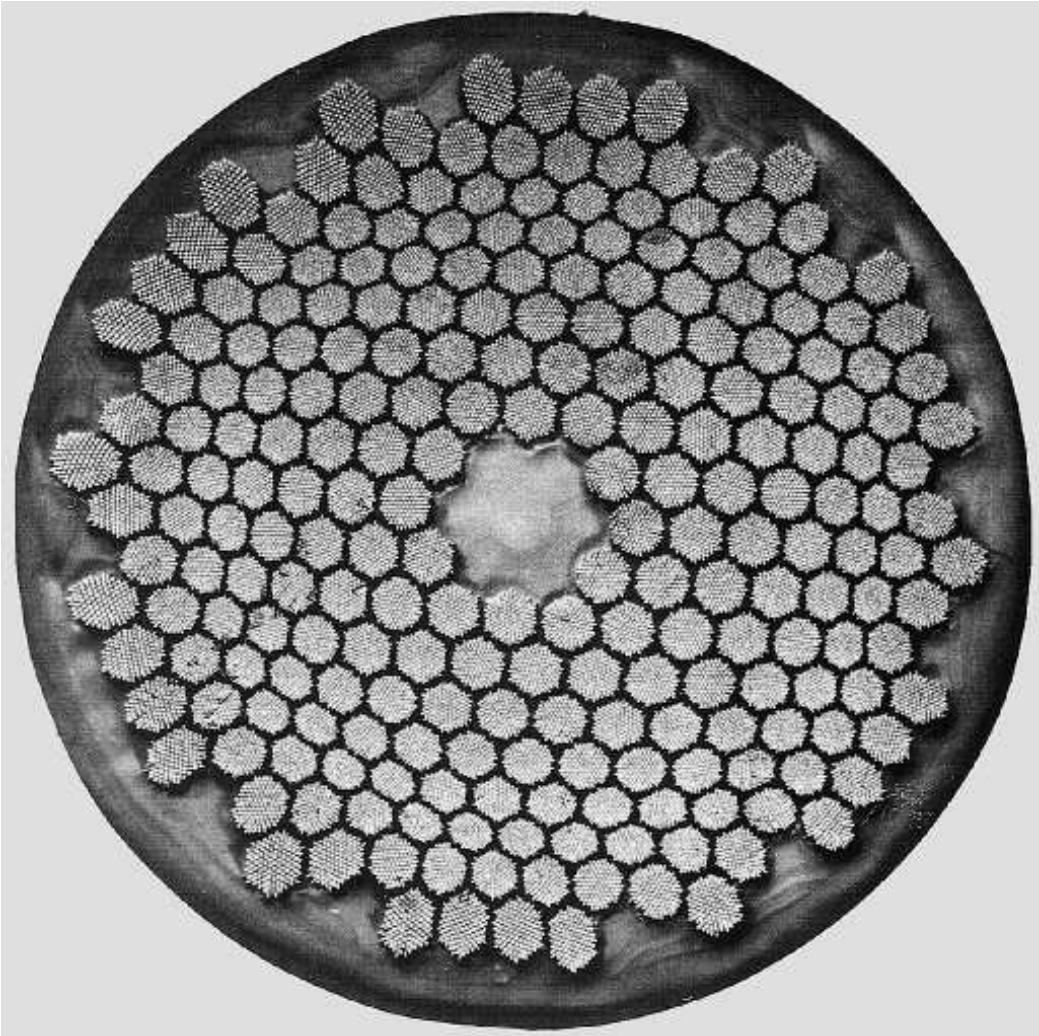

Figure 3.3.5 Multi-filament strand.

3.4 Physical properties

The cable is characterised by several typical properties. The table shows typical values for accelerator magnets [VtKL+95]:

Twist Pitch Lenght	L_p	$100 - 130\,\mathrm{mm}$
Width	w	$7 - 17\,\mathrm{mm}$
Thickness	h	$1 - 2.5\,\mathrm{mm}$
Strand Diameter	D_s	$0.8 - 1.1\,\mathrm{mm}$
Filament Diameter	D_f	$5 - 7\,\mu\mathrm{m}$
Number of Strands	N_s	$20 - 40$
Number of Filament	N_s	$5000 - 9000$
Cable Critical current, $1.9\,\mathrm{K}$, $10\,\mathrm{T}$	I_{max}	$12 - 13\,\mathrm{kA}$
Strand Critical current, $1.9\,\mathrm{K}$, $10\,\mathrm{T}$	I_{maxs}	$0.3 - 0.5\,\mathrm{kA}$

(3.4.1)

The number of strands in a cable ranges from 20 to 40 depending on the type of magnets and in the same magnet on the layer.

Thickness of the cable can be different due to key stoning (see figure 3.3.4). In fact cables are compressed and deformed in order to make them assume the right shape. The compression increases the contact surface between strands leading to a decrease of electrical resistance between strands, the main responsible of eddy current generation.

Contact resistances are divided in two family, cross resistances and adjacent resistances. Cross resistances, R_c, are the resistances from strands that belongs to different layer, adjacent resistances are the resistances that occurs between two close strand in the same layer.

Contact resistances mainly depend on the surface of the strands usually copper oxide. Surface is subject several treatment and temperature cycles during fabrication. Matrix resistivity doesn't play a role only if it is made by pure copper. In some cables a resistive barrier is put between the two layers of the cable, thus only cross resistances are enhanced.

In addiction to this effects that depend on the fabrication process, there are other process that change the resistance inside a magnets. The key stoning changes the contact surfaces and the pressure between strands. This pressure is not uniform in the magnets, in particular different in the coil ends. The pressure change during the operation of the magnets because cables are subjects to the Lorentz force.

All this factors are difficult to control. Moreover contact resistance are difficult to measure. Even if measured before magnet assembling , they will change during fabrication process and during operation of the magnets. Inside a magnets can be measured only by inverse field calculation and a correlation with losses.

Chapter 4

Experimental Observations

Eddy currents (also known as coupling currents) effects play a role in the heat losses, the ramp rate dependent field errors, quench current limit, cable magnetisation. When the magnetic field begins to increase eddy currents starts to build up in the conductors. Then they reach a limit depending on the variation of the magnetic field. When the the magnetic field increas stops, the eddy cirrents decay.

We can classify coupling currents if three categories [Ver95]:

IFCC Interfilament coupling currents;

ISCC Interstrand coupling currents, also called simply "coupling currents";

BICC Boundary induce coupling currents, also called "supercurrents" [KS95].

IFCC are the currents which flow between filament in the strands, they grow with a time scale of milliseconds. They are important during quench propagation process.

Between strands flow two kind of currents. ISCC are currents which depend only on a single periodic part of the twisted cable. They have time scales of seconds. They are responsible of the main losses and field errors. BICC depend on the whole lenght of the cable for the fact that the cable it not infinite (spatial variation of $\frac{\partial}{\partial t}\boldsymbol{B}$ [VtK95], [KS95]) and that the cable it is not perfect (not perfect cancelation of flux linkage). They have a time scale of order of hours or days. They are long loops of currents flowing mainly in the superconductor. They are responsible a periodic field pattern along longitudinal axis and affects quench current limit due to a local rise of current density. The interaction of this currents with filament magnetization is responsible of the so-called "decay and snapback" [HKdO$^+$01].

4.1 Interstrands Coupling Currents

The existence of eddy currents inside superconducting cables has been evident from the first stage of cable studies and realizations. A linear relation between ramp rate dependent losses can be measured easily on superconducting magnets ([ABB+00]), see figure 4.1.1.

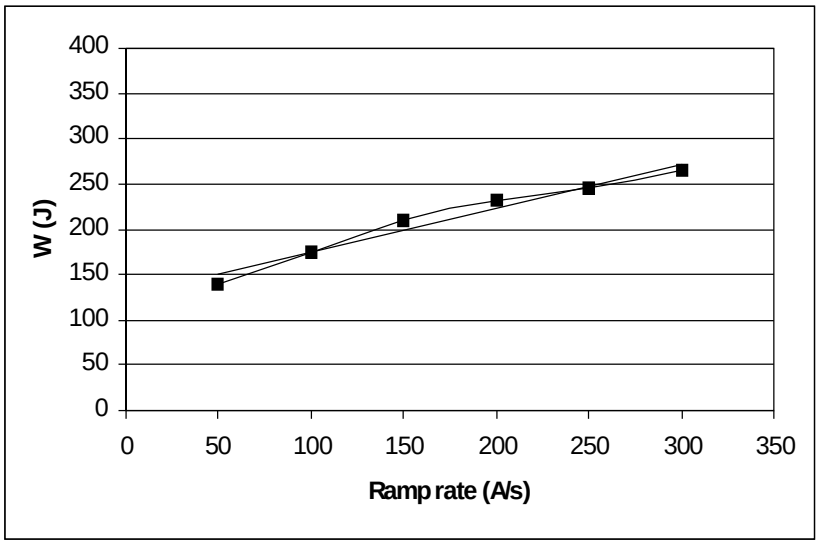

Figure 4.1.1 Work done by the current during a cycle from minimum to maximum current and back in a LHC dipole magnet.

Another linear correletaion with the ramp rate can be found with the histeresis width for field error normalized component.

In the figure 4.1.2 we can see the ramp rate depend histeresis of a field compoment. The histeresis is not centered in the 0 for the presence of a geometrical error. The amplitude of the width is linear with the ramparate as we can see in the figure:

4.2 Boundary Induced Coupling Currents

The existence of periodic field pattern in superconducting magnets was discovered at first at HERA [BGK+91]. In the figure 4.2.4 we can see a periodic field pattern of the sextupole component. Subsequently this pattern has been measured in the rest of superconducting magnets. The periodicity length is equal to the cable twist pitch inside the measure errors. This is an evidence that it is cable effects. The periodicity affects all the harmonic

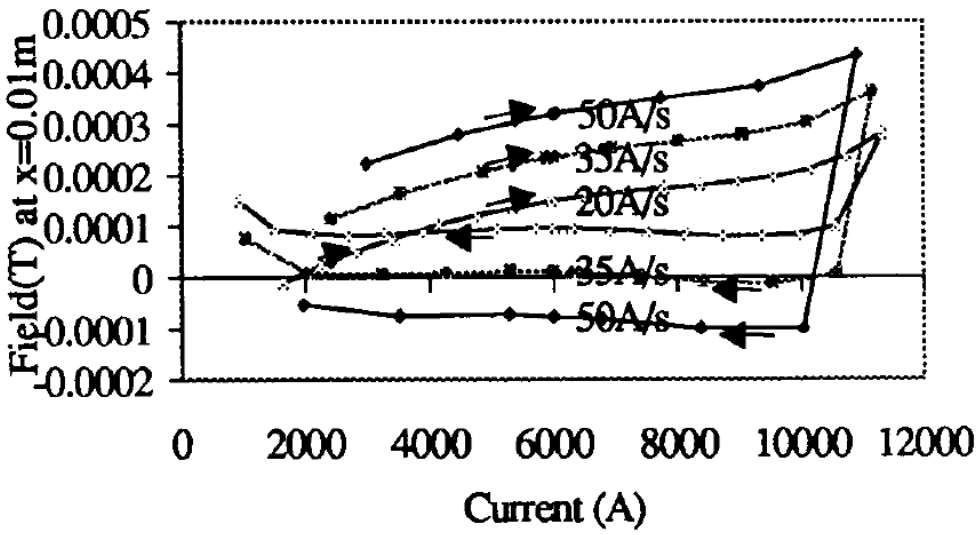

Figure 4.1.2 Sextupole histeresis at different ramp rate [BRW$^+$95].

component of magnetic field, even the not allowed component due to the symmetry. This fact is compatible to the randomness of interstrands contact resistances. At the early stage of excitation the magnets do not present the periodic pattern. After ramping magnetic field this pattern persist for hours and show a decay.

In the figures 4.2.4, 4.2.5, 4.2.6 we can see measures of periodic pattern of the sextupole component in LHC magnets in several situation [BWA97]. From that we can have an idea on the time scale involved. It is important to note that the pattern is different from magnet to magnets of the same type and in the same magnets with different excitation history.

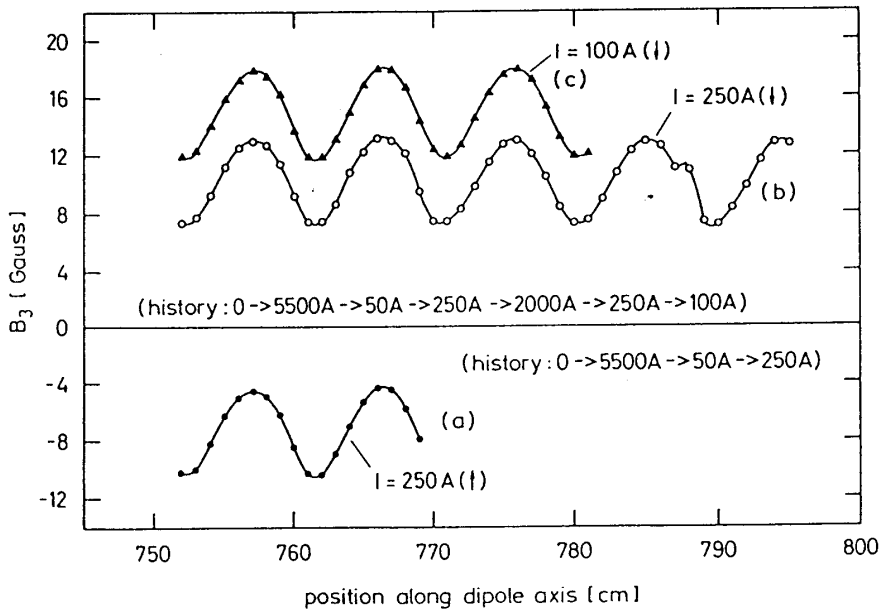

Figure 4.2.3 Periodic field pattern of the sextupole component in a HERA magnet.

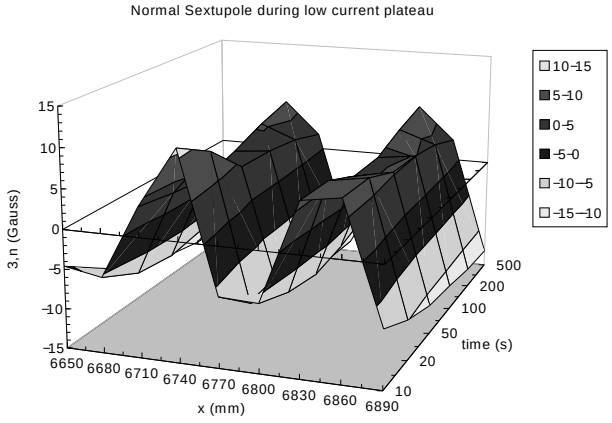

Figure 4.2.4 Periodic field pattern of the sextupole component in a LHC magnet. Time evolution during flat top at injection. Courtesy of Luca Bottura.

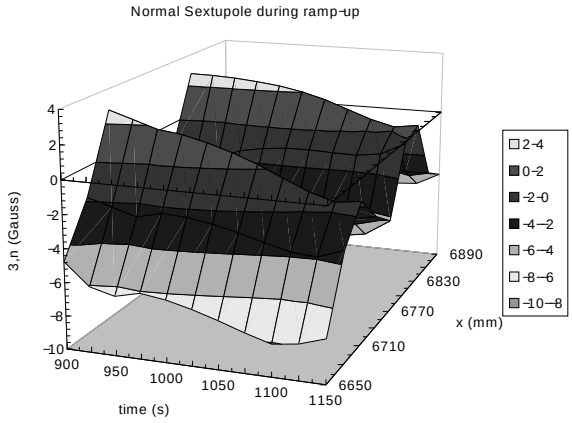

Figure 4.2.5 Periodic field pattern of sextupole component in a LHC magnet. Time evolution during ramp up. Courtesy of Luca Bottura.

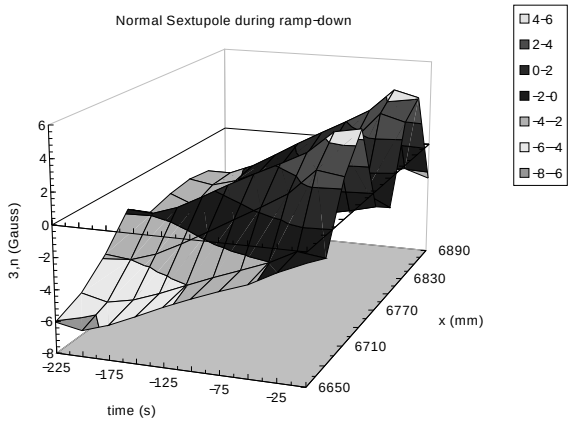

Figure 4.2.6 Periodic field pattern of sextupole component in a LHC magnet. Time evolution during ramp down. Courtesy of Luca Bottura.

Chapter 5

Electromagnetic Diffusion Problems

5.1 Maxwell Equations

Maxwell equations are:

$$\begin{aligned} \nabla \cdot \boldsymbol{D} &= \rho \\ \nabla \cdot \boldsymbol{B} &= 0 \\ \nabla \times \boldsymbol{E} &= -\frac{\partial}{\partial t}\boldsymbol{B} \\ \nabla \times \boldsymbol{H} &= \boldsymbol{J} + \frac{\partial}{\partial t}\boldsymbol{D} \end{aligned} \tag{5.1.1}$$

with

$$\begin{aligned} \boldsymbol{D} &= \varepsilon \boldsymbol{E} \\ \boldsymbol{J} &= \sigma \boldsymbol{E} \\ \boldsymbol{B} &= \mu \boldsymbol{H}. \end{aligned} \tag{5.1.2}$$

Using $\nabla \cdot \boldsymbol{B} = 0$, a vector potential $\boldsymbol{A}$ can be defined such that

$$\boldsymbol{B} = \nabla \times \boldsymbol{A}. \tag{5.1.3}$$

Using $\nabla \times (\boldsymbol{E} + \frac{\partial}{\partial t}\boldsymbol{A}) = 0$, Φ can be defined such that

$$\boldsymbol{E} = -\nabla \Phi - \frac{\partial}{\partial t}\boldsymbol{A}. \tag{5.1.4}$$

In the following we assume ε and μ to be scalar and constant. σ could be a tensor depending on the position and the current.

5.2 Magneto Quasi-static Approximation

Last equation of (5.1.1) multiplied by μ becomes

$$\nabla \times \boldsymbol{B} = \mu\sigma\boldsymbol{E} + \mu\varepsilon\frac{\partial}{\partial t}\boldsymbol{E}. \tag{5.2.1}$$

In order to compare the importance of the two terms of the right hand side of the last equation we can state:

$$\frac{\partial}{\partial t}\boldsymbol{E} = O\left(\frac{\boldsymbol{E}}{\tau}\right), \tag{5.2.2}$$

where τ is the typical time scale of our system.
Now the last equation can be written as

$$\nabla \times \boldsymbol{B} = \mu\left(O\left(\sigma\boldsymbol{E}\right) + O\left(\frac{\varepsilon}{\tau}\boldsymbol{E}\right)\right). \tag{5.2.3}$$

If

$$\sigma \gg \frac{\varepsilon}{\tau}, \tag{5.2.4}$$

we can neglect the last term of (5.2.1),

$$\varepsilon\frac{\partial}{\partial t}\boldsymbol{E} = O\left(\frac{\varepsilon}{\tau}\boldsymbol{E}\right) \approx 0. \tag{5.2.5}$$

This is called magneto quasi-static approximation.
In this case Maxwell equations (5.1.1) can be written as:

$$\begin{aligned} \nabla \times \boldsymbol{E} &= -\frac{\partial}{\partial t}\boldsymbol{B} \\ \nabla \times \boldsymbol{B} &= \mu\sigma\boldsymbol{E}. \end{aligned} \tag{5.2.6}$$

One consequence is:

$$\nabla \cdot \boldsymbol{J} = \nabla \cdot \sigma\boldsymbol{E} = 0. \tag{5.2.7}$$

Knowing that $\rho = \varepsilon\nabla \cdot \boldsymbol{E}$, $\rho = 0$ holds only if

$$\nabla \cdot \sigma\boldsymbol{E} = \sigma\nabla \cdot \boldsymbol{E}, \tag{5.2.8}$$

that happens if σ is scalar and independent of the position.

In conclusion the magneto quasi-static approximation means that we can neglect the effects of the charge building process, assuming that if this charge exists it builds up instantaneously. The existence of this charge and his effects is studied in [Car04].

5.3 External Sources

In our problems we need to introduce an external source of magnetic field $\boldsymbol{B}_e$ or vector potential $\boldsymbol{A}_e$ neglecting the effects that the system has on those sources. In fact we don't want to simulate the entire magnet because the effects of the eddy currents are small compared those of the transport currents. We only use the magnetic field generated by them. We can formalise this assumption writing Maxwell's equations for the sum of two current density and magnetic fields. $\boldsymbol{J}$ and $\boldsymbol{B}$ are the current densities and magnetic field due to the eddy currents and $\boldsymbol{J}_e$, $\boldsymbol{B}_e$ due to the transport currents. In this way we can write

$$\nabla \times \boldsymbol{E} = -\frac{\partial}{\partial t}\boldsymbol{B} - \frac{\partial}{\partial t}\boldsymbol{B}_e \tag{5.3.1}$$

and

$$\nabla \times \boldsymbol{B} + \nabla \times \boldsymbol{B}_e = \mu \boldsymbol{J} + \mu \boldsymbol{J}_e. \tag{5.3.2}$$

The assumption of none feed back can be taken into account writing:

$$\nabla \times \boldsymbol{B}_e = \mu \boldsymbol{J}_e \tag{5.3.3}$$

which yields

$$\nabla \times \boldsymbol{B} = \mu \boldsymbol{J} \tag{5.3.4}$$

Using vector potentials for both $\boldsymbol{B}$ and $\boldsymbol{B}_e$ we can write

$$\boldsymbol{E} = -\nabla \Phi - \frac{\partial}{\partial t}(\boldsymbol{A} + \boldsymbol{A}_e), \tag{5.3.5}$$

where $\boldsymbol{B}_e = \nabla \times \boldsymbol{A}_e$.

5.4 Diffusion equations

Quasi static assumpion leads to diffusion equation. In fact we can write several equations derived from Maxwell's equation:

$$\begin{aligned} \sigma^{-1}(\nabla \times \boldsymbol{B}) = \mu \boldsymbol{E} \Rightarrow \\ \nabla \times \left(\sigma^{-1}(\nabla \times \boldsymbol{B})\right) = -\mu \frac{\partial}{\partial t}(\boldsymbol{B} + \boldsymbol{B}_e) \end{aligned} \tag{5.4.1}$$

or

$$\begin{aligned} \nabla \times \frac{\partial}{\partial t}\boldsymbol{B} = \nabla \times (\nabla \times \boldsymbol{E} - \frac{\partial}{\partial t}\boldsymbol{B}_e) = -\mu\sigma \frac{\partial}{\partial t}\boldsymbol{E} \Rightarrow \\ \nabla \times \nabla \times \boldsymbol{E} = -\mu\sigma \frac{\partial}{\partial t}\boldsymbol{E} + \nabla \times \frac{\partial}{\partial t}\boldsymbol{B}_e \end{aligned} \tag{5.4.2}$$

or

$$\nabla \times \nabla \times \sigma^{-1}\boldsymbol{J} = -\mu\frac{\partial}{\partial t}\boldsymbol{J} + \nabla \times \frac{\partial}{\partial t}\boldsymbol{B}_e. \tag{5.4.3}$$

If conducibility is homogeneous and isotropic preavios equations become diffusion equations because left hand sides of preavios equation become curl-curl operator applied to diverge free fields, that is a laplacian operator. In fact

$$\begin{aligned} \nabla \times \left(\sigma^{-1}(\nabla \times \boldsymbol{B})\right) &= \sigma^{-1}\nabla \times \nabla \times \boldsymbol{B}, \\ \nabla \times \nabla \times \sigma^{-1}\boldsymbol{J} &= \sigma^{-1}\nabla \times \nabla \times \boldsymbol{J}, \\ \nabla \cdot \boldsymbol{E} &= \sigma^{-1}\nabla \cdot \boldsymbol{J} = 0, \end{aligned} \tag{5.4.4}$$

thus

$$\begin{aligned} \nabla^2\boldsymbol{B} &= \sigma\mu\frac{\partial}{\partial t}(\boldsymbol{B} + \boldsymbol{B}_e) \\ \nabla^2\boldsymbol{E} &= \sigma\mu\frac{\partial}{\partial t}\boldsymbol{E} + \nabla \times \frac{\partial}{\partial t}\boldsymbol{B}_e, \\ \nabla^2\boldsymbol{J} &= \sigma\mu\frac{\partial}{\partial t}\boldsymbol{J} - \sigma\nabla \times \frac{\partial}{\partial t}\boldsymbol{B}_e. \end{aligned} \tag{5.4.5}$$

5.5 Maxwell's Equation Solution

A direct use of Maxwell's equations is difficult due the fact that the internal structure of the cable is small compared to the total dimensions. A continuous approach can be used if we neglect the structure of the cable and we use a global non isotropic conductivity. Only the equations are derived.

The main problem to solve equations (5.4.1), (5.4.2) and (5.4.1) is that the curl-curl operator cannot be simplified using divergence free field or there is a tensor that multiply the vector field. In both cases the components of the vector fields are coupled. In the 2D equation can be decoupled if conductivity is diagonal and independent on position.

Assuming $\boldsymbol{B} = B(x, y, t)\boldsymbol{e}_z$, $\boldsymbol{B}_e = B_e(x, y, t)\boldsymbol{e}_z$ and $\sigma = \sigma_x\boldsymbol{e}_x\boldsymbol{e}_x + \sigma_y\boldsymbol{e}_y\boldsymbol{e}_y$

the equation for $\boldsymbol{B}$ (5.4.1) can be simplified:

$$\begin{aligned}
\nabla \times B(x,y,t)\boldsymbol{e}_z &= \frac{\partial}{\partial y}B(x,y,t)\boldsymbol{e}_x - \frac{\partial}{\partial x}B(x,y,t)\boldsymbol{e}_y \\
\sigma^{-1}\left(\frac{\partial}{\partial y}B(x,y,t)\boldsymbol{e}_x - \frac{\partial}{\partial x}B(x,y,t)\boldsymbol{e}_y\right) &= \frac{\partial}{\partial y}\frac{B(x,y,t)}{\sigma_x}\boldsymbol{e}_x - \frac{\partial}{\partial x}\frac{B(x,y,t)}{\sigma_y}\boldsymbol{e}_y \\
\nabla \times \left(\frac{\partial}{\partial y}\frac{B(x,y,t)}{\sigma_x}\boldsymbol{e}_x - \frac{\partial}{\partial x}\frac{B(x,y,t)}{\sigma_y}\boldsymbol{e}_y\right) &= \frac{\partial^2}{\partial x^2}\frac{B(x,y,t)}{\sigma_y}\boldsymbol{e}_z + \frac{\partial^2}{\partial y^2}\frac{B(x,y,t)}{\sigma_x}\boldsymbol{e}_z \\
\frac{\partial^2}{\partial x^2}\frac{B(x,y,t)}{\sigma_y} + \frac{\partial^2}{\partial y^2}\frac{B(x,y,t)}{\sigma_x} &= -\mu\frac{\partial}{\partial t}B(x,y,t) - \mu\frac{\partial}{\partial t}B_e(x,y,t).
\end{aligned} \tag{5.5.1}$$

This is the equation for a piece of flat conductor with a conductivity that depends on the direction, for example a non twisted Rutherford-type cable. In order to "simulate" a twisting the source B_e could be assumed sinusoidal in the direction of twisting.

5.6 Potential Formulation

Assuming the Coulomb Gauge, $\nabla \cdot A = 0$, the Maxwell's equations (5.1.1) became:

$$\nabla^2 \boldsymbol{A}(\boldsymbol{r},t) = -\mu \boldsymbol{J}(\boldsymbol{r},t) \tag{5.6.1}$$

$$\nabla \cdot \boldsymbol{J}(\boldsymbol{r},t) = 0 \tag{5.6.2}$$

$$\sigma^{-1}(\boldsymbol{r},\boldsymbol{J})\boldsymbol{J}(\boldsymbol{r},t) = -\nabla\Phi(\boldsymbol{r},t) - \frac{\partial}{\partial t}\boldsymbol{A}(\boldsymbol{r},t), \tag{5.6.3}$$

where $\sigma^{-1}(\boldsymbol{r},\boldsymbol{J})$ is the resistivity. In particular for mixed normal conductor, super-conductor is a tensor depending on the position and on the current density, in the following to ease notation, we will write simply σ^{-1}, but during calculation, these dependences are taken into account.

If we want to consider an external source of vector potential $\boldsymbol{A}_e$ neglecting the effects on it (using (5.3.1)), the previous system becomes

$$\nabla^2 \boldsymbol{A}(\boldsymbol{r},t) = -\mu \boldsymbol{J}(\boldsymbol{r},t) \tag{5.6.4}$$

$$\nabla \cdot \boldsymbol{J}(\boldsymbol{r},t) = 0 \tag{5.6.5}$$

$$\sigma^{-1}\boldsymbol{J}(\boldsymbol{r},t) = -\nabla\Phi(\boldsymbol{r},t) - \frac{\partial}{\partial t}(\boldsymbol{A}(\boldsymbol{r},t) + \boldsymbol{A}_e(\boldsymbol{r},t)). \tag{5.6.6}$$

An approach that leads us to a numerical solution is to solve (5.6.4) using the Green function of the Laplace operator for free space $G(\boldsymbol{r}) = \frac{1}{4\pi r}$

where $r = |\boldsymbol{r}|$. This yields:

$$\boldsymbol{A}(\boldsymbol{r},t) = G(\boldsymbol{r}) \circledast (\mu \boldsymbol{J}(\boldsymbol{r})) = \frac{\mu}{4\pi} \int_{V'} \frac{\boldsymbol{J}(\boldsymbol{r}',t)}{|\boldsymbol{r}'-\boldsymbol{r}|} dV'. \tag{5.6.7}$$

Equation (5.6.6) becomes

$$\sigma^{-1}\boldsymbol{J}(\boldsymbol{r},t) + \frac{\mu}{4\pi} \int_{V'} \frac{\frac{\partial}{\partial t}\boldsymbol{J}(\boldsymbol{r}',t)}{|\boldsymbol{r}'-\boldsymbol{r}'|} dV' = -\nabla\Phi(\boldsymbol{r},t) - \frac{\partial}{\partial t}\boldsymbol{A}_e(\boldsymbol{r},t). \tag{5.6.8}$$

5.7 Numerical Approach

A numerical solution of the system can be found using the PEEC (partial element equivalent circuit) analysis [Rue74]. The magneto quasi static aproximation yields the existence of resistance, inductance circuit elements and voltage source elements.

Following [BRR79] and [Kam98], equation (5.6.8) can be solved assuming $\boldsymbol{J}$ constant in space in some region and zero outside.This can be done using the expansion:

$$\boldsymbol{J}(\boldsymbol{r},t) = \sum_i \boldsymbol{J}_i(t) w_i(\boldsymbol{r}) = \sum_i J_i(t) \boldsymbol{w}_i(\boldsymbol{r}) \tag{5.7.1}$$

where $\boldsymbol{J}_i(t)$ is the current density assumed constant in the volume V_i, $w_i(\boldsymbol{r})$ is weighting function that is 1 in the volume V_i and 0 outside. Thus $\boldsymbol{w}_i(\boldsymbol{r})$ is a vector field that is $\boldsymbol{J}_i(t)/J_i(t)$ in the volume V_i and 0 outside, where $J_i(t) = |\boldsymbol{J}_i(t)|$. Volume V_i has to be a flux tube of $\boldsymbol{J}$ in order to simplify next calculations. Volumes can overlap, the important is that

$$\int_V \boldsymbol{w}_i(\boldsymbol{r}) \cdot \boldsymbol{w}_j(\boldsymbol{r}) = \delta_{ij}, \tag{5.7.2}$$

where δ_{ij} is the Kronecker delta.

In the figure 5.7.1 the elementary volume V_i is sketched

Under this assumption can be defined a current in the volume

$$I_i(t) = \int_{S_i} J_i(t) \boldsymbol{w}_i \cdot \boldsymbol{dS}_i = S_i J_i(t), \tag{5.7.3}$$

where S_i is a surface orthogonal to $\boldsymbol{w}_i$.

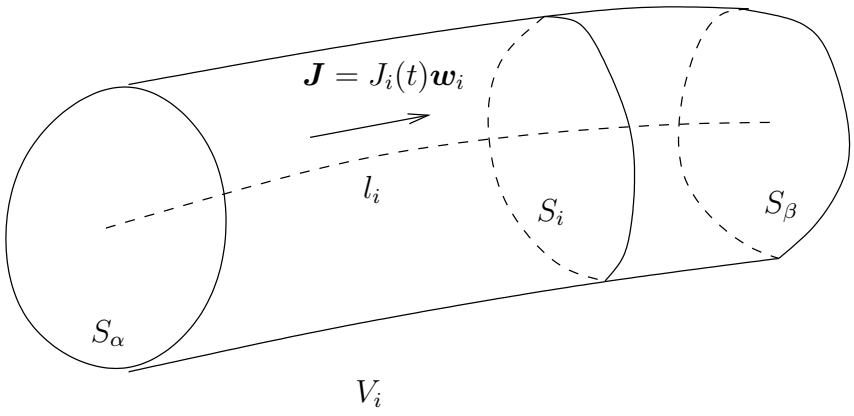

Figure 5.7.1 Elementary volume V_i in which space is subdivided.

Now we can integrate in the volume each term of (5.6.8) weighted with each $\boldsymbol{w}_i(\boldsymbol{r})$ function. This yields for the first term:

$$\begin{aligned}\int_V \boldsymbol{w}_i(\boldsymbol{r}) \cdot (\sigma^{-1}\boldsymbol{J}(\boldsymbol{r},t))dV = \int_{V_i} \sum_i \sigma^{-1} J_j(t)\boldsymbol{w}_j(\boldsymbol{r}) \cdot \boldsymbol{w}_i(\boldsymbol{r})dV_i = \\ = \int_{V_i} \sigma^{-1} J_i(t)dV = I_i(t) \int_{l_i} \frac{\sigma^{-1}}{S_i} dl_i = R_i I_i(t),\end{aligned} \tag{5.7.4}$$

where l_i is a field line of $\boldsymbol{J}$ and R_i is the resistance of the volume V_i in the direction of $\boldsymbol{w}_i$.

The second term of (5.6.8) yields

$$\begin{aligned}\frac{\mu}{4\pi} \int_V \boldsymbol{w}_i(\boldsymbol{r}) \cdot \int_{V'} \frac{\frac{\partial}{\partial t}\boldsymbol{J}(\boldsymbol{r}',t)}{|\boldsymbol{r}'-\boldsymbol{r}|} dV'dV = \\ = \frac{\mu}{4\pi} \sum_j \int_{V_i} \int_{V_j} \frac{\boldsymbol{w}_i(\boldsymbol{r}) \cdot \boldsymbol{w}_j(\boldsymbol{r}) \frac{\partial}{\partial t} J_j(t)}{r_{ij}} dV_i dV_j = \\ = \sum_j \frac{\partial}{\partial t} I_j(t) \frac{\mu}{4\pi} \frac{1}{S_i S_j} \int_{V_i} \int_{V_j} \frac{\boldsymbol{w}_i \cdot \boldsymbol{w}_j}{r_{ij}} dV_i dV_j = \sum_j L_{ij} \frac{\partial}{\partial t} I_j,\end{aligned} \tag{5.7.5}$$

where r_{ij} is the distance function between the volumes V_i and V_j and L_{ij} are the mutual inductances.

For the third term of (5.6.8), using $\nabla \cdot \boldsymbol{J}(\boldsymbol{r}) = J_i \nabla \cdot \boldsymbol{w}_i(\boldsymbol{r}) = 0$ in the

volume V_i, we obtain

$$\begin{aligned} -\int_V \boldsymbol{w}_i(\boldsymbol{r}) \cdot \nabla\Phi(\boldsymbol{r},t)dV = -\int_{V_i} \nabla\cdot\left(\boldsymbol{w}_i(\boldsymbol{r})\Phi(\boldsymbol{r},t)\right) dV_i = \\ = \frac{1}{S_\alpha}\int_{S_\alpha} \Phi(\boldsymbol{r},t)dS_\alpha - \frac{1}{S_\beta}\int_{S_\beta} \Phi(\boldsymbol{r},t)dS_\beta = \Phi_\alpha - \Phi_\beta = \Phi_i, \end{aligned} \tag{5.7.6}$$

where S_α, S_β are the surface at the edge of the volume V_i as shown in figure 5.7.1, Φ_α and Φ_β are the potential in the surfaces S_α and S_β and Φ_i their difference.

For the fourth term of (5.6.8) we derive

$$-\int_V \boldsymbol{w}_i(\boldsymbol{r}) \cdot \frac{\partial}{\partial t}\boldsymbol{A}_e(\boldsymbol{r},t) = U_i, \tag{5.7.7}$$

where U_i is the voltage drop due to $\boldsymbol{A}_e$ along the length of the volume.

Plugging all together we get an equation for each I_i

$$R_i I_i + \sum_j L_{ij}\frac{\partial}{\partial t} I_j = \Phi_i - U_i. \tag{5.7.8}$$

Using matrix notation we obtain

$$\mathcal{R}\mathcal{I} + \mathcal{L}\frac{\partial}{\partial t}\mathcal{I} = \mathcal{V} - \mathcal{U}. \tag{5.7.9}$$

This is the constitutive equation for a network of lumped elements that can be solved with one of the Kirchoff laws (see chapter 6).

Chapter 6

Network Analysis

6.1 Introduction

The study of eddy currents using a R-L network brings us to a modification of Kirchoff laws in order to include the effect of magnetic field change.

6.2 Steady State Analysis

In the steady state analysis we can neglect the effects of accumulation of magnetic energy and consider only a resistive network.

6.2.1 Node Analysis

An electrical network can be represented as an orientated graph. Assume the oriented graph composed by N nodes and B branches. If we number nodes and branches, we can describe the graph using the so-called complete incidence matrix $\mathcal{A}_a : N \times B$, defined as follow:

$$\mathcal{A}_{mn} = \begin{cases} 1 & \text{if branch } n \text{ exit from node } m, \\ -1 & \text{if branch } n \text{ enter in node } m, \\ 0 & \text{otherwise.} \end{cases} \tag{6.2.1}$$

The incidence matrix, for the graph in the figure 6.2.1, reads:

$$\mathcal{A}_a = \begin{pmatrix}
1 & 0 & 0 & 0 & 0 & 0 & 0 & 0 & 1 & 0 & 0 & 0 & 0 & 0 & 0 & -1 & 0 & 0 & 0 & 0 \\
0 & 1 & 0 & 0 & 0 & 0 & 0 & 0 & 0 & 1 & 0 & 0 & 0 & 0 & 0 & 1 & 0 & 0 & 0 & 0 \\
0 & 0 & 1 & 0 & 0 & 0 & 0 & 0 & 0 & 0 & 1 & 0 & 0 & 0 & 0 & 0 & -1 & 0 & 0 & 0 \\
0 & 0 & 0 & 1 & 0 & 0 & 0 & 0 & 0 & 0 & 0 & 1 & 0 & 0 & 0 & 0 & 0 & 1 & 0 & 0 \\
0 & -1 & 0 & 0 & 1 & 0 & 0 & 0 & -1 & 0 & 0 & 0 & 1 & 0 & 0 & 0 & 0 & 0 & 0 & 0 \\
-1 & 0 & 0 & 0 & 0 & 1 & 0 & 0 & 0 & 0 & -1 & 0 & 0 & 1 & 0 & 0 & 0 & 0 & -1 & 0 \\
0 & 0 & 0 & -1 & 0 & 0 & 1 & 0 & 0 & -1 & 0 & 0 & 0 & 0 & 1 & 0 & 0 & 0 & 1 & 0 \\
0 & 0 & -1 & 0 & 0 & 0 & 0 & 1 & 0 & 0 & 0 & -1 & 0 & 0 & 0 & 1 & 0 & 0 & 0 & 0 \\
0 & 0 & 0 & 0 & -1 & 0 & 0 & 0 & 0 & 0 & 0 & 0 & 0 & -1 & 0 & 0 & 0 & 0 & -1 & 0 \\
0 & 0 & 0 & 0 & 0 & 0 & -1 & 0 & 0 & 0 & 0 & 0 & -1 & 0 & 0 & 0 & 0 & 0 & 1 & 0 \\
0 & 0 & 0 & 0 & 0 & -1 & 0 & 0 & 0 & 0 & 0 & 0 & 0 & 0 & -1 & 0 & 0 & 0 & 0 & -1 \\
0 & 0 & 0 & 0 & 0 & 0 & 0 & -1 & 0 & 0 & 0 & 0 & 0 & 0 & -1 & 0 & 0 & 0 & 0 & 1
\end{pmatrix} \tag{6.2.2}$$

Sums of columns are always 0, the rank of $\mathcal{A}_a$ is $N-1$.

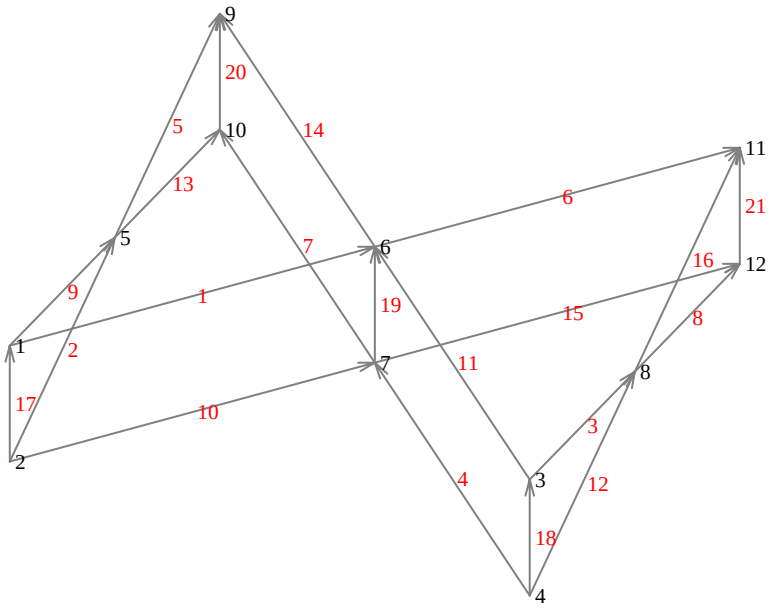

Figure 6.2.1 A graph of 21 branches and 12 nodes. Number in red refer to strand labelling, in black node labelling

For a network we can build the incidence matrix $\mathcal{A} : (N-1) \times B$ defined as $\mathcal{A}_a$ without one row.

We can define the admittance matrix $\mathcal{G} : B \times B$ in which the element $\mathcal{G}_{ab} = i_a/v_b$ is the contribution of voltage v_a to the current i_b and voltage source matrix $\mathcal{U} : B \times 1$ where $\mathcal{U}_{b1}$ is the voltage source of branch b.

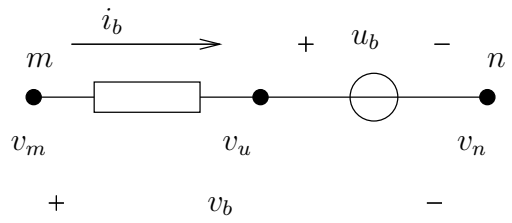

Figure 6.2.2 Definitions on branch b between nodes m and n

Using figure 6.2.2 we can write a constitutive equation

$$\begin{aligned} i_b &= G_b(v_m - v_u) \\ u_b &= v_u - v_n \\ i_b &= G_b(v_m - v_n) - G_b u_b, \end{aligned} \tag{6.2.3}$$

Using incidence matrix we can derive for all nodes the matrix equation:

$$\mathcal{I} = \mathcal{G}\mathcal{A}^T\mathcal{V}_n - \mathcal{G}\mathcal{U}. \tag{6.2.4}$$

where $\mathcal{V}_n$ is the node potential matrix, $\mathcal{I}$ is the branch current matrix and $\mathcal{V} = \mathcal{A}^T\mathcal{V}_n$ is the branch voltage matrix.

Using the Kirchoff current law written for incidence matrix,

$$\mathcal{A}\mathcal{I} = 0, \tag{6.2.5}$$

the previous equation can be solved

$$\mathcal{V}_n = (\mathcal{A}\mathcal{G}\mathcal{A}^T)^{-1}\mathcal{A}\mathcal{G}\mathcal{U}. \tag{6.2.6}$$

6.2.2 Mesh Analysis

In a network of N nodes and B branches we can define the $(N-1)$-branches tree set and $(B-N+1)$-branches co-tree set. A mesh is set of branches that represent a closed path between nodes. Each co-tree branch defines a mesh whose currents is equal to the co-tree branch current.

A set of independent meshes can be represented using the so-called mesh matrix $\mathcal{M} : (B-N+1) \times B$ defined as follow:

$$\mathcal{M}_{ab} = \begin{cases} 1 & \text{if branch } b \text{ belongs to loop } a \text{ with same orientation,} \\ -1 & \text{if branch } b \text{ belongs to loop } a \text{ with opposit orientation,} \\ 0 & \text{otherwise.} \end{cases} \tag{6.2.7}$$

For example a set of meshes of the graph in the figure 6.2.1, has the following mesh matrix

$$\mathcal{M} = \begin{pmatrix} 0 & 1 & 0 & 0 & 0 & 0 & -1 & 0 & 0 & -1 & 0 & 0 & 1 & 0 & 0 & 0 & 0 & 0 & 0 & 0 & 0 \\ 0 & 0 & 0 & 1 & 0 & 0 & 0 & -1 & 0 & 0 & 0 & -1 & 0 & 0 & 1 & 0 & 0 & 0 & 0 & 0 & 0 \\ 0 & -1 & 0 & 0 & 0 & 0 & 0 & 0 & 1 & 0 & 0 & 0 & 0 & 0 & 0 & 0 & 1 & 0 & 0 & 0 & 0 \\ 0 & 0 & 0 & -1 & 0 & 0 & 0 & 0 & 0 & 0 & 1 & 0 & 0 & 0 & 0 & 0 & 0 & 1 & -1 & 0 & 0 \\ 1 & 0 & 0 & 0 & 0 & 0 & 0 & 0 & 0 & -1 & 0 & 0 & 0 & 0 & 0 & 0 & 1 & 0 & -1 & 0 & 0 \\ 0 & 0 & 1 & 0 & 0 & 0 & 0 & 0 & 0 & 0 & 0 & -1 & 0 & 0 & 0 & 0 & 0 & 1 & 0 & 0 & 0 \\ 0 & 0 & 0 & 0 & 0 & 1 & 0 & 0 & 0 & 0 & 0 & 0 & 0 & -1 & 0 & 0 & 0 & 0 & 0 & -1 & 0 \\ 0 & 0 & 0 & 0 & 0 & 0 & 1 & 0 & 0 & 0 & 0 & 0 & 0 & 0 & 0 & -1 & 0 & 0 & 0 & 1 & 0 & -1 \\ 0 & 0 & 0 & 0 & 0 & 0 & 0 & -1 & 0 & 0 & 0 & 0 & 0 & 0 & 1 & 0 & 0 & 0 & 1 & -1 & 0 \\ 0 & 0 & 0 & 0 & 0 & 0 & 0 & 0 & -1 & 0 & 0 & 0 & 0 & 0 & 0 & 0 & 1 & 0 & 0 & 0 & -1 \end{pmatrix} \tag{6.2.8}$$

where the co-tree set is composed by branch $\{1, 2, 3, 4, 5, 6, 9, 14, 16, 18\}$ and the tree set is $\{7, 8, 10, 11, 12, 13, 15, 17, 19, 20, 21\}$.

All the branch currents can be derived using this matrix equation

$$\mathcal{I} = \mathcal{M}^T \mathcal{I}_M, \tag{6.2.9}$$

where $\mathcal{I}_M : (B - N + 1) \times 1$ is the mesh current matrix. As we did before we can write a constitutive equation

$$\mathcal{V} = \mathcal{R}\mathcal{I} + \mathcal{U} = \mathcal{R}\mathcal{M}^T \mathcal{I}_M + \mathcal{U}, \tag{6.2.10}$$

where $\mathcal{R} = \mathcal{G}^{-1}$. Using the Kirchoff voltage law

$$\mathcal{M}\mathcal{V} = 0, \tag{6.2.11}$$

we can solve the system

$$\mathcal{M}\mathcal{R}\mathcal{M}^T \mathcal{I}_M + \mathcal{M}\mathcal{U} = 0 \tag{6.2.12}$$

in

$$\begin{aligned} \mathcal{I}_M &= -(\mathcal{M}\mathcal{R}\mathcal{M}^T)^{-1} \mathcal{M}\mathcal{U} \\ \mathcal{I} &= -\mathcal{M}^T \mathcal{R}_M^{-1} \mathcal{U}_M, \end{aligned} \tag{6.2.13}$$

where $\mathcal{R}_M = \mathcal{M}\mathcal{R}\mathcal{M}^T$ and $\mathcal{U}_M = \mathcal{M}\mathcal{U}$. $\mathcal{R}_M$ is the matrix of mesh resistance, the diagonal elements of $\mathcal{R}_M$ are the total resistance of each mesh and the off-diagonal are the algebraic sum of the common resistances between meshes. $\mathcal{U}_M$ is the sum of the voltage sources in each mesh.

6.3 Link between Node and Mesh Analysis

The incidence matrix $\mathcal{A}$ and the mesh matrix $\mathcal{M}$ are linked by the relation

$$\mathcal{A}\mathcal{M}^T = 0. \tag{6.3.1}$$

In fact this product perform the scalar product between every row of $\mathcal{M}$ that represents the meshes and every row of $\mathcal{A}$ that represent the branches that belongs to the nodes. Every node in a mesh has to belong to two branches in which the mesh current respectively enters and exits, the dot product checks this condition choosing the branches that belongs to a node and summing their orientations.

If we use tree and co-tree technique to find meshes, we can partition $\mathcal{A}$ in $(\mathcal{A}_C|\mathcal{A}_T)$ where $\mathcal{A}_T$ contains the tree branches informations and $\mathcal{A}_C$ the co-tree informations. Also $\mathcal{M}$ can be partitioned in $(\mathcal{M}_C|\mathcal{M}_T)$. This yields that $\mathcal{A}_T$ is a non singular square matrix and $\mathcal{M}_C = \mathcal{E}$ the unit diagonal matrix. Using the previous relations (6.3.1) we can find

$$\begin{aligned} \mathcal{A}_C\mathcal{M}_C^T + \mathcal{A}_T\mathcal{M}_T^T &= 0 \\ \mathcal{M}_T^T &= -\mathcal{A}_T^{-1}\mathcal{A}_C. \end{aligned} \tag{6.3.2}$$

We can also generalize the concept of meshes noting that if we make a linear combination of two rows of mesh matrix $\mathcal{M}$ we do not change his algebraic properties. We can consider a mesh as a particular vector in the branch space that belongs to the null space of $\mathcal{A}$. The mesh matrix can be determinated by a set of linearly independent mesh. In fact the nullity of $\mathcal{A}$ is equal the number of independent meshes.

6.3.1 Circuit in an External Time Varying Magnetic Field

If we want to include the effects of an external magnetic field we should include in the Kirchoff law the Faraday induction equation for a closed loop

$$u = -\frac{\partial}{\partial t}\int \boldsymbol{B}\cdot\boldsymbol{dS} = -\frac{\partial}{\partial t}\oint \boldsymbol{A}\cdot\boldsymbol{dl}, \tag{6.3.3}$$

where $\boldsymbol{A}$ is the vector potential, $\boldsymbol{B} = \nabla\times\boldsymbol{A}$ is the magnetic field.

We discretize $\boldsymbol{A}$ assigning it to each node a $\boldsymbol{A}_n$. Moreover we approximate $\boldsymbol{A}$ linear with the distance. With this assumption Faraday law integral (6.3.3) becomes:

$$\oint \boldsymbol{A}\cdot\boldsymbol{dl} \approx \sum_n \frac{\boldsymbol{A}_n + \boldsymbol{A}_{n+1}}{2}\cdot(\boldsymbol{r}_{n+1} - \boldsymbol{r}_n) \tag{6.3.4}$$

for every n that belongs to the loop.

As an example we can study the circuit in the figure 6.3.3, where only $\frac{\partial}{\partial t}B_{0z} \neq 0$.

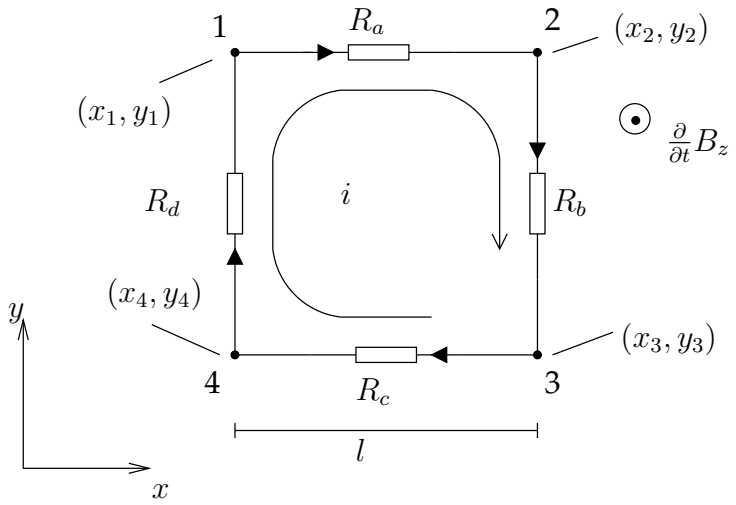

Figure 6.3.3 Simple circuit in a homogeneous time-varying B_{0z} field.

The solution is:

$$(R_a + R_b + R_c + R_d)i = \frac{\partial}{\partial t} B_{0z} l^2. \tag{6.3.5}$$

For a homogeneous magnetic field,

$$\boldsymbol{B}(x, y, z) = \boldsymbol{B}_0 = B_{0x}\boldsymbol{e}_x + B_{0y}\boldsymbol{e}_y + B_{0z}\boldsymbol{e}_z, \tag{6.3.6}$$

a vector potential is

$$\begin{aligned} \boldsymbol{A}(x, y, z) &= \frac{1}{2}\boldsymbol{B}_0 \times \boldsymbol{r} \\ &= \frac{1}{2}\left((B_{0y}x - B_{0z}y)\boldsymbol{e}_x + (B_{0z}x - B_{0x}z)\boldsymbol{e}_y + (B_{0x}y - B_{0y}x)\boldsymbol{e}_z\right), \end{aligned} \tag{6.3.7}$$

the flux can be written, if $\frac{\partial}{\partial t}B_{0x} = 0$, $\frac{\partial}{\partial t}B_{0y} = 0$, as

$$\begin{aligned} \frac{\partial}{\partial t} B_{0z} l^2 = \oint \frac{\partial}{\partial t}\boldsymbol{A} \cdot \boldsymbol{dl} &= \sum_b \int_b \frac{\partial}{\partial t}\boldsymbol{A} \cdot \boldsymbol{dl} \\ &= u_a + u_b + u_c + u_d. \end{aligned} \tag{6.3.8}$$

The solution now can be written as:

$$(R_a + R_b + R_c + R_d)i = u_a + u_b + u_c + u_d. \tag{6.3.9}$$

The solution of this circuit is equal to the solution of circuit 6.3.4, in which $u = \int_b \frac{\partial}{\partial t}\boldsymbol{A} \cdot \boldsymbol{dl}$. In other words we can split the circulation of $\frac{\partial}{\partial t}\boldsymbol{A}$ and associate each portion to a circuit branch. Using the approximation seen above for $\boldsymbol{A}$ (see (6.3.4)), we obtain

$$u_a = \frac{\partial}{\partial t}\frac{A_{x1} + A_{x2}}{2}(x_2 - x_1) + \frac{\partial}{\partial t}\frac{A_{y1} + A_{y2}}{2}(y_2 - y_1). \tag{6.3.10}$$

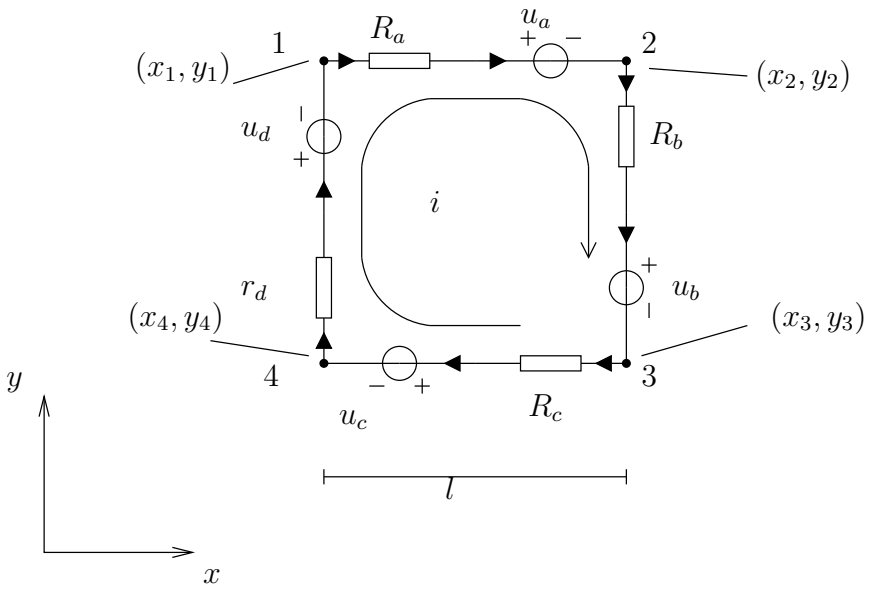

Figure 6.3.4 Simple circuit in a homogeneous B_{0z} field, where the effects B_{0z} is inside voltage sources u.

It is easy to prove that the solution is the same.

This leads us to reformulate the matrix equations including the contribution of magnetic field change.

If we define $\mathcal{X}$, $\mathcal{Y}$, $\mathcal{Z}$ as the node position matrices, $\mathcal{A}_x$, $\mathcal{A}_y$, $\mathcal{A}_z$ the node vector potential matrices and $\mathcal{A}_2$ the incidence matrix with all elements squared, we can write

$$\mathcal{U} = \frac{1}{2}\left((\mathcal{A}_2^T\frac{\partial}{\partial t}\mathcal{A}_x)(\mathcal{A}_a^T\mathcal{X}) + (\mathcal{A}_2^T\frac{\partial}{\partial t}\mathcal{A}_y)(\mathcal{A}_a^T\mathcal{Y}) + (\mathcal{A}_2^T\frac{\partial}{\partial t}\mathcal{A}_z)(\mathcal{A}_a^T\mathcal{Z})\right). \tag{6.3.11}$$

It is important to note that the vector potential and the scalar potential depend on the choice of the gauge. While node analysis, that use as unknowns the scalar potential, has to deal with this choice, mesh analysis using Kirchoff voltage law eliminates the ambiguity of gauging. Matrix multiplication $\mathcal{MU}$ perform a discrete path integral able to cancel all

the possible curl free parts of the discretized vector potential. In fact Kirchoff voltage law, in presence of a magnetic field, is an application of $\nabla \times (\boldsymbol{E} + \frac{\partial}{\partial t}\boldsymbol{A}) = 0$ instead of simply $\nabla \times \boldsymbol{E} = 0$ in normal network analysis.

6.4 Transient Analysis

For transient analysis we need to introduce the mutual inductance elements that takes into account the effect of a current change of one branch on another branch.

The constitutive equations in matrix form now reads:

$$\mathcal{V} = \mathcal{R}\mathcal{I} + \mathcal{L}\frac{\partial}{\partial t}\mathcal{I} + \mathcal{U}, \tag{6.4.1}$$

where $\mathcal{L}$ is such that diagonal elements are the self-inductances of each branch and the off-diagonal are the mutual-inductances.

If we use the Kirchoff voltage law (6.2.11) and the definition of mesh current (6.2.9) we obtain:

$$\mathcal{R}_M\mathcal{I}_M + \mathcal{L}_M\frac{\partial}{\partial t}\mathcal{I}_M + \mathcal{U}_M = 0, \tag{6.4.2}$$

where diagonal elements of $\mathcal{L}_M = \mathcal{M}\mathcal{L}\mathcal{M}^T$ are the self-inductances of each mesh and the off-diagonal are the mutual-inductances between meshes.

6.4.1 Numerical Approach

For a numerical integration in time domain of equation (6.4.2) we can choose the trapezoidal approximation for the time derivative. That is

$$\begin{aligned}
\frac{\partial}{\partial t}\mathcal{I}\left(\frac{t_{k+1}+t_k}{2}\right) &\approx \frac{\mathcal{I}(t_{k+1}) - \mathcal{I}(t_k)}{h},\\
\mathcal{I}\left(\frac{t_{k+1}+t_k}{2}\right) &\approx \frac{\mathcal{I}(t_{k+1}) + \mathcal{I}(t_k)}{2},\\
\mathcal{V}\left(\frac{t_{k+1}+t_k}{2}\right) &\approx \frac{\mathcal{V}(t_{k+1}) + \mathcal{V}(t_k)}{2},\\
\mathcal{U}\left(\frac{t_{k+1}+t_k}{2}\right) &\approx \frac{\mathcal{U}(t_{k+1}) + \mathcal{U}(t_k)}{2},
\end{aligned} \tag{6.4.3}$$

where $t_k = kh$ and h is the time step size.

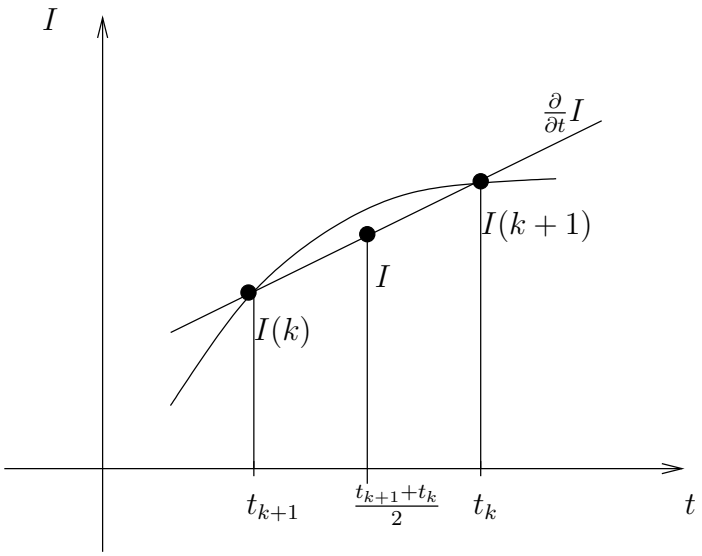

Figure 6.4.5 Trapezoidal approximation for I and $\frac{\partial}{\partial t}I$

Trapezoidal approximation uses values of the quantity at steps t_k and t_{k+1} in order to approximate the differential equation at $(t_{k+1} + t_k)/2$. In the figure 6.4.5 is show a graphic representation.

The matrix equation (6.4.1) approximated in $t = (t_{k+1} + t_k)/2$ becomes

$$\mathcal{V}(k) + \mathcal{V}(k+1) = \mathcal{R}\Big(\mathcal{I}(k) + \mathcal{I}(k+1)\Big) + \\ + \frac{2}{h}\mathcal{L}\Big(\mathcal{I}(k+1) - \mathcal{I}(k)\Big) + \mathcal{U}(k) + \mathcal{U}(k+1). \quad (6.4.4)$$

Rearranging the terms yields

$$\mathcal{V}(k) + \mathcal{V}(k+1) = \\ \left(\mathcal{R} + \frac{2}{h}\mathcal{L}\right)\mathcal{I}(k+1) + \left(\mathcal{R} - \frac{2}{h}\mathcal{L}\right)\mathcal{I}(k) + \mathcal{U}(k) + \mathcal{U}(k+1). \quad (6.4.5)$$

Using the equation for mesh currents (6.2.9) and left multiplying by $\mathcal{M}$ gives

$$\mathcal{M}\left(\mathcal{R} + \frac{2}{h}\mathcal{L}\right)\mathcal{M}^T\mathcal{I}_M(k+1) = \\ - \mathcal{M}\left(\mathcal{R} - \frac{2}{h}\mathcal{L}\right)\mathcal{M}^T\mathcal{I}_M(k) - \mathcal{M}\mathcal{U}(k) - \mathcal{M}\mathcal{U}(k+1), \quad (6.4.6)$$

which can be solved:

$$\mathcal{I}_M(k+1) = -\mathcal{Z}_A^{-1}\left(\mathcal{Z}_B\mathcal{I}_M(k) + \mathcal{M}\mathcal{U}(k) + \mathcal{M}\mathcal{U}(k+1)\right), \tag{6.4.7}$$

where $\mathcal{Z}_A = \mathcal{M}\left(\mathcal{R} + \frac{2}{h}\mathcal{L}\right)\mathcal{M}^T$ and $\mathcal{Z}_B = \mathcal{M}\left(\mathcal{R} - \frac{2}{h}\mathcal{L}\right)\mathcal{M}^T$.

Trapezoidal approximation leads to a local error proportional to h^3 and it is stable ([MS96]).

6.5 Spectral Analysis of Mesh Method Solutions

6.5.1 Steady State

$\mathcal{R}_M$ in equation (6.2.13) can be diagonalised using the transformation

$$\mathcal{R}_M = \mathcal{D}\mathcal{R}_D\mathcal{D}^{-1}, \tag{6.5.1}$$

where the columns of $\mathcal{D}$ are the eigenvectors $\mathcal{P}_\lambda$ corresponding to the eigenvalues $r_\lambda = \mathcal{R}_{D_{\lambda\lambda}}$ and $\mathcal{D}^{-1} = \mathcal{D}^T$ because $\mathcal{R}_M$ is real and symmetric.

We can define the matrices

$$\begin{aligned} \mathcal{M}_D &= \mathcal{D}^T\mathcal{M}, \\ \mathcal{I}_D &= \mathcal{M}_D\mathcal{I}, \\ \mathcal{U}_D &= \mathcal{M}_D\mathcal{U}. \end{aligned} \tag{6.5.2}$$

If we left multiply for $\mathcal{D}^T$, use $\mathcal{D}\mathcal{D}^T = \mathcal{E}$ and apply last definition in the system for the mesh currents (6.2.12) we obtain

$$\begin{aligned} \mathcal{M}\mathcal{R}\mathcal{M}^T\mathcal{I}_M + \mathcal{M}\mathcal{U} &= 0 \\ \mathcal{D}^T\mathcal{M}\mathcal{R}\mathcal{M}^T(\mathcal{D}\mathcal{D}^T)\mathcal{M}\mathcal{I} + \mathcal{D}^T\mathcal{M}\mathcal{U} &= 0, \\ \mathcal{M}_D\mathcal{R}\mathcal{M}_D^T\mathcal{M}_D\mathcal{I} + \mathcal{M}_D^T\mathcal{U}_D &= 0, \\ \mathcal{R}_D\mathcal{I}_D + \mathcal{M}_D^T\mathcal{U}_D &= 0. \end{aligned} \tag{6.5.3}$$

As we did, we can solve this system as

$$\mathcal{I} = -\mathcal{M}_D^T\mathcal{R}_D^{-1}\mathcal{U}_D. \tag{6.5.4}$$

where $\mathcal{R}_D = \mathcal{M}_D\mathcal{R}\mathcal{M}_D^T$.

We can recognize that $\mathcal{M}_D$ is a new mesh matrix, $\mathcal{I}_D$ are the currents of the meshes, $\mathcal{U}_D$ is are the voltages sources of the meshes and $\mathcal{R}_D$ is the

resistance of the mesh. These meshes are "generalized" mesh because each row of $\mathcal{M}_D$, that represent a mesh, it is not more composed by 1, 0, -1, but it is fully populated of non integer values. This means that the mesh are no more a set of branches, but a set of coefficients associated to each branch. This coefficients represents the fraction of the current of branches that belongs to each current of meshes. Then these meshes do not interact each others because $\mathcal{R}_D$ is diagonal. Each of them represent a solution of the system if the system is excited by $\mathcal{U}_D$ such that each component is 0 but the component relative to the mesh that is equal 1. In [AIS98] they are called eigen-currents and can be considered the modes of the system.

If we call $\mathcal{Q}_\lambda$ the λth row of $\mathcal{M}_D$, r_λ the λth eigenvalue, u_λ the λth source, we obtain from (6.5.4)

$$\begin{aligned} \mathcal{I}_i &= -\sum_\lambda \mathcal{M}_{D_{\lambda i}} \frac{\mathcal{U}_{D_\lambda}}{\mathcal{R}_{D_\lambda}} \Rightarrow \\ \mathcal{I} &= -\sum_\lambda \frac{u_\lambda}{r_\lambda} \mathcal{Q}_\lambda \end{aligned} \tag{6.5.5}$$

We have expressed the currents as a weighted sum of eigen-currents. The weight depends on the ratio between the resistance of the relative meshes and the voltage associated. Eigen-currents can be calculated using the first of equations (6.5.2). From that we obtain:

$$\mathcal{Q}_\lambda = \mathcal{M}^T \mathcal{P}_\lambda \tag{6.5.6}$$

Thus $\mathcal{Q}_\lambda$ is the eigenvector corresponding the eigenvalue r_λ expressed in terms of branches, instead of $\mathcal{P}_\lambda$ that is expressed in terms of mesh currents.

6.5.2 Transient

We can do the same as done before, solving the equation for the transient (6.4.2).

The solution is ([Akh98])

$$\mathcal{I}_M = (\mathcal{E} - e^{\mathcal{L}_M^{-1}\mathcal{R}_M t})\mathcal{R}_M^{-1}\mathcal{U} = (\mathcal{E} - e^{\mathcal{W}t})\mathcal{R}_M^{-1}\mathcal{U} \tag{6.5.7}$$

where $\mathcal{E}$ is the unit matrix and $\mathcal{W} = \mathcal{L}_M^{-1}\mathcal{R}_M$.

If we diagonalise $\mathcal{W}$, we can write equation (6.5.7) as:

$$\mathcal{I}_M = \left(\mathcal{E} - \sum_\lambda \exp(w_\lambda t) \prod_{\lambda \neq \lambda'} \frac{\mathcal{W} - w_\lambda \mathcal{E}}{w_{\lambda'} - w_\lambda}\right) \mathcal{R}_M^{-1}\mathcal{U} \tag{6.5.8}$$

where eigenvalues w_λ of $\mathcal{W}$ represent the inverse of time constant spectrum of our system.

Chapter 7

Network Model for Eddy Currents

7.1 Introduction

Interstrand coupling currents are eddy currents generated by $\frac{\partial}{\partial t}\boldsymbol{B}$ across strands and copper inside a Rutherford-type cable. They produce losses, field errors and reduce the maximum transport currents during ramping. They are responsible of a limitation of cycle ramp rate in magnets.

Several models have been developed either assuming the cable as a continuum ([Car75], [CWM75], [Car77], [Cam80], [Cam81], [Cam82]), as a network of lumped elements ([Mor73], [ADO94], [AKOT95], [Ver95], [DO95], [Akh98], [AIS98], [Akh00b]) and as a network of distributed elements ([Tur74], [KS95], [KS96], [ABBR00], [Akh00a], [Akh01], [ABB01], [Akh02], [BRB00], [BBSS02], [BBR03], [BBF03],). For a comparison of these models refer to [Akh00a].

7.2 Network Model

The Rutherford-type cableis represented as a network of superconducting thin wires and discrete contact resistances. Figure 7.2.1 shows a modelized version a twist pitch length L_p portion of a cable.

As seen in chapter 6, we can study the circuit with mesh or nodal analysis. Although node analysis is easier to implement, mesh analysis is used. The main reason is that with node analysis should used conductances. Conductances of branches representing strands diverge when they are in the superconducting state and this leads to numerical instabilities.

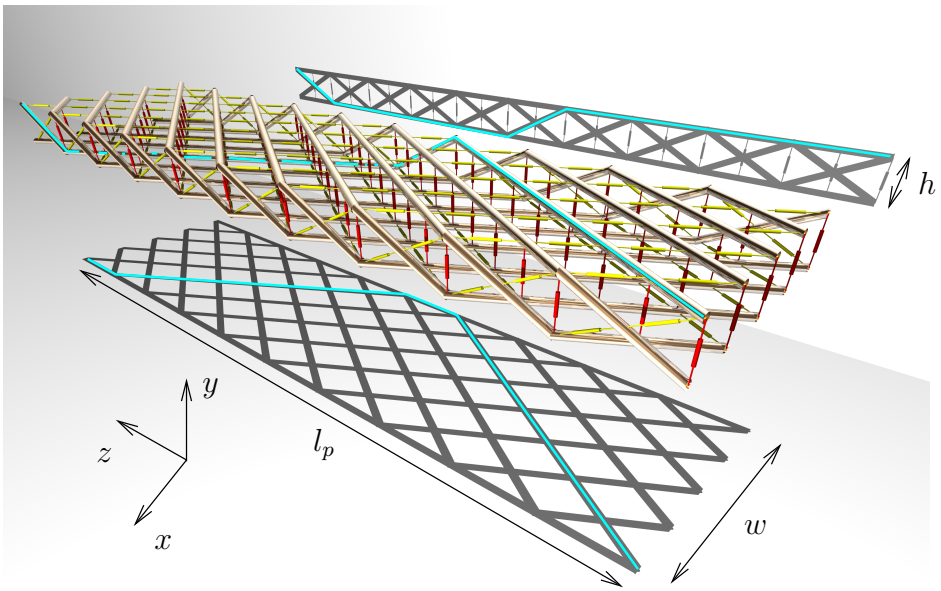

Figure 7.2.1 Network model of a twist pitch length (L_p) portion of a 10 strands cable. The dashed cyan line represent the spatial disposition of a strand in a twist pitch.

7.3 Geometric Parameters

From figure 7.2.1 it easy to see that there is a sub-periodicity of a $L_b = L_p/N_s$, where N_s is the number of strands (see figure 7.3.2).

This part of the cable is called band.

From a geometric point of view, a cable is defined by (see figure 7.2.1)

- N_s: number of strands,
- N_b: number of bands,
- l_p: twist pitch,
- h_1, h_2: height,
- w: width.

From these quantities it is possible to determine physical dimension of the cable and the quantity associate to the graph. In the following we make use of definitions:

- $N = 2N_sN_b + N_s$: number of nodes,

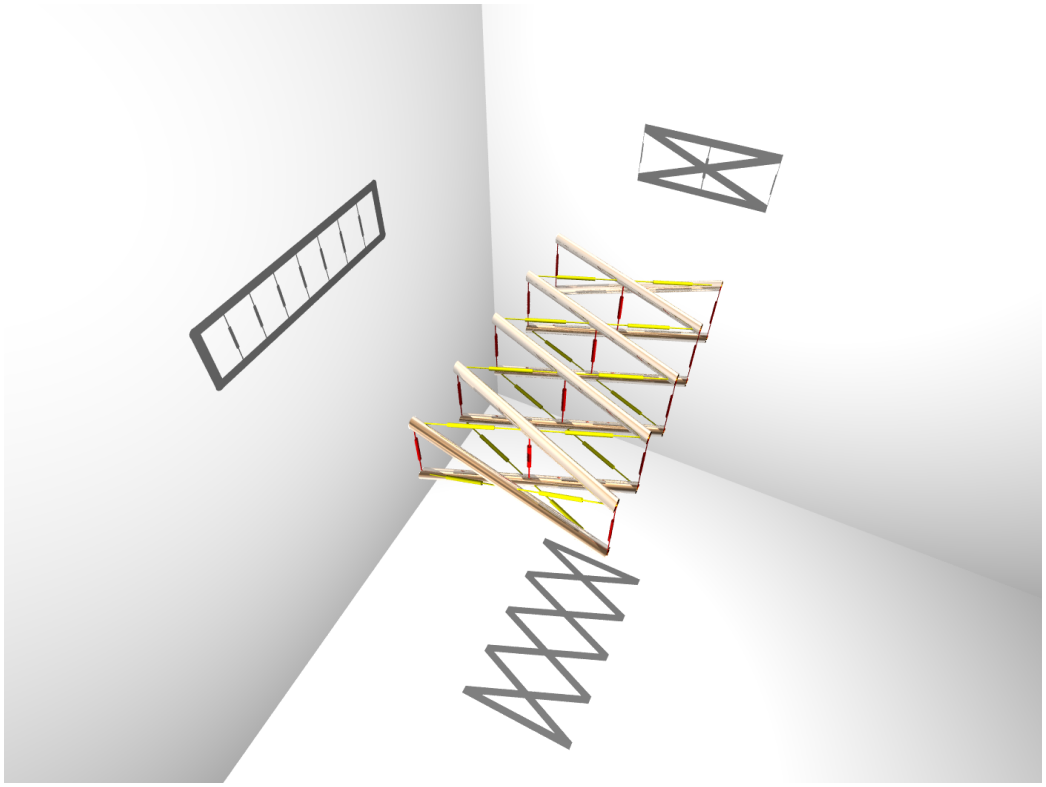

Figure 7.3.2 Periodic band of a 10 **strands cable**

- $B_s = 2N_sN_b$: number of strand branches,
- $B_a = 2N_sN_b$: number of adjacent resistance branches,
- $B_c = (N_s - 1)N_b + N_s/2$: number of cross resistance branches
- $B = B_s + B_a + B_c = (5N_s - 1)N_b + N_s/2$: total number of branches,
- $M = B - N + 1 = (3N_s - 1)N_b - N_s/2 + 1$: number of independent meshes
- $l_b = l_pN_s$: length of a band
- $l_c = N_bl_b = l_pN_b/N_s$: length of the cable

In figure 7.3.3 the graph for one band of 10-strand cable is shown . We assume that z-axes correspond to the longitudinal direction of the cable, x the width direction and y the height.

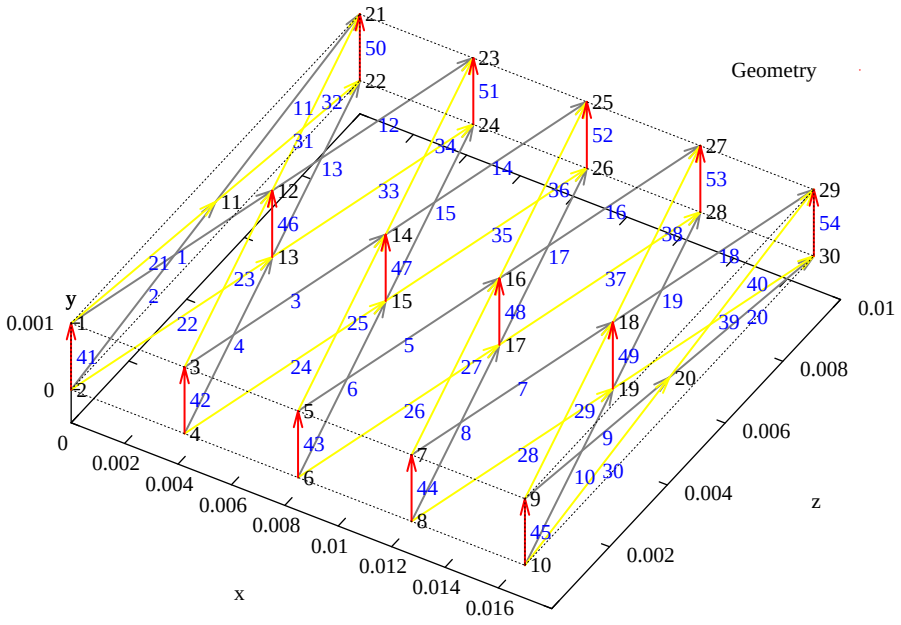

Figure 7.3.3 Graph a one band of 10-strands cable. Black arrows are branches that represent strands, red arrows represent cross resistances, yellow arrows represents adjacent resistances. Blue numbers label branch and black numbers nodes.

7.4 Lumped elements

7.4.1 Strand Resistances

Resistance in the strand is determined by the presence of two kind of electrons. Superconducting electrons that are inside the Nb-Ti if it is in the superconducting state, and normal electrons that are inside copper and Nb-Ti as well. For field errors currents of normal conducting electrons are not important because it is small compared to the super-conducting one.

Thus strands can be considered having zero conductance until Nb-Ti is in the superconducting state. Anyway it is interesting to have the possibility to associate a non zero resistance and calculate its effects, e.g. in use of a quench.

7.4.2 Contact Resistances

Resistance between strands is determined by an oxide layer on cable ([Wil97]). There are two kind of resistances: cross resistances (R_c) between strands in the upper and lower layer and adjacent resistances (R_a) between same layer strands on the on horizontal plane.

R_c values have been directly measured and indirectly estimated for LHC cables [WLR+97]. Their values vary randomly across the cable in width and length, vary from cable to cable, and vary for the same cable during process for magnets fabrication. In the figure 7.4.4 is showed the results of a series of measures of the mean of the cross resistance R_c in some LHC cables. We can see that values vary one order of magnitude from $20\,\mu\Omega$ to $200\,\mu\Omega$.

R_a should have slightly greater values than R_c because the contact surface between two adjacent strands is greater than the cross one. But their effects on interstrand coupling currents is small and their values have not been measured.

In figure 7.4.5 we can see the variation of the inverse of cross-resistance in a single magnets. Values represents the estimated mean of cross resistance in each cable depending of its position in the magnet cross section.

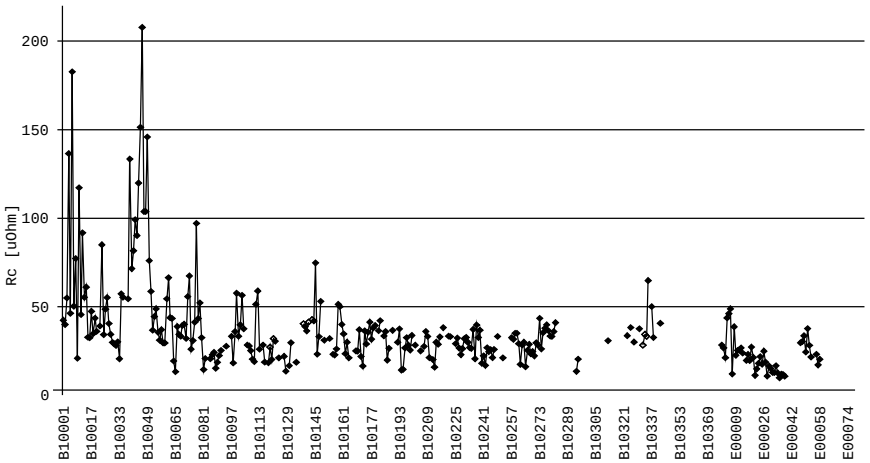

Figure 7.4.4 Measurements of the mean of R_c in LHC cables. Data provided by D. Ritcher

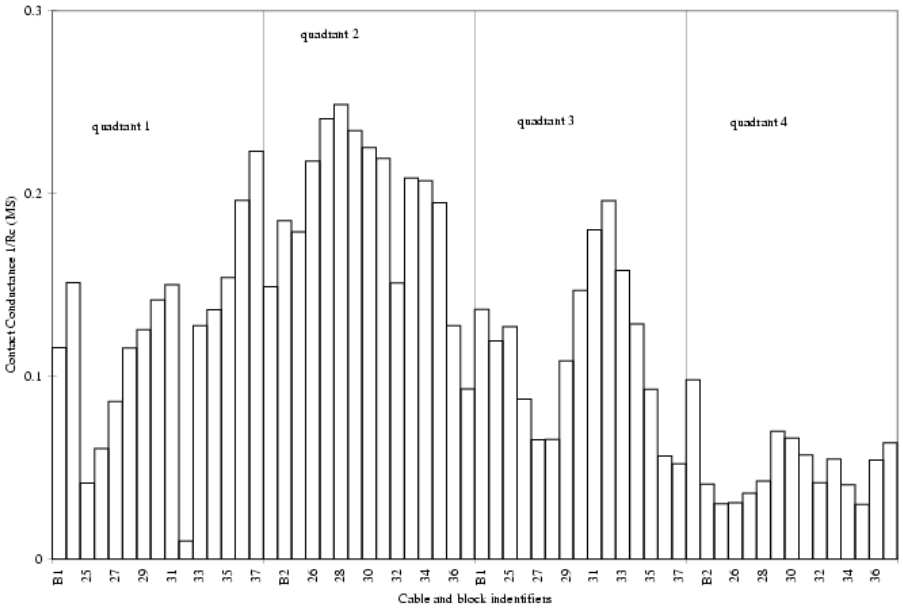

Figure 7.4.5 Cross conductance ($1/R_c$) of different cables of the same magnet. Data provided by R. Wolf.

7.4.3 Branch Inductances

Each branch has a self-inductance and a mutual-inductance with respect to the other branches. Calculation of this inductances is difficult task because the usual formulas loose their validity when the section area of the conductor is comparable with the length and distance of the other branch. There is no accordance on what formulas or technique are used (see [VtKL+95], [KS95], [ADMS93], [SM97], [ABBR00]).

A good estimation of inductances can be found calculating it for thin wires and considering a thick wire composed by thin wire.

The general formula for calculating self and mutual inductances is (see (5.7.5)) is:

$$\begin{aligned} L_{ij} = \frac{\mu}{4\pi}\frac{1}{S_i S_j}\int_{V_i}\int_{V_j}\frac{\boldsymbol{w}_i\cdot\boldsymbol{w}_j}{r_{ij}}dV_i dV_j = \\ \frac{\mu}{4\pi}\frac{1}{S_i S_j}\int_{S_i}\int_{S_j}\int_{l_i}\int_{l_j}\frac{\boldsymbol{w}_i\cdot\boldsymbol{w}_j}{r_{ij}}dl_i dl_j dS_i dS_j. \end{aligned} \tag{7.4.1}$$

For a thin wires becomes:

$$L_{ij} = \frac{\mu}{4\pi}\int_{l_i}\int_{l_j}\frac{\boldsymbol{w}_i\cdot\boldsymbol{w}_j}{r_{ij}}dl_i dl_j. \tag{7.4.2}$$

Self inductances

Self-inductance for a thick wire can be calculated noting that the wire can be thought composed of thin parallel wires. Formula for mutual inductance of parallel thin wires can be calculated solving the integral (7.4.2)

$$\begin{aligned} L(l/d) = \frac{\mu}{4\pi}\int_0^l\int_0^l\frac{1}{\sqrt{d^2+(l_i-l_j)^2}}dl_i dl_j = \\ \frac{\mu}{4\pi}2l\left[\log\left(\frac{l}{d}+\sqrt{1+\frac{l^2}{d^2}}\right)-\sqrt{1+\frac{d^2}{l^2}}+\frac{d}{l}\right], \end{aligned} \tag{7.4.3}$$

where d is the distance between wires and l is the length.

For calculating the self inductance we should average this formula for every distance between the points inside the section. That is solving the integral

$$L = \frac{1}{S^2}\int_S\int_S L(l/d)dSdS, \tag{7.4.4}$$

where d is the distance of two points of the surface S.

This integral cannot be computed easily because we should consider also short distances where $L(l/d)$ diverge.

Following [Gro46], for a wire whose thickness is smaller than length, the formula (7.4.3) can be approximated as

$$L(l/d) \approx L_a(l/d) = \frac{\mu}{4\pi} 2l \left(\log\left(\frac{2l}{d}\right) - 1 \right), \tag{7.4.5}$$

because $l/d \gg 1$.

The integral (7.4.4) is a sum of logarithms of the distance between two points in a region, thus its value is the integrand (7.4.3) in which the distance is the so-called geometric mean distance of the area from itself. In fact

$$\begin{aligned} \frac{1}{S^2} \int_S \int_S \log\left(\frac{2l}{d}\right) dS dS \approx \frac{1}{n} \sum_{i=1}^{n} \log \frac{2l}{d_i} = \\ = \log \sqrt[n]{\prod_{i=1}^{n} \frac{2l}{d_i}} = \log \frac{2l}{\sqrt[n]{\prod_{i=1}^{n} d_i}} \end{aligned}, \tag{7.4.6}$$

where d_i is the distance between every couple of points in the surface S. We recognize that

$$d_g = \lim_{n\to\infty} \sqrt[n]{\prod_{i=1}^{n} d_i} \tag{7.4.7}$$

is the geometric mean of d. Thus we can write

$$L \approx \frac{1}{S^2} \int_S \int_S L_a(l/d) dS dS = L_a(l/d_g). \tag{7.4.8}$$

For a round wire of radius r the geometric mean distance is

$$d_g = K_g r = e^{-1/4} r \approx 0.7788 r, \tag{7.4.9}$$

where r is the radius of the wire and K_g is the geometric mean distance factor.

In our case this approximation cannot be used because branch thickness has the same magnitude of the length. Nevertheless we can follow the same idea and define an equivalent mean distance d_e that depends on the shape as in the thin wire approximation and the length of the wire because $L(l/d)$ it is no more a pure logarithm like in (7.4.6), such that:

$$\frac{1}{S^2} \int_S \int_S L(l/d) dS dS = L(l/d_e), \tag{7.4.10}$$

or

$$\frac{1}{S^2}\int_S\int_S F(l/d)dSdS = F(l/d_e), \tag{7.4.11}$$

where $F(l/d)$ is the adimensional quantity

$$F(l/d) = \log\left(\frac{l}{d} + \sqrt{1+\frac{l^2}{d^2}}\right) - \sqrt{1+\frac{d^2}{l^2}} + \frac{d}{l}. \tag{7.4.12}$$

Solving the integral on the left of (7.4.11) and inverting $F(l/d_e)$, the equivalent mean distance d_e can be found for any shape and length.

For the circle of radius r, the admimensional quantity $F(l/d_e)$ will depend only on l/r because is the only adimensional quantity that can be constructed with r and l the free variables (Buckingamm theorem). Thus d_e will have the form

$$d_e = K(l/r)r \tag{7.4.13}$$

because $F(l/d_e)$ will be written as $F(\frac{1}{K(l/r)}\frac{l}{r})$.

Solving the integral (7.4.4) is difficult, even numerically, because it is a 4-D integral with a 2-D singular surface where $d = 0$. Anyway can be solved either with Monte-Carlo methods, or choosing Gauss points close but not in the singular surface ([HSS03]). Last choice is used for solving the integral for a round wire.

In analogy with geometric mean distance we define . The results for $K(l/r)$ is plotted in the figure 7.4.6.

For $l \gg r$, K approaches to K_g, the geometric mean distance factor, because we are in the thin wire approximation.

For $K(l/r)$ a fitting curve can be found:

$$K(l/r) = K_g - \frac{a}{l/r + \pi/5}, \tag{7.4.14}$$

where constant $a = 0.123178(119)$.

Resuming, the self inductance for a round wire is approximated by:

$$\begin{aligned} L &= \frac{\mu}{4\pi}2l\left(\log\left(\frac{l}{d_e} + \sqrt{1+\frac{l^2}{{d_e}^2}}\right) - \sqrt{1+\frac{{d_e}^2}{l^2}} + \frac{d_e}{l}\right), \\ d_e &= Kr, \\ K &= 0.7788 - \frac{0.1232}{l/r + 0.6283}. \end{aligned} \tag{7.4.15}$$

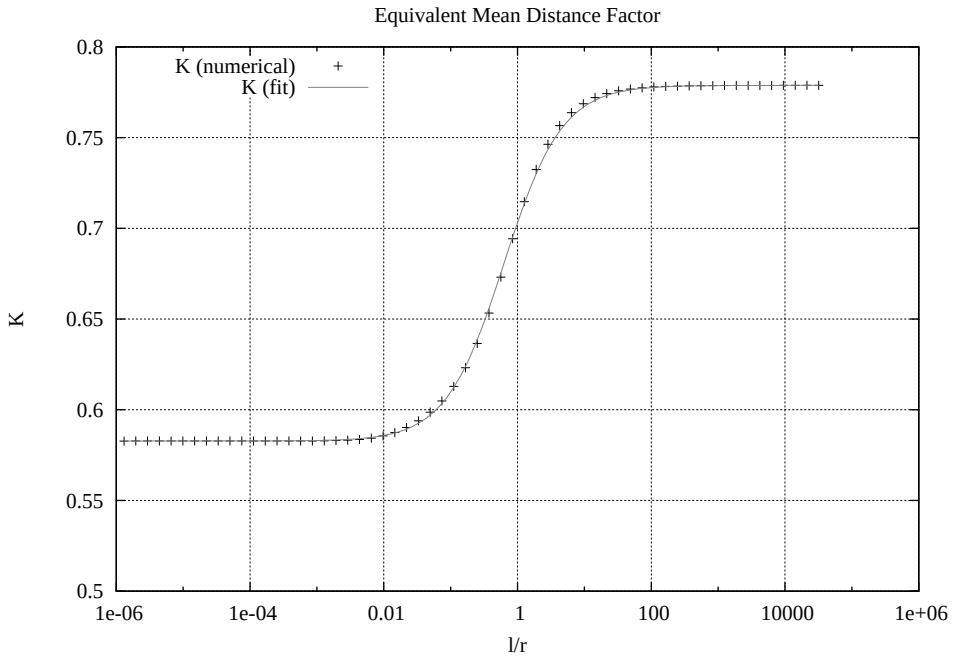

Figure 7.4.6 Equivalent mean distance for a round wire

Mutual inductances

Mutual inductances for thin wires can be calculated using formula (7.4.2). This formula can be approximated as:

$$L_{ij} = \frac{\mu}{4\pi} \frac{l_i l_j (\boldsymbol{w}_i \cdot \boldsymbol{w}_j)}{\langle r_{ij} \rangle} \tag{7.4.16}$$

where $\langle r_{ij} \rangle$ is the distance between the middle points of the segments l_i, l_j. This approximations strictly works when distance between the wires is large compared with their length and their thickness because the distance r_{ij} does not vary too much. It gives a good approximation also when wires are thick and close to each other. The approximation used is:

$$\frac{1}{V_i V_j} \int_{V_i} \int_{V_j} \frac{1}{r_{ij}} dV_i dV_j = \left\langle \frac{1}{r_{ij}} \right\rangle \approx \frac{1}{\langle r_{ij} \rangle}, \tag{7.4.17}$$

where the integral can been calculated using Gauss quadrature method and w are the weights ([PTVF01]).

Mesh inductances

The self and mutual inductance between loops are composed by an algebraic sum of the self and mutual inductances of the branch. These inductances scale as the inverse of the distance, but never vanish. In order to reduce calculation time, it has been assumed that mesh inductances lower than the highest value divided by a sparsification factor f. It makes the mesh matrix sparser and keeps the passivity and symmetry of circuit.

Using definition in section 6.5.2 we can formalise this assumption stating:

$$\mathcal{L}_{M_{ij}} = 0 \qquad \text{if} \qquad \mathcal{L}_{M_{ij}} < \max(\mathcal{L}_M)/f, \tag{7.4.18}$$

with $f > 0$.

We can see the effect of sparsification plotting non zero elements of mesh inductance matrix $\mathcal{L}_M$ for several sparsification factors, see section 6.5.2.

In order to validate this approximation we can calculate, for several sparsification factor f, the time spectrum of the system that is determinated by the eigenvalue of matrix $\mathcal{W}$.

In figure 7.4.8 we show a typical time constant spectrum for a 1 meter long cable. We can see how only a small sparsification factor slightly change the spectrum. We can have a better view plotting the modulus of relative deviation from the non sparsified spectrum. In figure 7.4.9 we can see how using $f = 100$ we have errors in the range of 1%.

7.5 Periodic Boundary Condition

In order to simulate an infinite long cable it is necessary to impone the currents at the boundary on a finite cable to be equal. This task can be implememented in several ways: adding the periodic conditions to the system as homogeneus equation of two variables and reducing the system; applying the conditions directly to the system adding the colums relative to the two periodic varibles and cancel an equation; modifing the mesh matrix. The last solution is the most straight foward but it cannot be used if the vector potential has a variation on z axis. The problem is in the product $\mathcal{MU}$. If a modified mesh matrix is used, then the flux of the loops which link the boundauries are evalueted using the vector potential in two different palces. If the vector potential has a gauge which leads to a bias in the voltage sources, the flux is erronealy affected by the bias that it is not nullified by the mesh matrix beacouse it is not the real one.

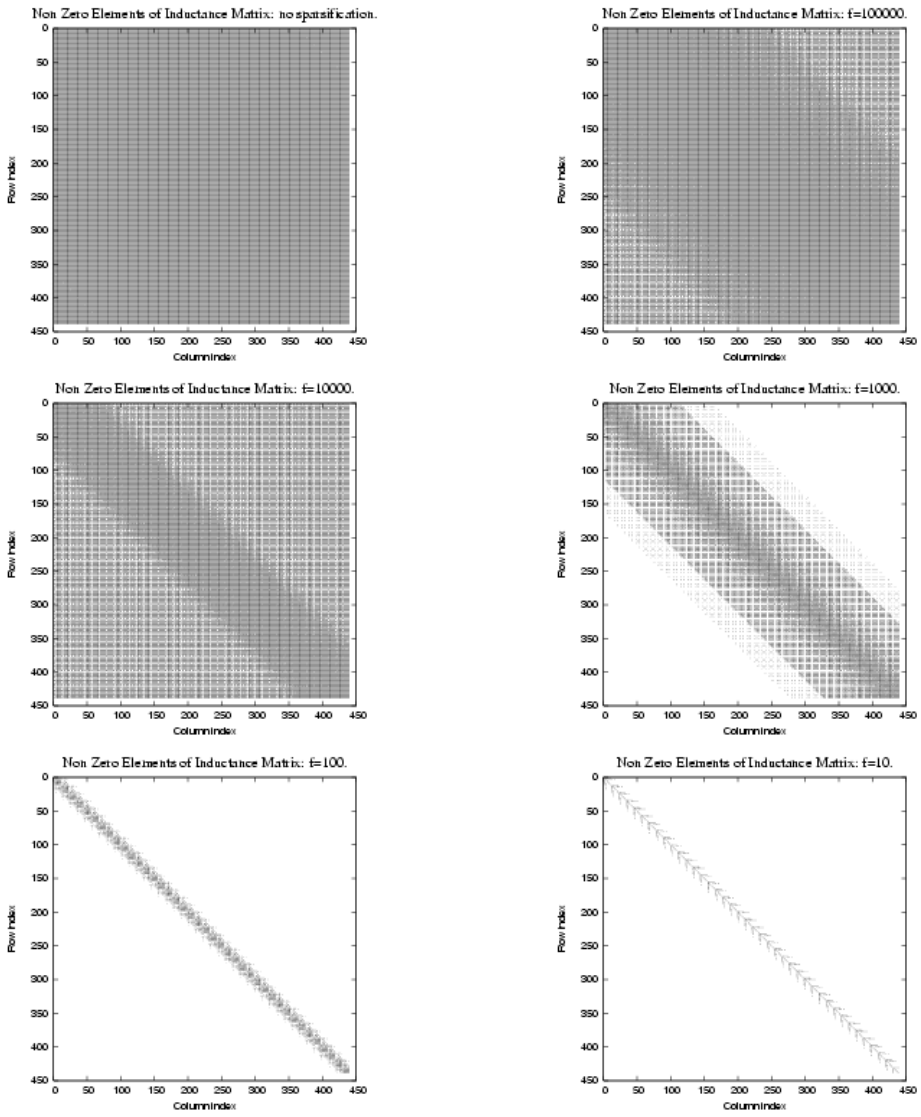

Figure 7.4.7 Sparsification of mesh inductance matrix $\mathcal{L}_M$ for several sparsification factors.

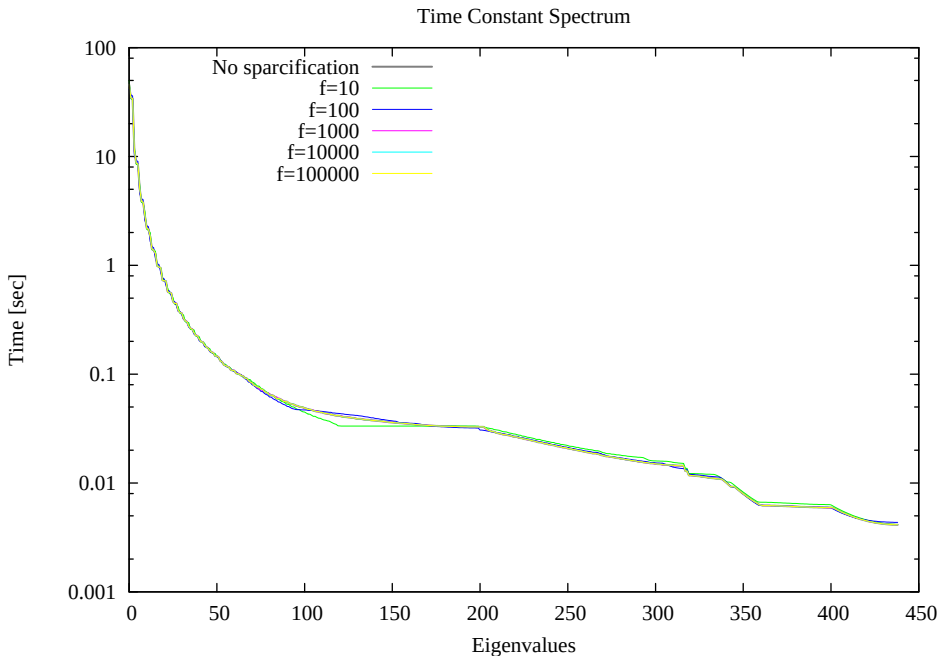

Figure 7.4.8 Time constant spectrum for a 4 strands, 10 twist pitch length cable. Several sparsification factor are used.

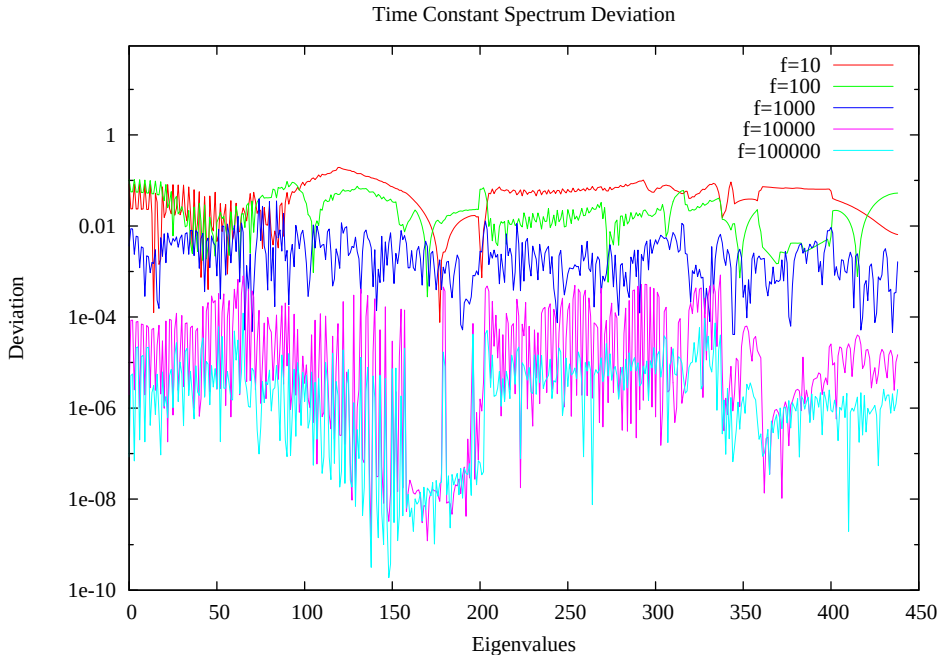

Figure 7.4.9 Time constant spectrum deviation for a 4 strands, 10 twist pitch length cable. Several sparsification factor are used. Modulus of relative deviation in logarithmic scale.

Chapter 8

Numerical Solutions of the Network Model

8.1 Introduction

In this chapter we present and discuss the results of numerical solutions of network model Rutherford-type cable in several condition. As stated in the previous chapter (see figure 7.3.3), we assume that z-axes correspond to the longitudinal direction of the cable, x the width direction and y the height.

8.2 2D Analysis

We can start analysing a single band of a cable with boundary spatial periodic conditions, that is the currents on branches at the cut edge of the cable are the same. For example, in cable in figure 8.2.1, the currents of strands $1-10$, $21-30$, $41-45$ are assumed equal respectively to $50-59$, $70-79$, $90-94$. More over the topology change and also the nodes at the edges are the same. This means that the nodes of the first cross section have 4 branches instead of 3 for a cutted cable.

This situation is representative of the central part of a infinity long cable. It is important to note which are the problems when this kind of condition is implemented in a code. Due to the topology change, there exis meshes with branch of the first and last parts. These branches spatially sapareted are combined in order to calculate the flux linked to the mesh. If the vector potential is 3D then the voltage source of the branches spatially sapareted are affected by a bias and the cannot be used to calculated the flux. What can be done is to perform this operation splitting the sur-

face in the two parts belonging the first and the last section. For example in the figure 8.2.1 the mesh $13 - 71 - 53 - 33$ due to the periodic boundary condition becomes $13 - 22 - 4 - 33$. The flux linked is not the sum $-u_{33} + u_{13} + u_{22} - u_4$, but $-u_{33} + u_{13} + u_a + u_b + _{22} - u_4$ where u_a is the voltage from node 22 to 24 and u_a from 4 to 2. If the vector potential is 2D that is it equal for every z than this problem does not exits because $u_a = u_b$. But in this case only a 2D magnetic field can be studied.

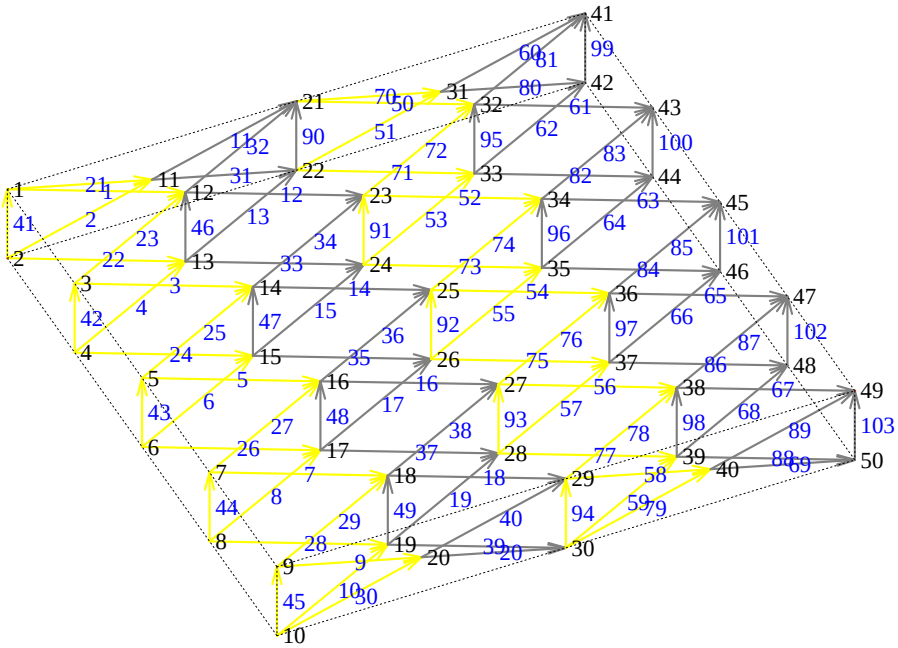

Figure 8.2.1 Network for 2 band of a 10-strands cable. The branch in yellow are the branch assumed equal when spatial periodic boundary condition are applied

We can perform two type of analysis: steady state and transient. In figure 8.2.2 we show a simplified time evolution of magnetic field and eddy currents. When magnetic field start the ramp, voltage sources, due to the change of flux, start to generate currents. This currents cannot start immediately because of the inductive coupling between them. They grow almost exponential until all magnetic energy it is stored. We call this period transient. After transient the value of eddy currents depends only of the contact resistance and the flux linked to the loop. We call this period steady state. When magnetic field end its ramp, voltage source becomes zero, but stored magnetic energy keeps currents flowing for a certain time, until all stored energy it is dissipated. This is another transient period.

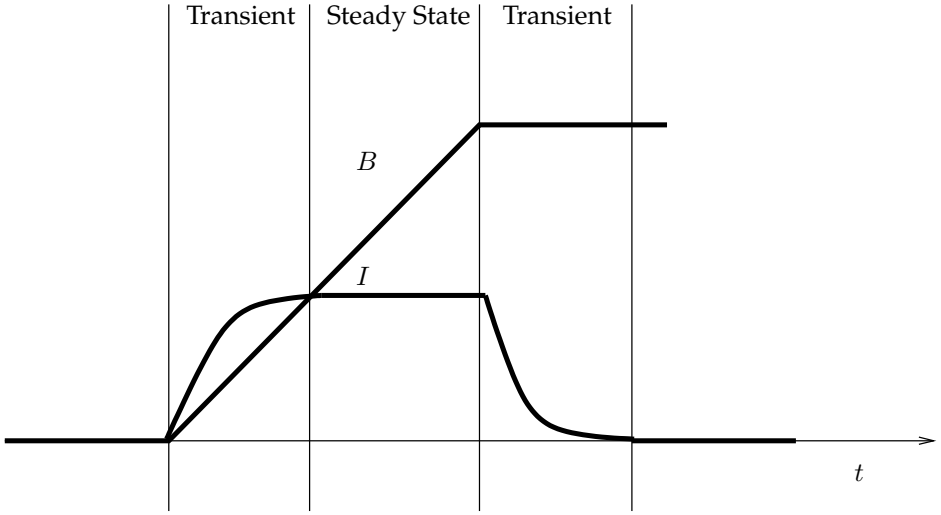

Figure 8.2.2 Definition of steady state and transient periods.

8.2.1 Steady State Calculations

Steady state solutions are calculated neglecting inductive coupling. This represents the situation when steady state solution is reached and the vanished time derivative of eddy currents nullify the contribution of inductances.

We study the effects of a homogeneous linearly ramped magnetic field, which direction is parallel to the height of the cable (y axes).

In order to have rough idea of what happens, we can apply the induction law on the loop showed in the figure 8.2.3.

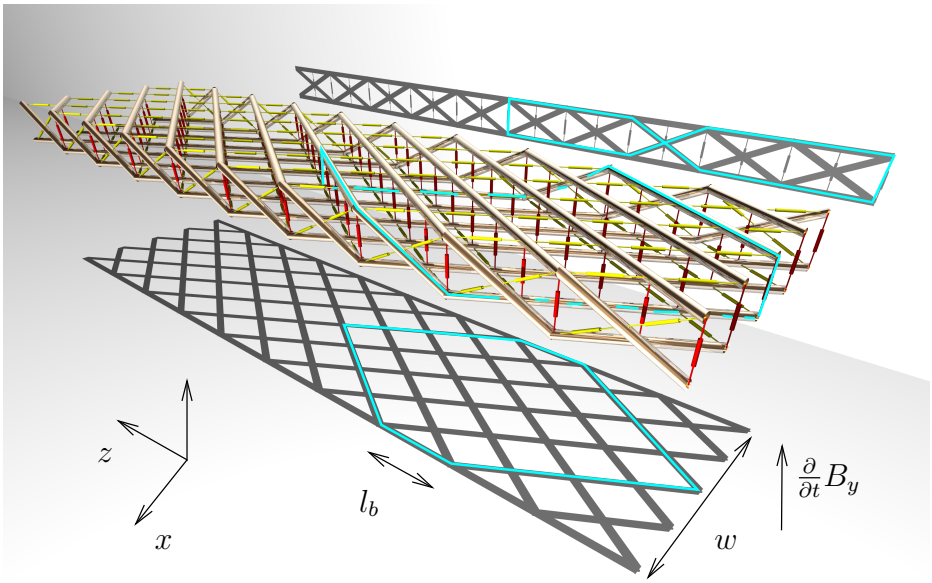

Figure 8.2.3 A loop of current in a 10 strands cable due to a homogeneous $\frac{\partial}{\partial t}B_y$. The dashed cyan line represents the path of the loop.

Area of the loop is $3wl_b$ thus current of the loops is

$$I = \frac{1}{2R_c}\frac{\partial}{\partial t}\Phi = \frac{3wl_b}{2R_c}\frac{\partial}{\partial t}B_y \tag{8.2.1}$$

This gives an idea how eddy currents depends on R_c.

In the picture 8.2.4 we give a qualititative idea of real currents distribution. High currents are located at the edge of the cable and flow on branches representing superconducting strands. Smaller currents flow in the cross resistances, and the smallest in the adjacent strands. We note that there is no electric field in y direction directly due to the $\frac{\partial}{\partial t}\boldsymbol{B}$ because electric field is orthogonal to the magnetic field.

In picture 8.2.5 we give a qualititative idea of the power dissipation. The maximum power is distributed in the centre of the cable where cross resistance have maximum current. This is due to the fact that cross resistance are the resistance that dissipate the current generate by the electric field in the strands. In fact there is no electric field generated directly by magnetic field ($\frac{\partial}{\partial t}A_y = 0$ if $\boldsymbol{B} = B_x\boldsymbol{e}_y$) inside cross resistance.

In figure 8.2.6 the currents in the strands ordered on the x axis are plotted.

In the figure 8.2.7 the currents in the cross resistance ordered on the x axis are plotted.

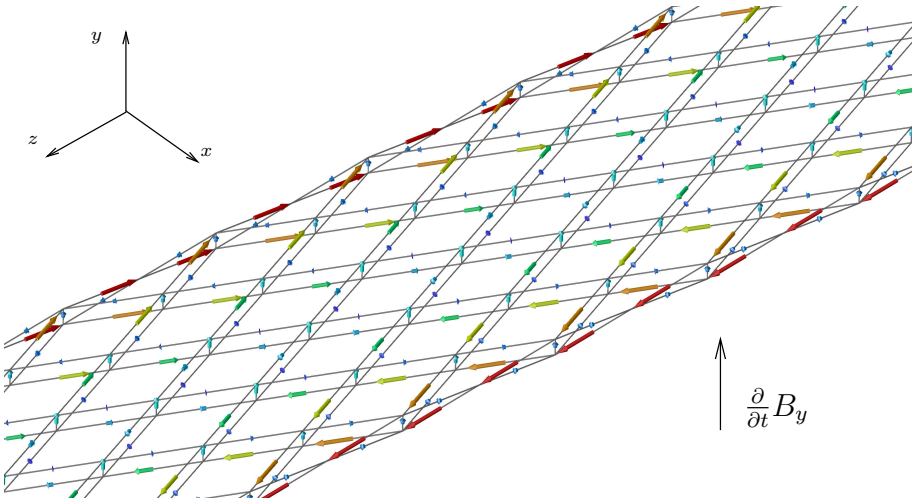

Figure 8.2.4 Current distribution for a 10-strands cable in spatial periodic condition due to a homogeneous linearly ramped magnetic field. Adjacent and cross resistance have the same value.

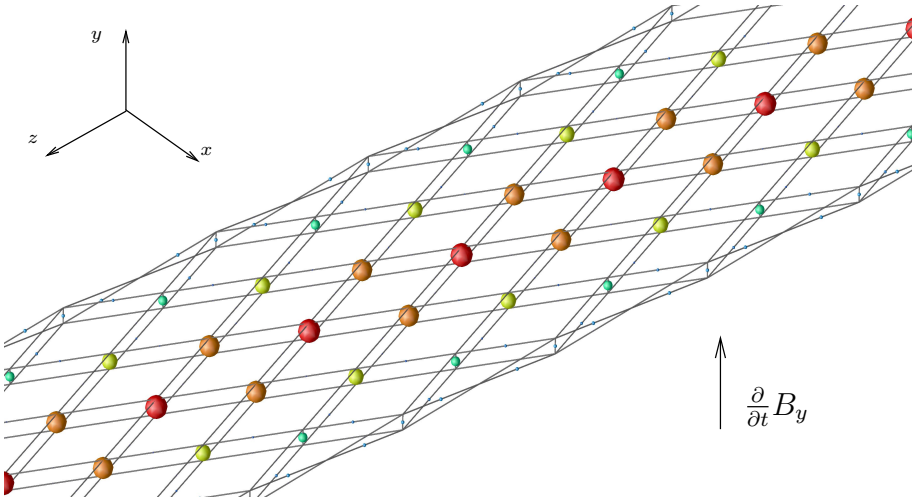

Figure 8.2.5 Power distribution for a 10-strands cable in spatial periodic condition due to a homogeneous linearly ramped magnetic field. Adjacent and cross resistance have the same value.

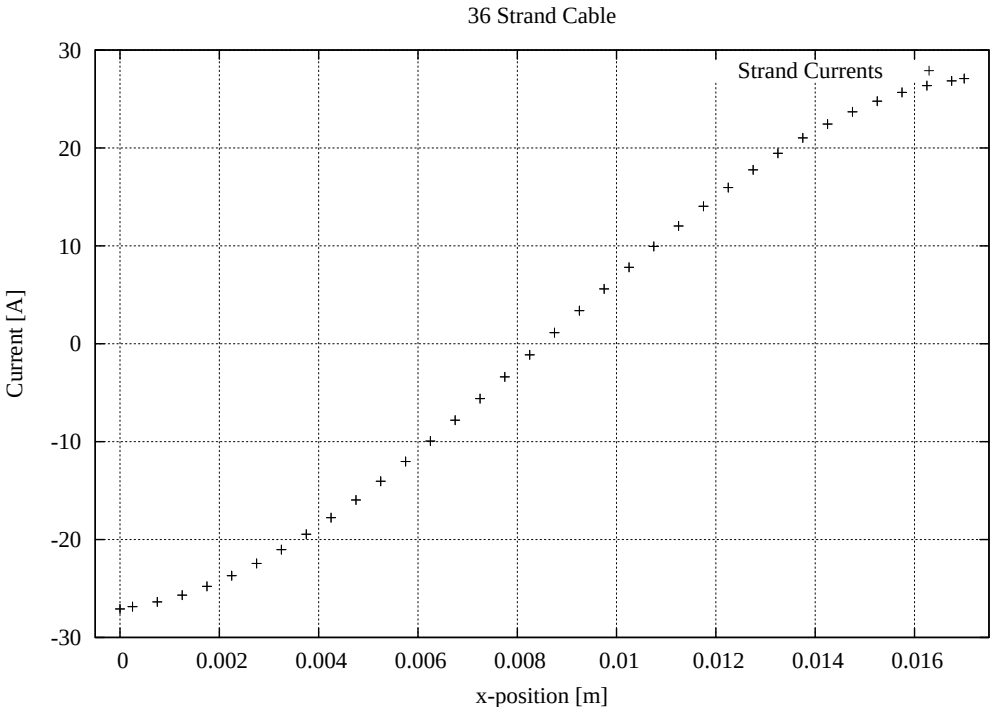

Figure 8.2.6 Current in the strands of a 36-strands cable. $\frac{\partial}{\partial t}B_y = 0.01\,\mathrm{T/\,m}$**, cross resistance** $R_c = 1\mu\,\Omega$**, adjacent resistance** $R_a = 1\mu\,\Omega$**, width** $w = 17\,\mathrm{mm}$**, height** $h = 1\,\mathrm{mm}$**.**

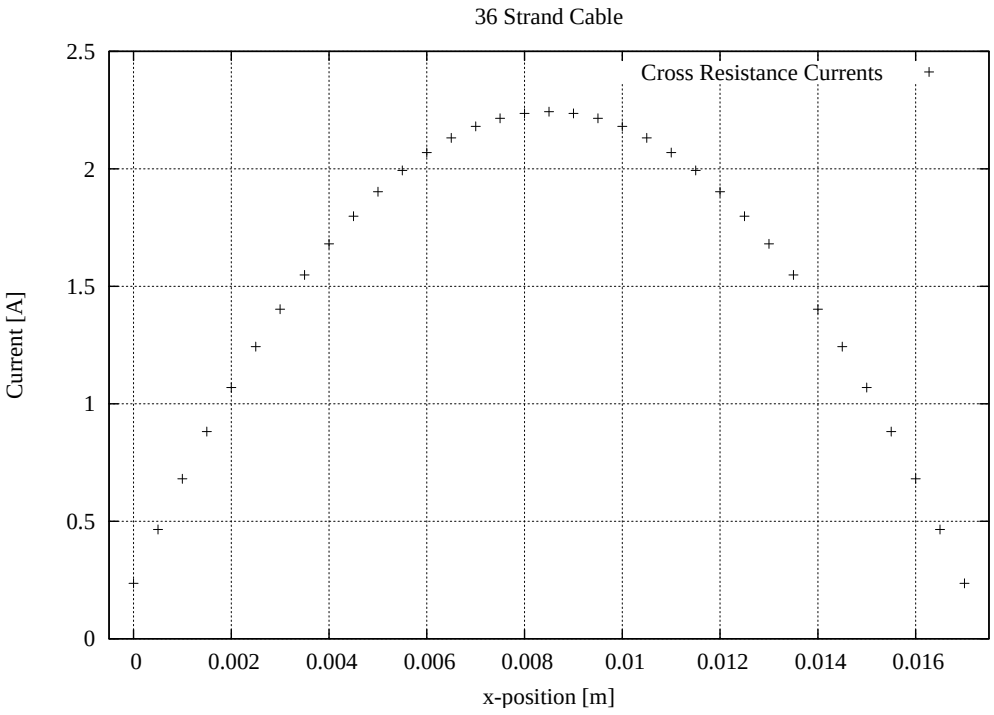

Figure 8.2.7 Current in the cross resistance of a 36-strands cable. $\frac{\partial}{\partial t}B_y = 0.01\,\mathrm{T/m}$**, cross resistance** $R_c = 1\mu\,\Omega$**, adjacent resistance** $R_a = 1\mu\,\Omega$**, width** $w = 17\,\mathrm{mm}$**, height** $h = 1\,\mathrm{mm}$**.**

In the figure 8.2.8 the currents in the adjacent resistance ordered on the x axis are plotted.

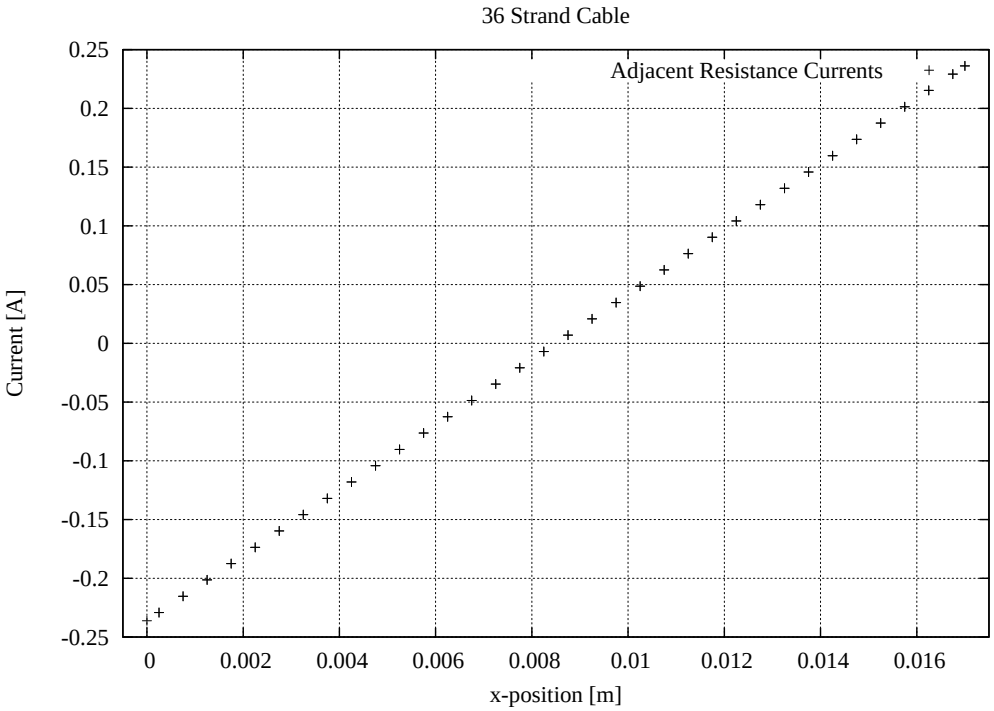

Figure 8.2.8 Current in the adjacent resistances of a 36-strands cable. $\frac{\partial}{\partial t}B_y = 0.01\,\mathrm{T/\,m}$**, cross resistance** $R_c = 1\mu\,\Omega$**, adjacent resistance** $R_a = 1\mu\,\Omega$**, width** $w = 17\,\mathrm{mm}$**, height** $h = 1\,\mathrm{mm}$**.**

Closed solution for eddy currents are found in case that $\boldsymbol{B}$ is homogeneous and R_a are not much bigger than R_c ([VtKL$^+$95], [DO95]) . This solution is compatible with our simulations. The light differences are due to different modelling of the transversal edge of the cable.

8.2.2 Transient Calculations

In the above situation we analyse the transient effects, we use a twist pitch length of the cable applying spatial boundary conditions at the edge.

In the figure 8.2.9, 8.2.10, 8.2.11 are plotted the currents for each type of branch: strand, cross resistance and adjacent resistance. Time is in logarithmic scale. Each line refers to a particular branch identified by his x coordinate. From these pictures we can have an idea of time constants of different currents. Currents in the strands have time constants in the order of seconds as currents in the cross resistance. This shows that currents in cross resistance depends on the currents in the strands and belongs to the same loops. Time constants for adjacent resistance are smaller because loops area is smaller.

These behaviour is compatible with results in the literature ([Ver95]).

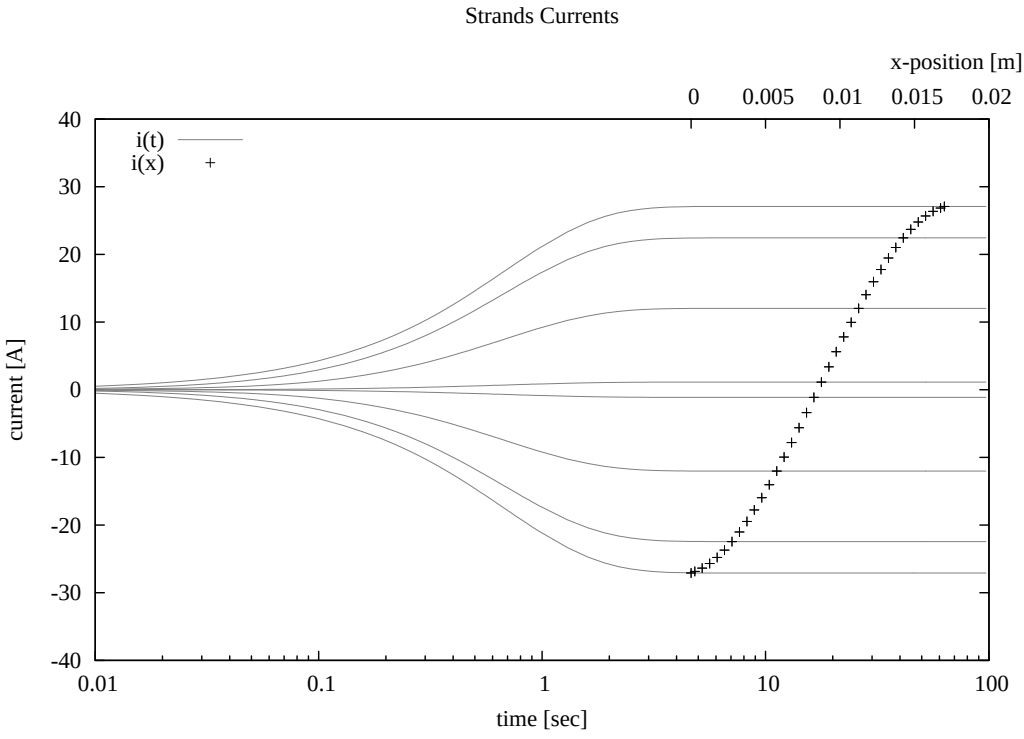

Figure 8.2.9 Current in the strand of a 36-strands cable. $\frac{\partial}{\partial t} B_y = 0.01\,\mathrm{T/m}$**, cross resistance** $R_c = 1\mu\,\Omega$**, adjacent resistance** $R_a = 1\mu\,\Omega$**, width** $w = 17\,\mathrm{mm}$**, height** $h = 1\,\mathrm{mm}$**.**

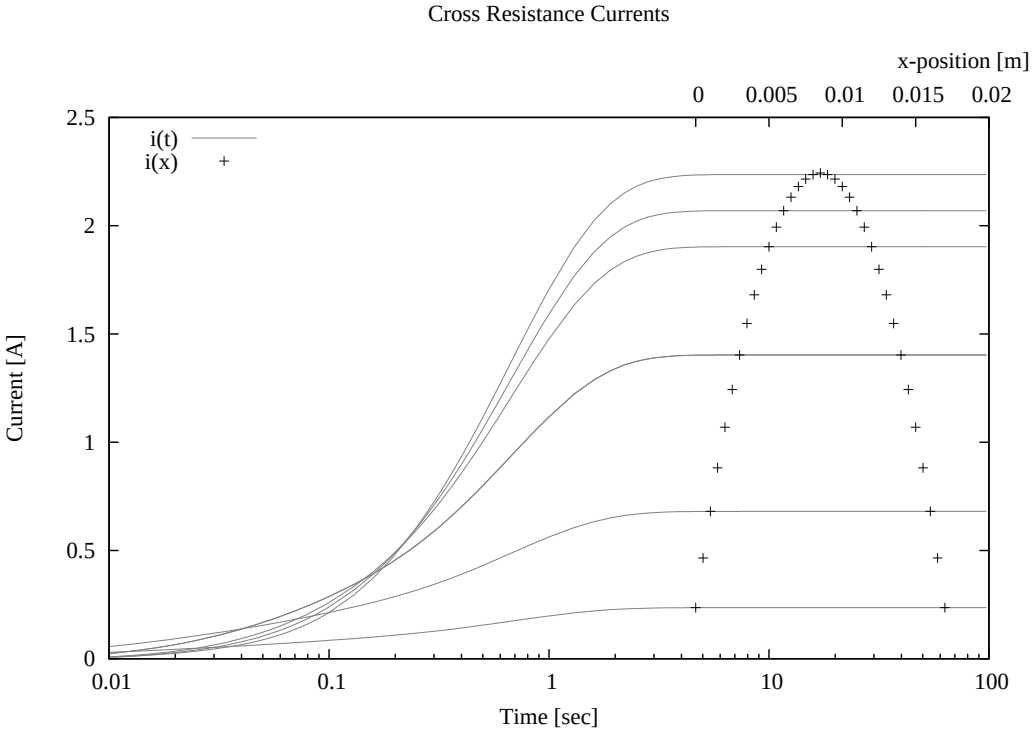

Figure 8.2.10 Current in the cross resistance of a 36-strands cable. $\frac{\partial}{\partial t} B_y = 0.01\,\mathrm{T/m}$**, cross resistance** $R_c = 1\mu\,\Omega$**, adjacent resistance** $R_a = 1\mu\,\Omega$**, width** $w = 17\,\mathrm{mm}$**, height** $h = 1\,\mathrm{mm}$**.**

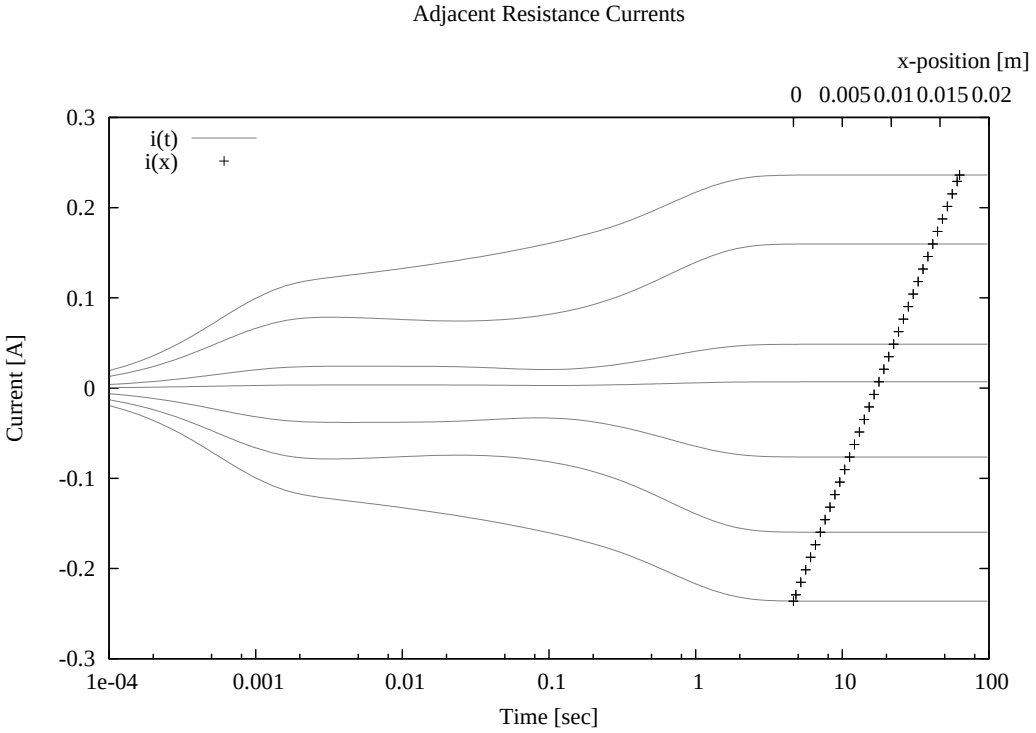

Figure 8.2.11 Current in the adjacent resistance of a 36-strands cable. $\frac{\partial}{\partial t} B_y = 0.01\,\mathrm{T/m}$**, cross resistance** $R_c = 1\mu\,\Omega$**, adjacent resistance** $R_a = 1\mu\,\Omega$**, width** $w = 17\,\mathrm{mm}$**, height** $h = 1\,\mathrm{mm}$**.**

8.3 Numerical Solution for a Magnet

We can apply the 2D analysis in the whole magnet and calculate the effects. Calculations are performed with ROXIE [Rus99] In figure 8.3.12 is show the magnetic field of a dipole, only a quarter is showed. The others quarters ara symmetrics.In the centre magnetic field is a pure dipole field, but in the cable region it assume different magnitude and direction. In particular inner layer cables see a magnetic field orthogonal to their with, while the outer layer cables are subjected to a parallel field.

In figure 8.3.13 the results of eddy current calculation are shown. In the inner layer we find the same distribution calculated using a vertical homogeneous magnetic field. Field generated by eddy currents oppose the existing field. When the magnetic field tends to be parallel to cable width the flux linked is quite smaller and the eddy currents are sensibly smaller.

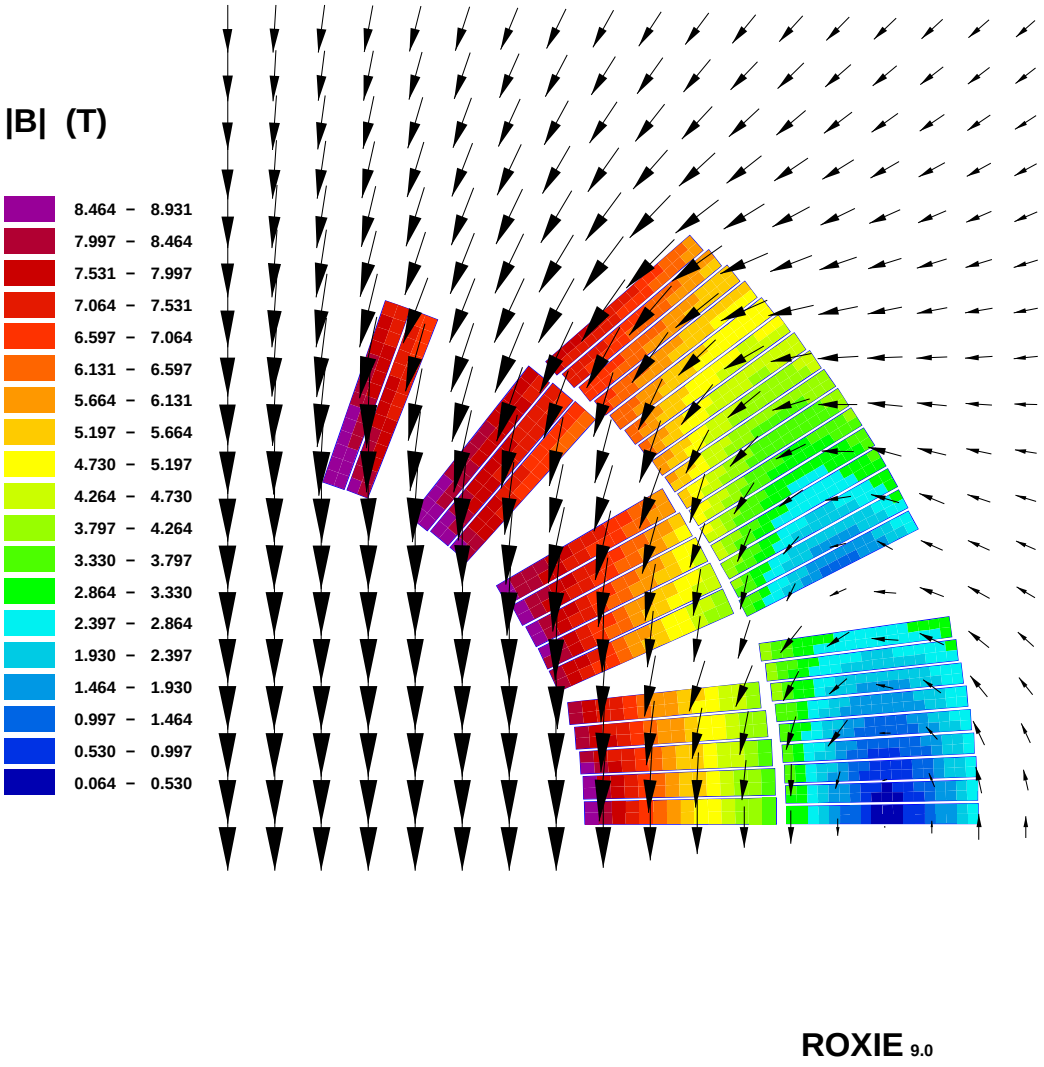

Figure 8.3.12 B of a dipole. In color the $|B|$ inside superconducting cables is shown. Black arrows show the field map.

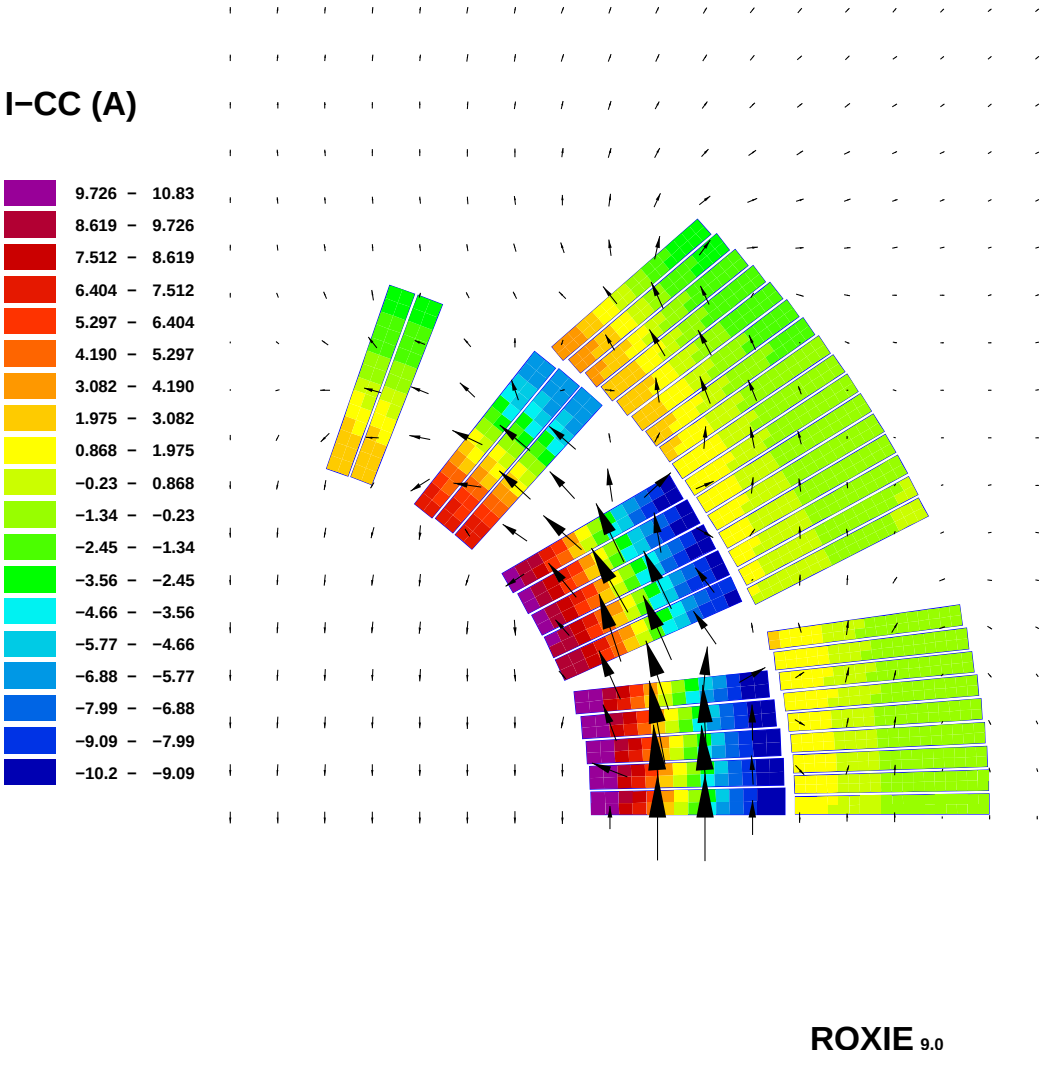

Figure 8.3.13 Inter-strands couplings currents of a dipole. $\frac{\partial}{\partial t}B = 0.094\,\mathrm{T/s}$. In colour the magnitude of currents in the strand that flows orthogonal to the plane. Arrows represent the magnetic field generated by the currents.

8.4 3D Analysis

3D reveals new dynamics in addition to 2D.

In figures 8.4.15 we can follow the time evolution of currents flowing in the strands at one edge of the for every z in several instant in a twist pitch length of 10-strands cable. In these branches flows the maximum current. In the figure 8.4.14 is highlighted the branch whose currents is plotted in figure 8.4.15. No boundary condition are applied thus what it is simulated is the part of the cable showed in figure 8.4.15 in an homogeneous linearly ramped magnetic field in y direction.

In figure 8.4.16 the same time evolution in 3D with time in an axes it shown.

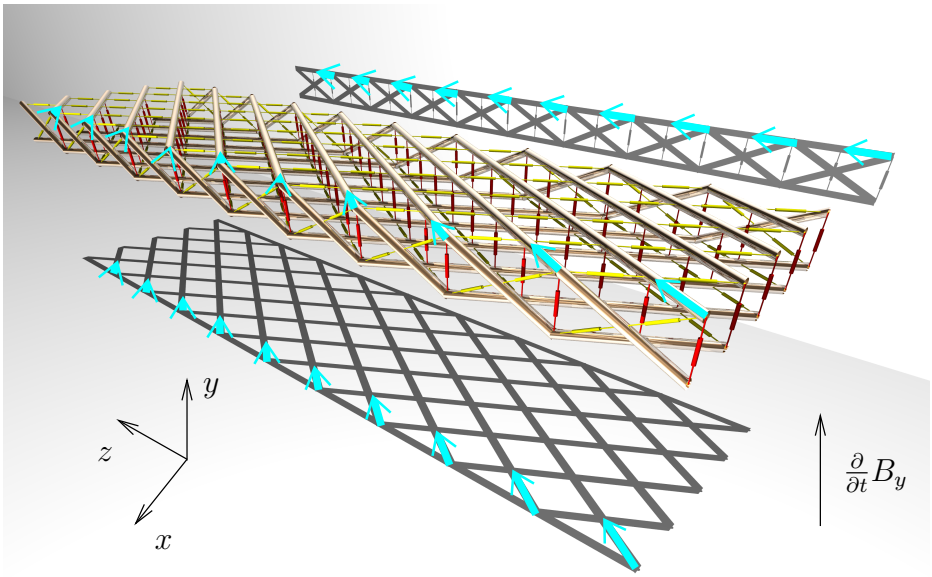

Figure 8.4.14 In cyan strand branches at the edge of the cable for every band.

In figures 8.4.18 we can follow the time evolution of currents in the cross resistance in the position $x = w/2$ for every z in several instant in a twist pitch length of 10-strands cable. In the figure 8.4.17 is highlighted the branch whose currents is plotted in figure 8.4.18. In figure 8.4.19 it shown the same time evolution in 3D with time in an axes.

In the figures 8.4 is show the field map of current density of the first three twist pitch of cable seen from top (y direction). We can see that the oscillation we have seen in the currents are part of a loop cell structure. At the beginning exist only a big loop of currents that closes at the edge.

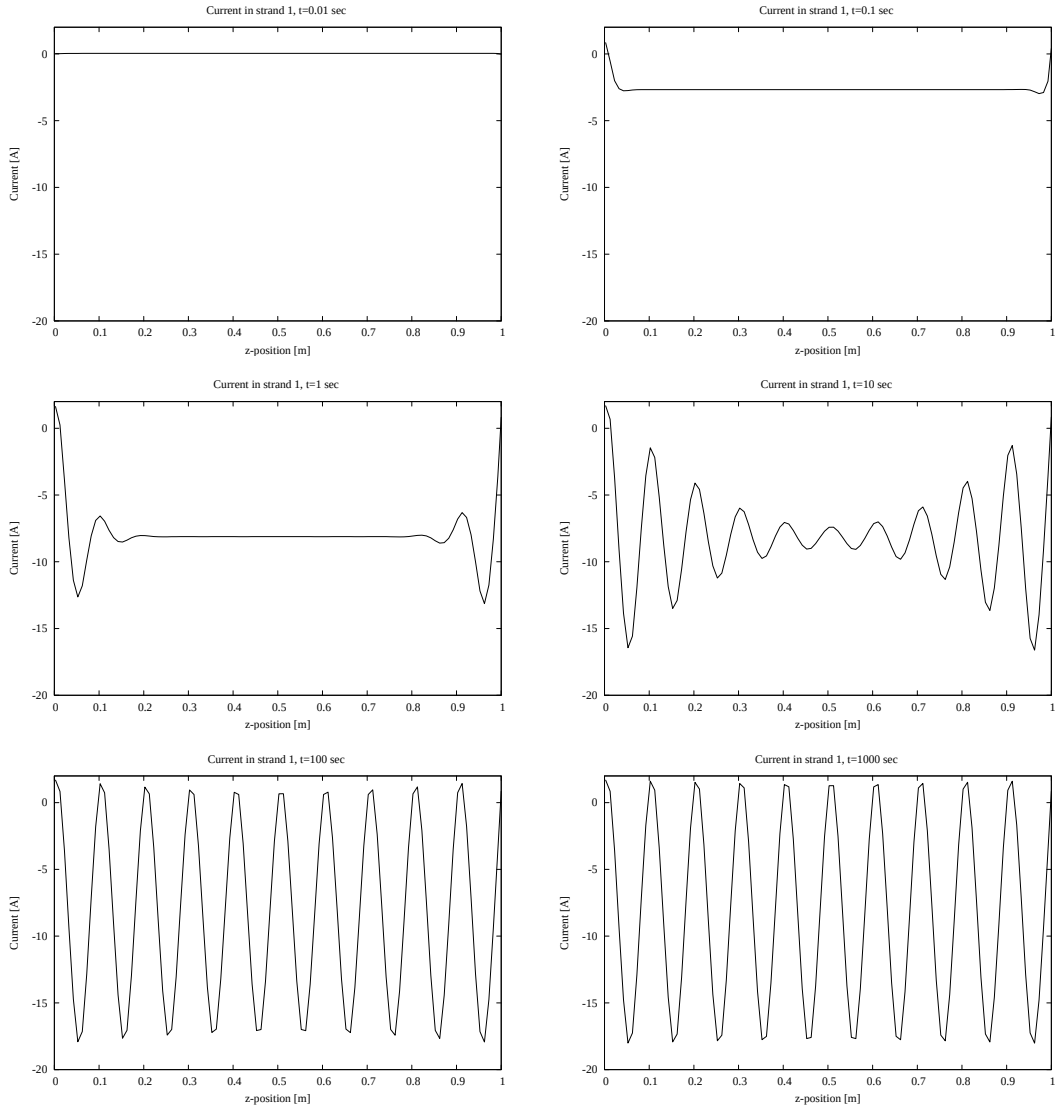

Figure 8.4.15 Time evolution of the current of the strand located at $x = 0$ for each z-position for a 10-strand 10 twist pitch cable without- spatial boundary periodicity condition. $\frac{\partial}{\partial t} B_y = 0.01\,\mathrm{T/m}$, cross resistance $R_c = 1\mu\,\Omega$, adjacent resistance $R_a = 1\mu\,\Omega$, width $w = 17\,\mathrm{mm}$, height $h = 1\,\mathrm{mm}$.

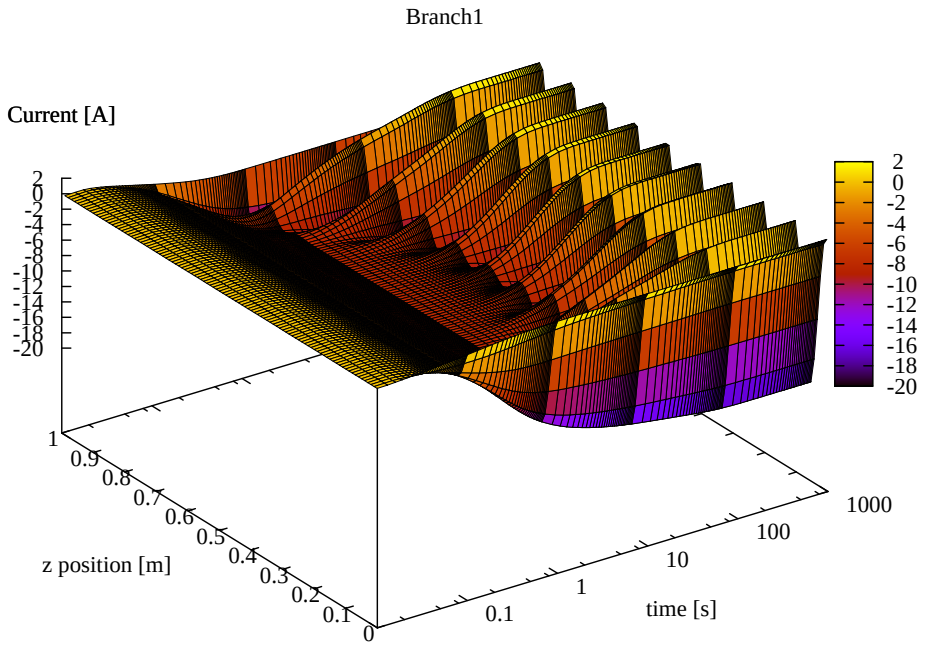

Figure 8.4.16 3D time evolution of the current of the strand located at $x = 0$ for each z-position for a 10-strand 10 twist pitch cable without- spatial boundary periodicity condition. $\frac{\partial}{\partial t} B_y = 0.01\,\mathrm{T/m}$, cross resistance $R_c = 1\mu\,\Omega$, adjacent resistance $R_a = 1\mu\,\Omega$, width $w = 17\,\mathrm{mm}$, height $h = 1\,\mathrm{mm}$.

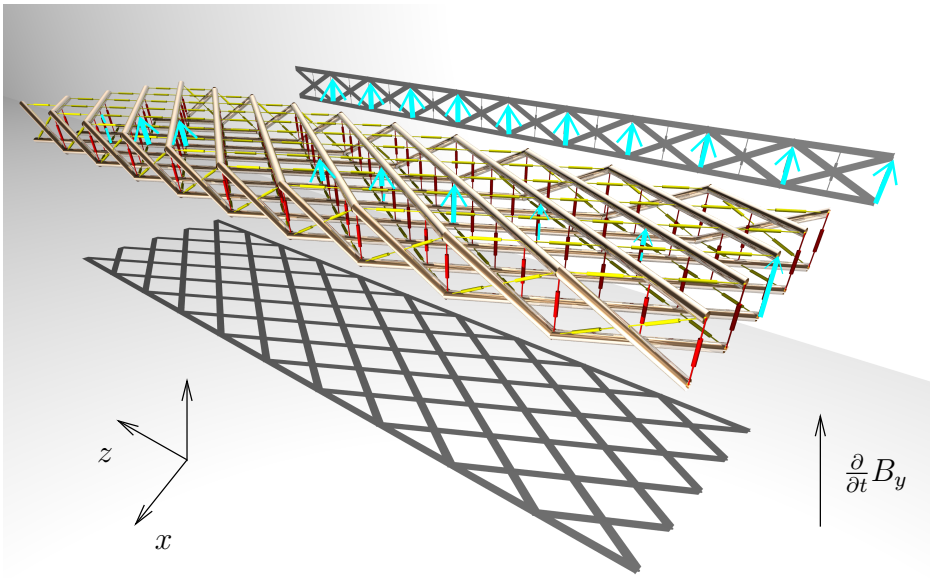

Figure 8.4.17 In cyan branches of cross resistances in the position $x = w/2$ for every band.

With a long time constant this loop tends to split in smaller loopd from the edges to the center of the cable.

In the figure 8.4.21 we can see in detail a single loop.

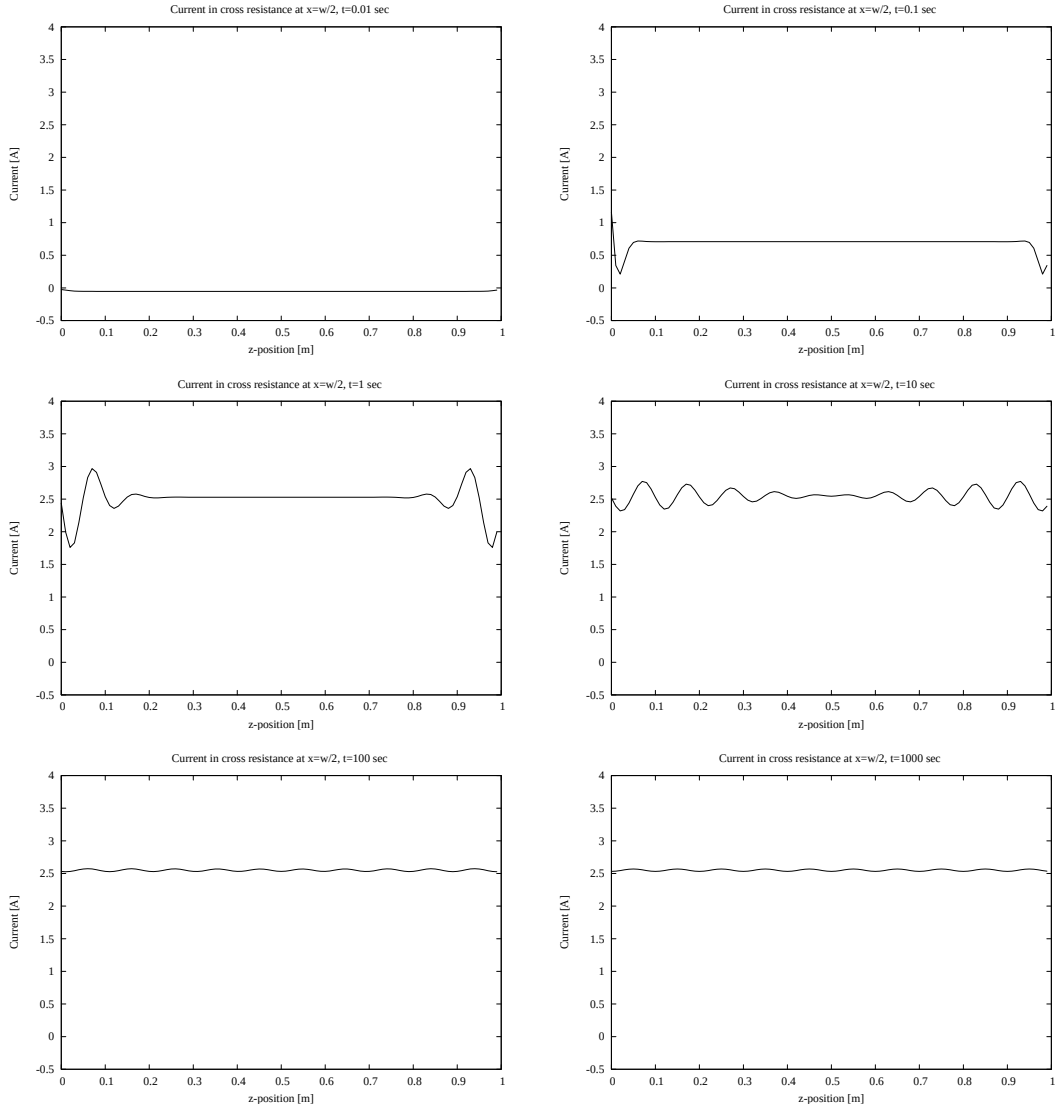

Figure 8.4.18 Time evolution of the current of the cross resistance located at $x = w/2$ for each z-position for a 10-strand 10 twist pitch cable without spatial boundary periodicity condition. $\frac{\partial}{\partial t}B_y = 0.01\,\mathrm{T/m}$, cross resistance $R_c = 1\mu\,\Omega$, adjacent resistance $R_a = 1\mu\,\Omega$, width $w = 17\,\mathrm{mm}$, height $h = 1\,\mathrm{mm}$.

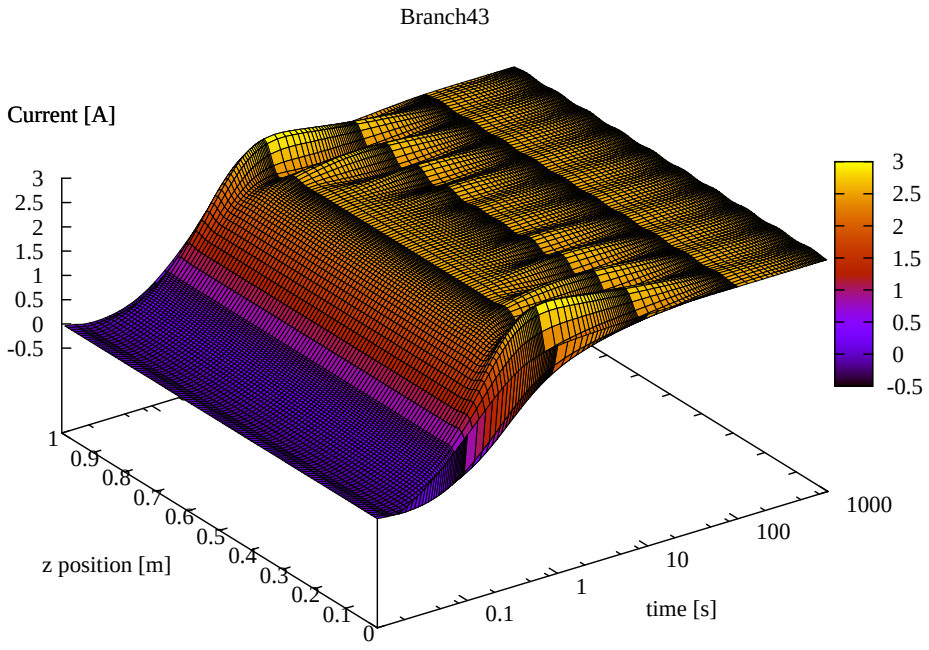

Figure 8.4.19 3D time evolution of the current of the cross resistance located at $x = w/2$ for each z-position for a 10-strand 10 twist pitch cable without spatial boundary periodicity condition. $\frac{\partial}{\partial t} B_y = 0.01\,\mathrm{T/\,m}$, cross resistance $R_c = 1\mu\,\Omega$, adjacent resistance $R_a = 1\mu\,\Omega$, width $w = 17\,\mathrm{mm}$, height $h = 1\,\mathrm{mm}$.

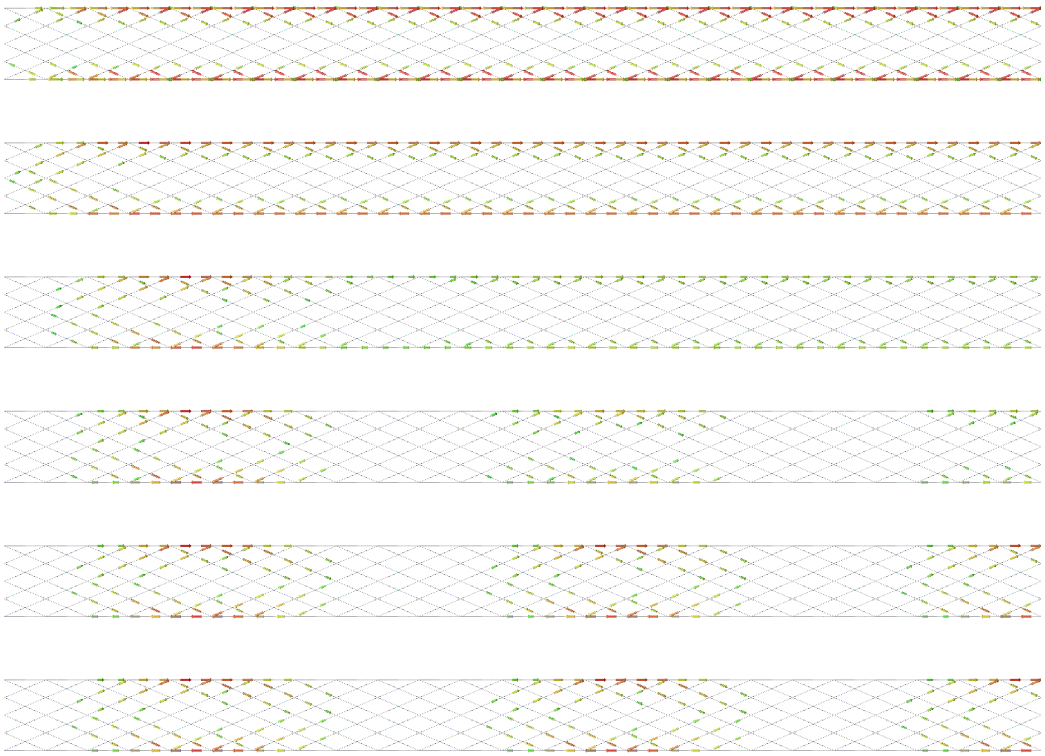

Figure 8.4.20 Comprehensive time evolution of the current of the cross resistance located at $x = w/2$ for each z-position for a 10-strand 10 twist pitch cable without spatial boundary periodicity condition. $\frac{\partial}{\partial t} B_y = 0.01\,\mathrm{T/\,m}$, cross resistance $R_c = 1\mu\,\Omega$, adjacent resistance $R_a = 1\mu\,\Omega$, width $w = 17\,\mathrm{mm}$, height $h = 1\,\mathrm{mm}$. Only the first third of the cable is showed.

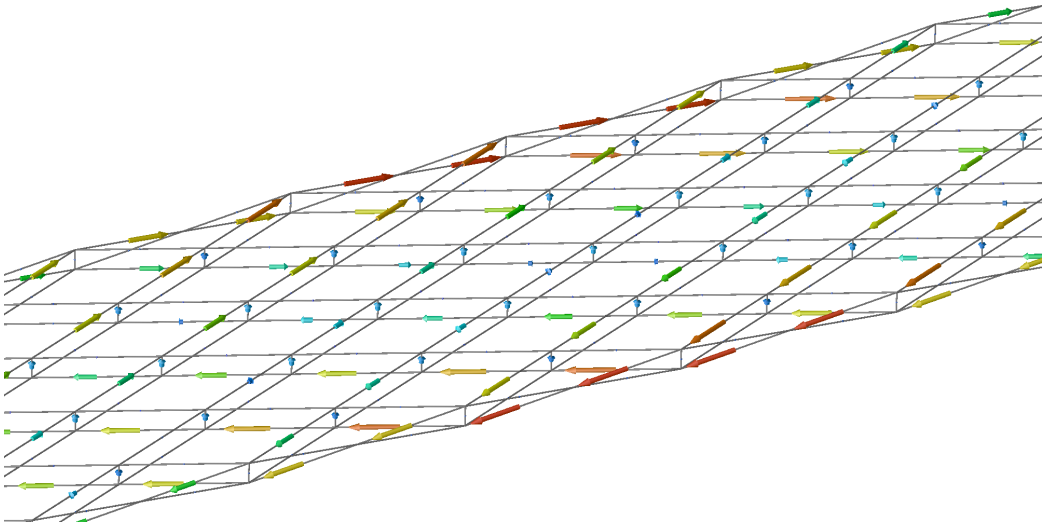

Figure 8.4.21 Detail of current loops and the end of the time evolution in a 10-strand 10 twist pitch cable without spatial boundary periodicity condition.

8.5 Random effects

We can simulate the random effect of a uniform distribution of contact resistance. In figure we show the results for a cable in the same condition as section 8.2.1, but cross resistances and adjacent resistances can vary uniformly of 50% over the mean value. In figures 8.5.22, 8.5.23, 8.5.24 are shown the results where the error bars represent the root mean square deviation.

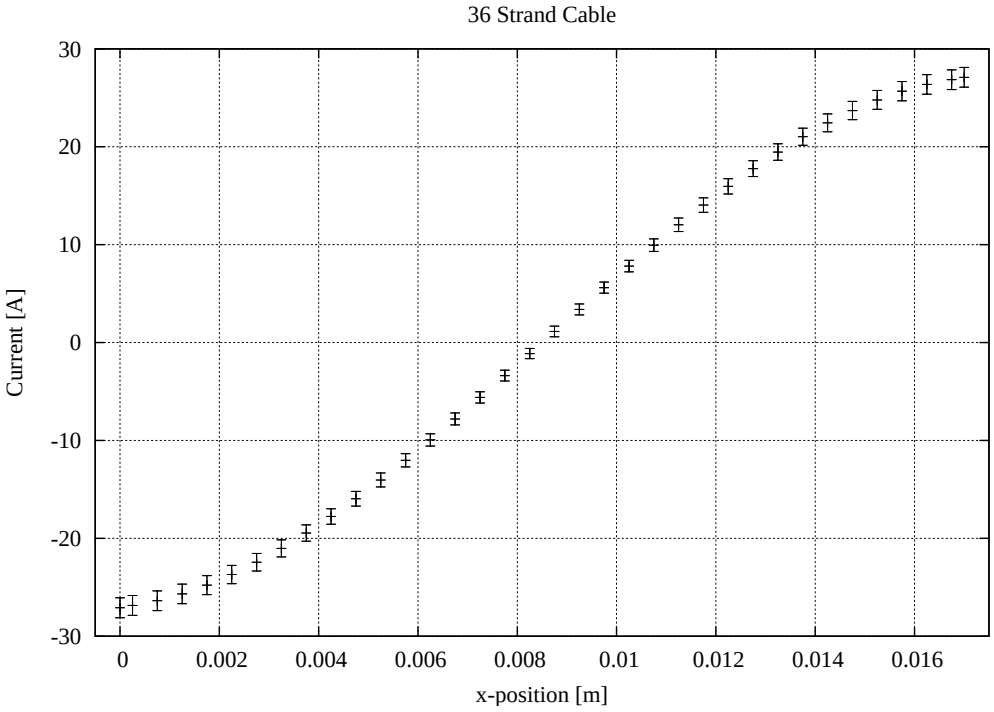

Figure 8.5.22 Current in the strands of a 36-strands cable. $\frac{\partial}{\partial t}B_y = 0.01\,\mathrm{T/m}$**, cross resistance** $R_c = (1 \pm 0.5)\mu\,\Omega$**, adjacent resistance** $R_a = (1 \pm 0.5)\mu\,\Omega$**, width** $w = 17\,\mathrm{mm}$**, height** $h = 1\,\mathrm{mm}$**.**

In the figure 8.5.25 are shown the perceptual deviation of currents ordered on the x axis.

We can see how currents on resistances are equal sensitive to a uniform variation of resistance value. Strand currents on the contrary are less sensitive for high value of current than for lower values.

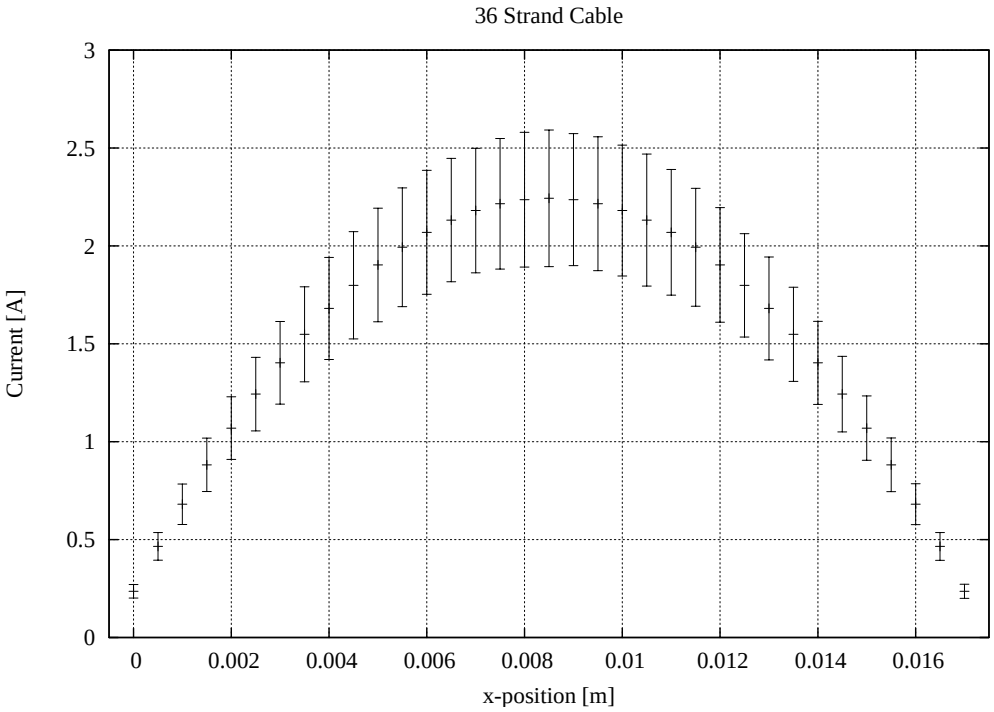

Figure 8.5.23 Current in the cross resistances of a 36-strands cable. $\frac{\partial}{\partial t}B_y = 0.01\,\mathrm{T/\,m}$**, cross resistance** $R_c = (1 \pm 0.5)\mu\,\Omega$**, adjacent resistance** $R_a = (1 \pm 0.5)\mu\,\Omega$**, width** $w = 17\,\mathrm{mm}$**, height** $h = 1\,\mathrm{mm}$**.**

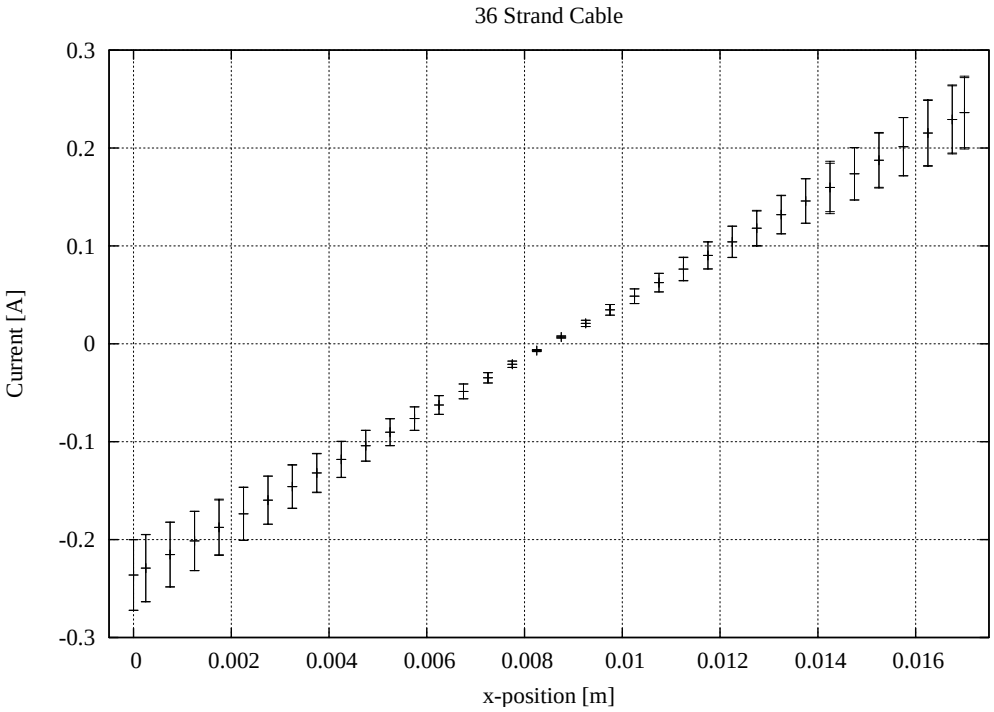

Figure 8.5.24 Current in the adjacent resistances of a 36-strands cable. $\frac{\partial}{\partial t}B_y = 0.01\,\mathrm{T/m}$**, cross resistance** $R_c = (1 \pm 0.5)\mu\,\Omega$**, adjacent resistance** $R_a = (1 \pm 0.5)\mu\,\Omega$**, width** $w = 17\,\mathrm{mm}$**, height** $h = 1\,\mathrm{mm}$**.**

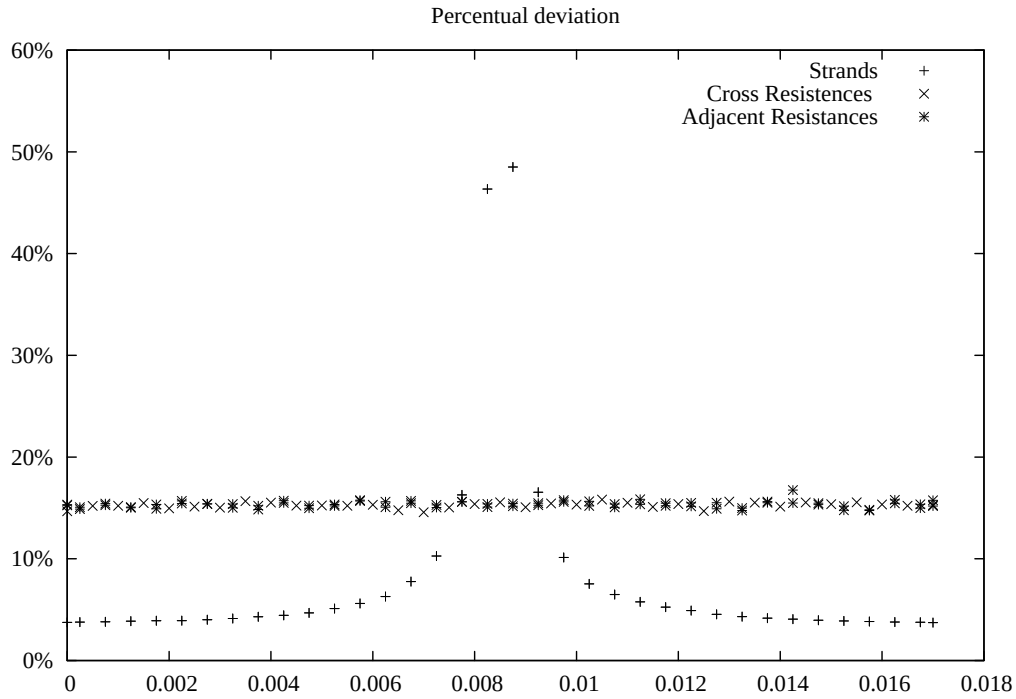

Figure 8.5.25 Perceptual deviation of currents of a 36-strands cable. $\frac{\partial}{\partial t}B_y = 0.01\,\mathrm{T}/\,\mathrm{m}$**, cross resistance** $R_c = (1 \pm 0.5)\mu\,\Omega$**, adjacent resistance** $R_a = (1 \pm 0.5)\mu\,\Omega$**, width** $w = 17\,\mathrm{mm}$**, height** $h = 1\,\mathrm{mm}$**.**

8.6 Spectral Analysis

Is interesting to analyse the resistance mesh matrix $\mathcal{R}_M$. The resistance mesh matrix is responsible of the steady state solutions through formula (6.2.13).

In figure 8.6.26 is shown an example of the spectrum of eigenvalues for a typical cable without spatial boundary periodic condition. Each eigenvector can be interpreted as generalised mesh (see section 6.5), thus the relative eigenvalue represents the resistance of this mesh. In the same figure are plotted the contribution of the different kind of branches for each eigen-current. The contribution as been calculated as follow:

$$\frac{|\mathcal{B}_S\mathcal{Q}_\lambda|}{|\mathcal{Q}_\lambda|}, \frac{|\mathcal{B}_C\mathcal{Q}_\lambda|}{|\mathcal{Q}_\lambda|}, \frac{|\mathcal{B}_A\mathcal{Q}_\lambda|}{|\mathcal{Q}_\lambda|}, \tag{8.6.1}$$

where $\mathcal{B}_S$, $\mathcal{B}_C$, $\mathcal{B}_A$ are row vectors whose elements are 1 if the element column index is the branch index of respectively a strand, a cross resistance or an adjacent resistance.

We can see that the smallest eigenvalues are relative to the eigenvector mainly constituted by strand branches that have no resistance.

In figure 8.6.27 we can see the sources due to an homogeneous magnetic field. We can see that only few eigen-currents are excited. The most exited eigen-currents has the lowest eigenvalue. In the figures 8.6.28 and 8.6.29 are shown the density current vector field relative to this mode. As we have seen in the 3D analysis this is in fact the distribution of the currents inside a isolated cable.

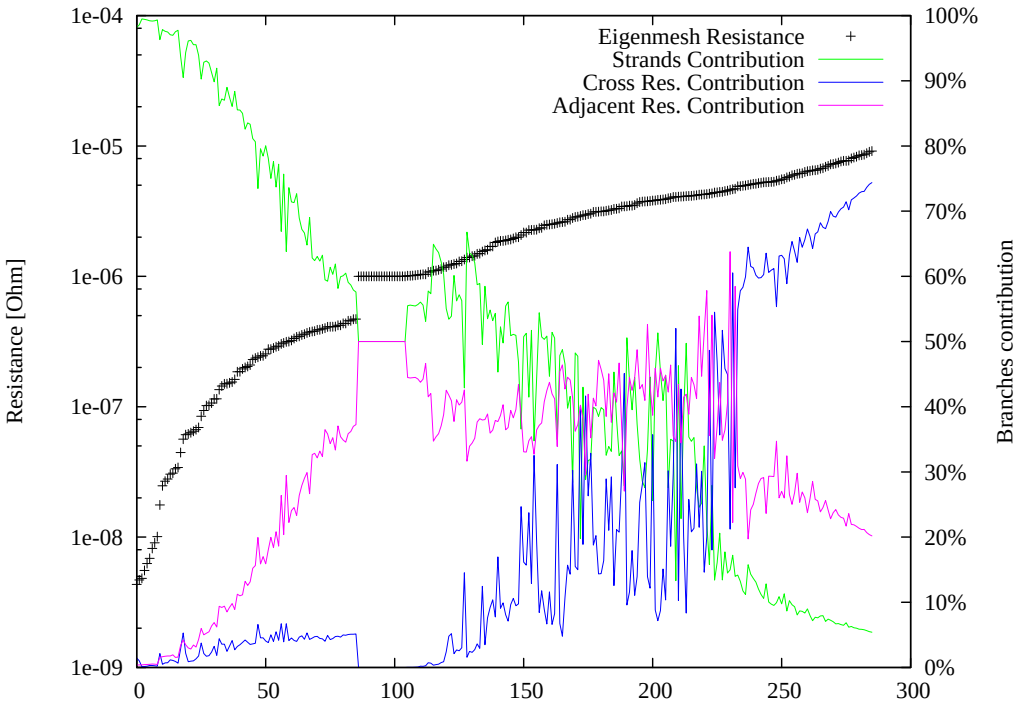

Figure 8.6.26 Eigenvalues of the resistance mesh matrix $\mathcal{R}_M$ of a 10-strand 10 twist pitch cable without spatial boundary periodicity condition in logarithmic scale.

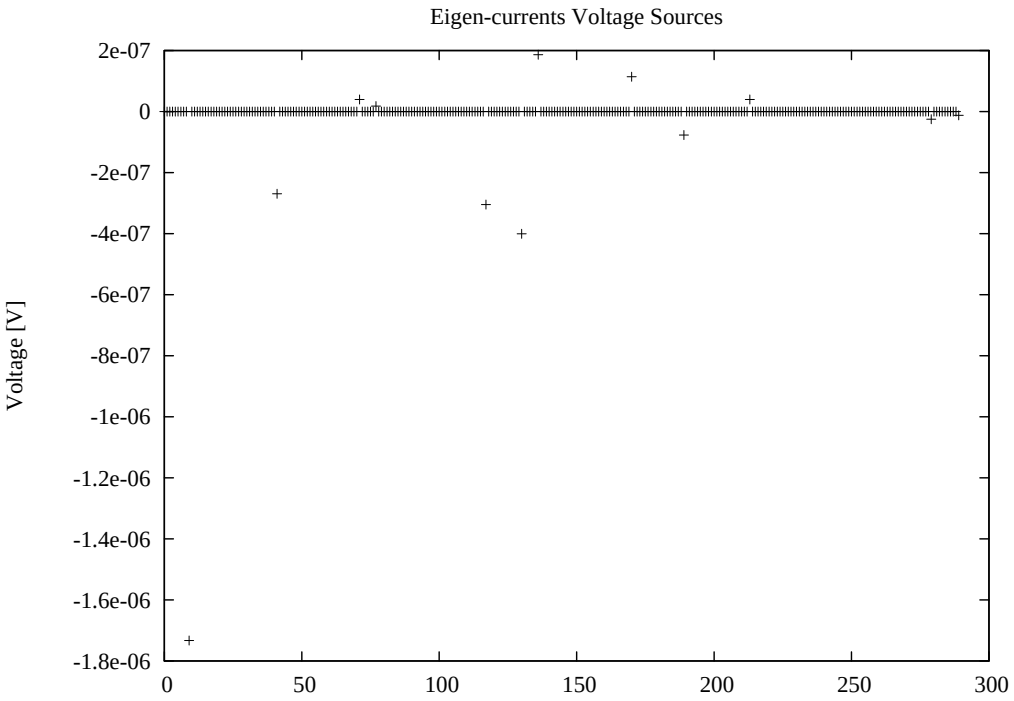

Figure 8.6.27 Voltage sources $\mathcal{U}_D$ relative to the eigen-currents of a 10-strand 10 twist pitch cable without spatial boundary periodicity condition.

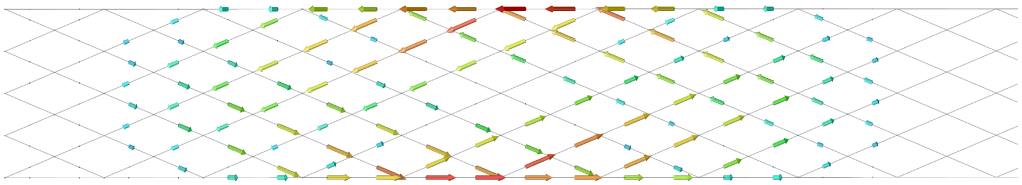

Figure 8.6.28 Eigen-currents relative to the first eigenvalues of the resistance mesh matrix $\mathcal{R}_M$ of a 10-strand 10 twist pitch cable without spatial boundary periodicity condition.

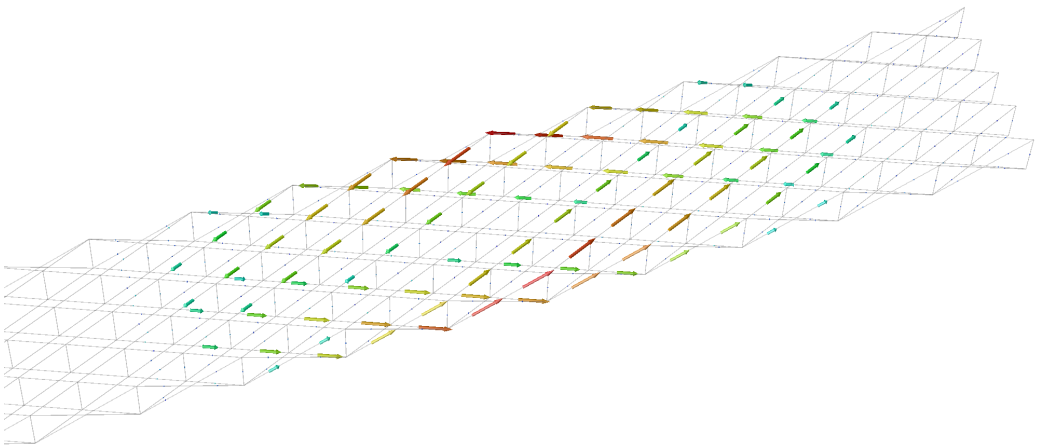

Figure 8.6.29 3D view of eigen-currents relative to the first eigenvalues of the resistance mesh matrix $\mathcal{R}_M$ of a 10-strand 10 twist pitch cable without spatial boundary periodicity condition.

The spectral analysis get more interesting when periodic boundary conditions are applied. If we choose a number of bands multiple of the number of strands (an integer number of twist pitch lengths) resistance mesh matrix becomes singular. The dimension of null space is $N_s - 1$. It means that there are a subspace of solutions. With spectral analysis we can analysis what kind of solution are.

In the figure 8.6.27 are shown the eigenvalues of the resistance mesh matrix $\mathcal{M}_D$ in the same case seen before but with periodic boundary condition. In the same figure we can see the contributions of each type of branch in the eigen-vector. We can see that there are 9 very low eigenvalues, less than machine precision, that can be treated as 0. It means that there are 9 eigen-currents that see no resistances, in fact they flow only superconducting strands as shown in figure 8.6.27. Thus we have 9 modes that can be exited without limitations.

In the figure 8.6.32 and 8.6.33 we can see one of these eigencurrents. This kind of modes are currents belonging to few strands that flow in different direction and they closes to the infinity.

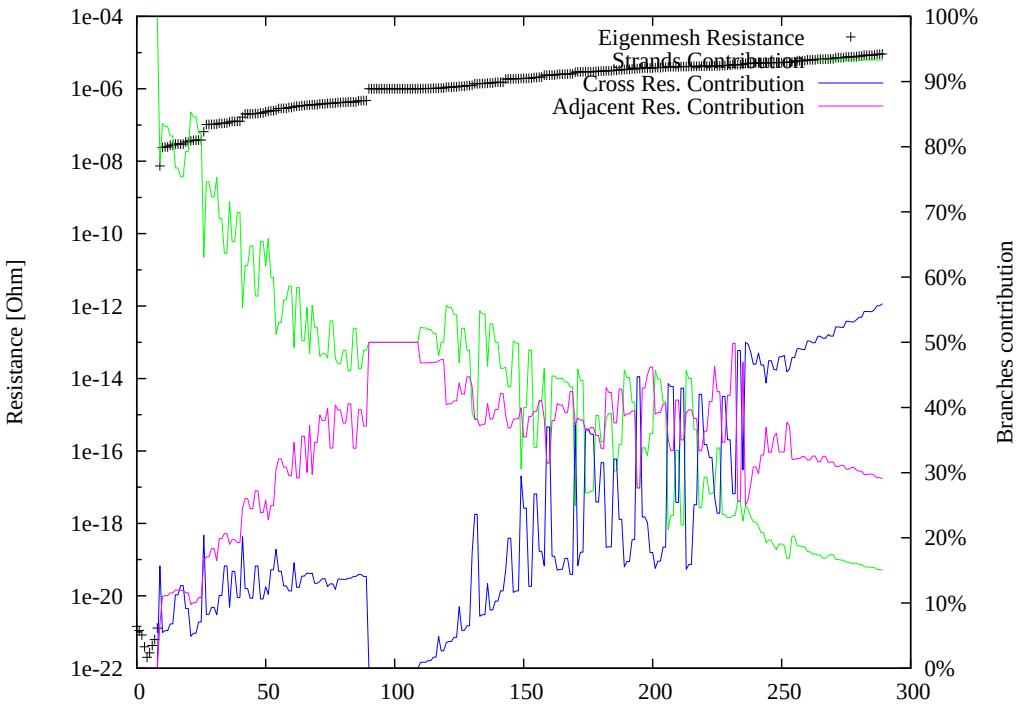

Figure 8.6.30 Eigenvalues of the resistance mesh matrix $\mathcal{R}_M$ of a 10-strand 10 twist pitch cable with spatial boundary periodicity condition in logarithmic scale.

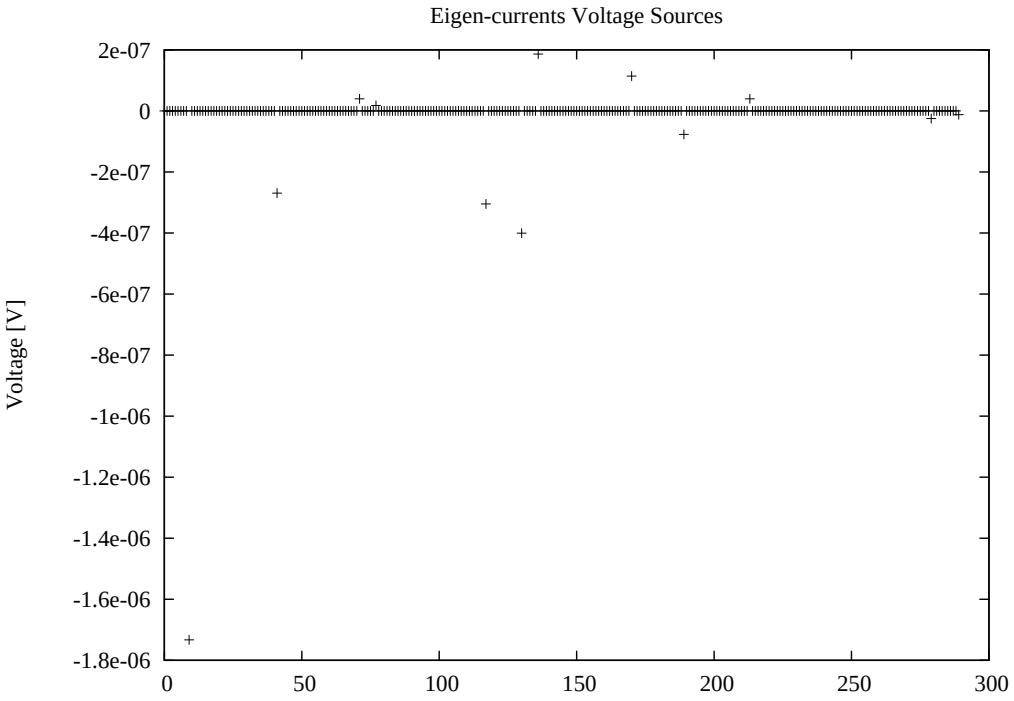

Figure 8.6.31 Voltage sources $\mathcal{U}_D$ relative to the eigen-currents of a 10-strand 10 twist pitch cable with spatial boundary periodicity condition.

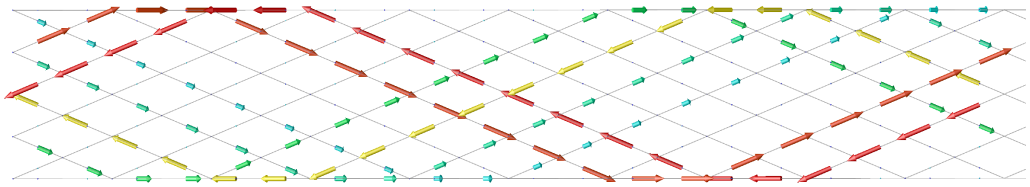

Figure 8.6.32 Eigen-currents relative to the first eigenvalues of the resistance mesh matrix $\mathcal{R}_M$ of a 10-strand 10 twist pitch cable with spatial boundary periodicity condition.

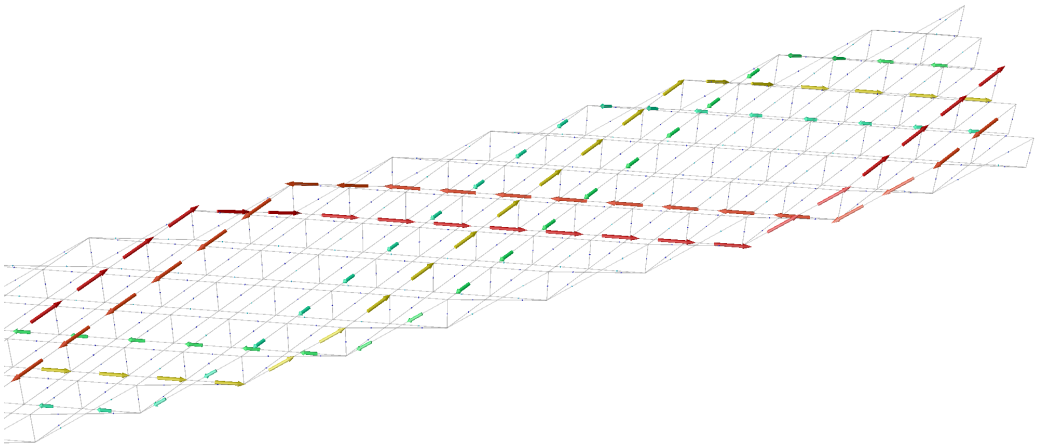

Figure 8.6.33 3D view of eigen-currents relative to the first eigenvalues of the resistance mesh matrix $\mathcal{R}_M$ of a 10-strand 10 twist pitch cable with spatial boundary periodicity condition.

Chapter 9

Implementation of the Network Model

9.1 Sparse Matrices

In order to reduce memory consumption and calculation time, all the matrix are stored in special forms.

Incidence matrix it is not calculated directly, instead it is used a net-list matrix. It is a $B \times 3$ matrix, where B is the number of branches. Row index is the branch number. In the first column is stored the type of branch as an integer value: 1 for strands, 2 for adjacent resistances, 3 for cross resistances. In the second and third column are stored the first a the second node number.

Mesh matrix it is stored in a special format. It is a $M \times 4$ matrix where M is the number of independent mesh. Row index is the mesh number. In each column is stored the branch number that belongs to the mesh. If the branch has the opposite direction with respect to the mesh current, its number is negative. The number 4 is used because the number of strands that belong to mesh it is not greater the 4. In particular the algorithm that find meshed is implemented in order to obtain mesh with 3 or 4 strands. For mesh with 3 strands the last column is filled with 0.

System matrices are stored in the so-called Compressed Sparse Columns (SCS) scheme [Saa96]. In this format only non zero elements are stored. In particular they are stored in a vector. Two other integer vectors store the information of the index of non zero elements.

Matrix multiplication of the type $\mathcal{M}\mathcal{R}\mathcal{M}^T$ is calculated using a special algorithm that use as input and output the matrix in the special form seen above.

Resistance matrix and inductance matrix are not stored at all, a function is used instead. In fact they are used only once when the system matrices $\mathcal{Z}_A$ and $\mathcal{Z}_B$ are calculated for the first time. When they change due to a time step variation, the previous values that matrices are used to calculate new values. In fact from definition (6.4.7)

$$\begin{aligned} \mathcal{Z}_A &= \mathcal{R}_M + \frac{2}{h}\mathcal{L}_M \\ \mathcal{Z}_B &= \mathcal{R}_M - \frac{2}{h}\mathcal{L}_M \end{aligned} \quad \Rightarrow \quad \begin{aligned} \mathcal{R}_M &= \frac{\mathcal{Z}_A + \mathcal{Z}_B}{2} \\ \mathcal{L}_M &= h\frac{\mathcal{Z}_A - \mathcal{Z}_B}{4} \end{aligned} \tag{9.1.1}$$

9.2 Linear system solution

In order to solve the linear system for steady state analysis (6.2.13)

$$\mathcal{R}_M \mathcal{I}_M(k) = -\mathcal{U}_M(k) \tag{9.2.1}$$

or for transient analysis (6.4.6)

$$\mathcal{Z}_A \mathcal{I}_M(k+1) = -\Big(\mathcal{Z}_B \mathcal{I}_M(k) + \mathcal{U}_M(k) + \mathcal{U}_M(k+1)\Big), \tag{9.2.2}$$

is used LU decomposition method [PTVF01].

For a system $Ax = b$ is found a decomposition for A as a multiplication of a lower triangle and upper triangle matrix $A = LU$. Then performed a forward substitution to solve the system $Ly = b$ then a back substitution to solve system $Ux = y$.

Decomposition and back substitution is performed by the open source solver SuperLU [XD98] optimised for sparse matrices in order to take the advantages due the sparsification.

Decomposition is performed only when necessary (a change in the system matrix) and the results is used for substitution every time step. In this way a great speed is reached.

9.3 Main algorithm

A block diagram of the main algorithm is sketched in the figure 9.3.1

Main routine use as input parameter time, magnetic field, cables information and return calculated currents. Routine use some static variable that are kept from a call to the other in order to store information on the calling history and the previous time steps.

In order to illustrate the algorithm we can ideally compute the firsts time step.

Step 1

It is a dummy step because no derivative can be calculated. The first conditional block recognise that it the first call. All variable are initialised. Size of arrays are calculated using cable informations from the main program. From the same information a list of the branches, meshes and position of the node are generated. Using magnetic field information the vector potential is calculated for each node. Because no calculation can be performed, time and vector potential are stored as old values.

Step 2

In the second time step, the time step size can be calculated. Another conditional block intercepts the second call. Now system matrices $\mathcal{Z}_A$ and $\mathcal{Z}_B$ or $\mathcal{R}_M$ can be calculated and decomposed. The actual vector potential is calculated and using the previous time step one the derivative can be obtained. With the derivative of vector potential is used for calculating voltage source matrix $\mathcal{U}_M$. Now all variables are ready for solving the system and obtain currents. At the end the actual values are stored as old values.

Step 3

If the time step size not changed, only new vector potential has to be calculated to obtain current for the actual time step. But if the time step has changed the system matrices $\mathcal{Z}_A$ and $\mathcal{Z}_B$ have to be updated in order to reflect the change of the inductive part.

9.4 Performance

Memory consumption depends on the size of matrices that have to be stored. The greatest matrices are the system matrices $\mathcal{Z}_A$ and $\mathcal{Z}_B$ that in principal have $M^2 \approx 9(N_s^2 L/Lp)^2$ elements, where M is the number of independent meshes, N_s the number of strands, L is the length and L_p is the twist pitch. For example for a 36 strands LHC cable $10\,\mathrm{m}$ long number of elements are in the order of $10^1 1$. Using sparcification technique number of nonzero elements are in the order of $20N_s^2 L/Lp$ for steady state analysis and $500N_s^2 L/Lp$ for transient analysis in practical cases.

Calculation time depends mainly on the calculation of system matrix in which inductance calculation and triple matrix product it is performed.

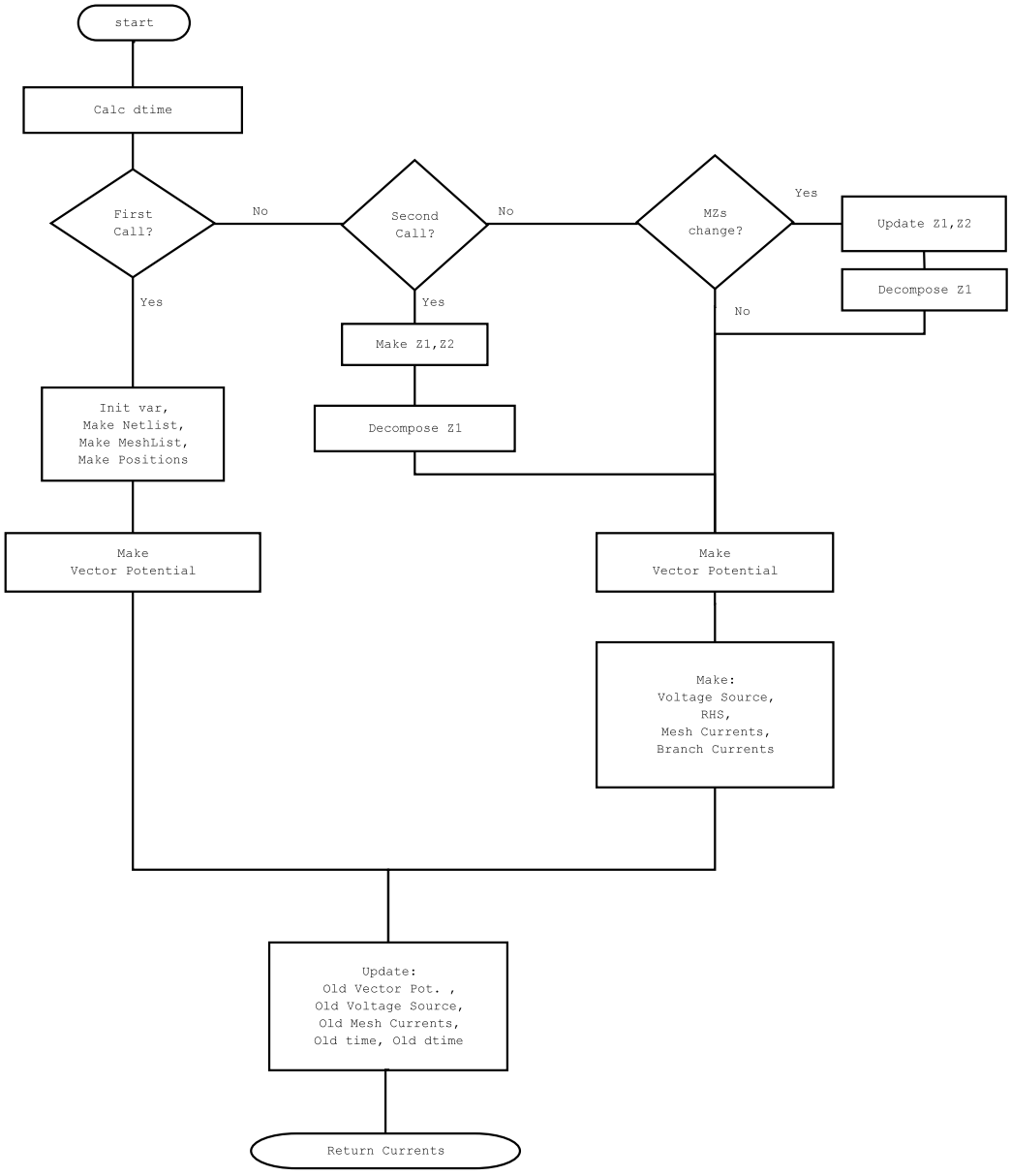

Figure 9.3.1 Main Algorithm

The product routine uses all non zero elements of mesh matrix and resistance matrix, but use all virtual (matrix it is not stored but it is a function) elements of inductances matrix thus depends on $(N_s^2 L/Lp)^2$. In fact sparcification process has made after the calculation of the product elements. In principle zero elements position can be estimated in order to avoid their calculation, but this estimation cannot cover all the cases that the code can manage and it makes code less general. We note that this calculation is performed only one time during calculation process, this choice can be a good compromise.

In order to give an idea calculation time for 150 (5 decades) time steps of a 10 strands 10 twist pitch length cable is 1 minute and use 20 MB on a 1.2GHz single CPU.

9.5 Hypothesis for iteration with persistent currents and iron joke saturation

The ROXIE program [Rus99] has the capability to calculate the non-linear and history dependent effects of persistent current and iron yoke saturation. The effects are calculated separately and then an iteration is performed.

The calculation of coupling currents could be added in this scheme using the scheme in figure 9.5.2.

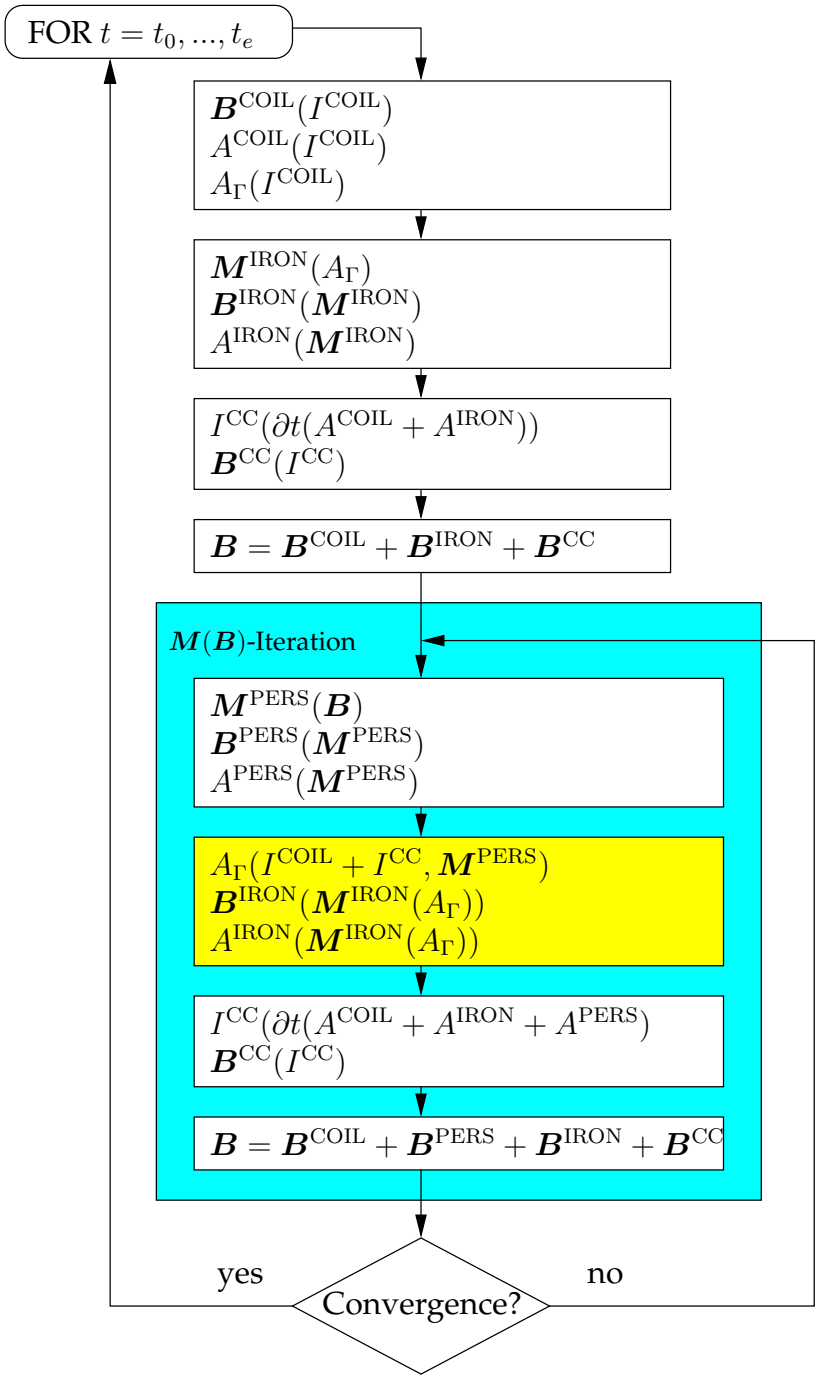

Figure 9.5.2 Hypothesis of ROXIE M(B) iteration with coupling currents

Chapter 10

Conclusions

Time transient behaviour of superconducting magnets are dominated by eddy currents effects. They are responsible of heat losses, field errors and maximum field achievable. They depend linearly on the inverse of contact resistances that have a strong random component which cannot be easily controlled and measured. This characteristic affects the reproducibility of magnet behaviour and it is problem for accelerator functioning.

A network model for calculation of eddy currents has been implemented. Contact resistances (cross and adjacent) can be assumed constant or randomly distributed. The inductive effects modelling needs to be robust and fast due to the high number of branches . A new formula for self inductance for a round wire, accurate for every length, has been found.

The network of lumped elements is solved using mesh methods formulated using a matrix approach. In this way calculations of the solving system for mesh currents and the passage to the branch currents involves only matrix multiplication. Such multiplications are highly optimised using a sparse matrix storage scheme and optimised routines. Moreover this approach leads easily to a spectral analysis diagonalising the mesh resistance matrix and time constant matrix. With spectral analysis is possible to calculate the current density field of the modes (called also eigen-currents), their time constants or their impedance and their excitation voltages. The magnetic flux linked with loops is calculated using vector potential integration over the path closed by the mesh. The integration is performed directly by the mesh matrix multiplication that sums the contribution of each branch to the closed part integral. Gauge ambiguity is thus eliminated.

Network of lumped elements for a straight wire is built from the geometric data: cable position, number of strands, width, heights, length. Any disposition on the cable in the space can be used if the node position

is given. The natural application is the study of eddy currents in coil ends.

Spatial periodic boundary conditions can be applied in order to modelize an infinitly long cable. When we study only one band of the cable, we call this kind analysis 2D because the third dimension effects due his infinity are neglected. Nevertheless when spatial periodic boundary conditions are applied to a sample longer than one band, new dynamics appear. This dynamics is exploited by means of spectral analysis that reveals the existence of zero impedance modes. These modes exist due to the fact that eddy currents can close to the infinity a thus can flows only on strands. Considering that a cable can be made hundred of meters long the infinite length hypothesis it is not so far from reality. Experience confirms this behaviour and very long currents loops with very long time constants can be exited in magnets in which the loops produce their effects: decay, ramp rate dependence of quench current, periodic patterns of magnetic fields components.

As example, studies on single cables and magnets are performed. For a single cable are showed results for steady state and transient 2D, transient 3D, steady state spectral analysis and random effects analysis. For magnets cross section are performed steady state 2D analysis.

The code developed in this thesis is integrated in ROXIE program. ROXIE is used at CERN and in other laboratory as an integrate tool for magnet design and analysis.

The integration in ROXIE will permit new studies of the interaction between eddy currents and persistent current responsible of the so called decay and snapback, the study of eddy currents in coil ends, and a finer validation of network model for eddy currents. Nevertheless the greatest advantage will be the possibility of taking into account the eddy currents effects in magnet design process.

Appendix A

Self Inductance Calculation

As seen in chapter 7.4.3 we have to solve the integral

$$I = \frac{1}{S^2}\int_V \int_V \frac{1}{r_{ij}} dV_i dV_j, \tag{A.1.1}$$

where V_i, V_j are the same cylinder of surface S, radius r, length l and $r_{ij} = |\boldsymbol{r}_i - \boldsymbol{r}_j|$ is the distance of two points in the cylinder.

The integral I has a singular volume such that $r_{ij} = 0$. We can calculate the value of the integral in the singular volume evaluating the integral in the ipervolume $r_{ij} < \delta$ and calculating the limit for $\delta \to 0$.

$$I_\delta = \frac{1}{S^2}\int_V \int_0^\delta \frac{1}{\rho}\rho^2 \sin(\vartheta) d\rho d\vartheta d\varphi dV_i = 2\pi\delta^2 \frac{l}{S} \xrightarrow{\delta\to 0} 0, \tag{A.1.2}$$

We can perform an double integration on the longitudinal axe of the cylinder

$$\begin{aligned} I &= \frac{1}{S^2}\int_S \int_S \int_0^l \int_0^l \frac{1}{\sqrt{d^2 + (l_i - l_j)^2}} dl_i dl_j dS_i dS_j = \\ &= \frac{2l}{S^2}\int_S \int_S F(l/d) dS_i dS_j, \end{aligned} \tag{A.1.3}$$

where d is the distance of two points in the surface S and

$$F(a) = \log\left(a + \sqrt{1 + a^2}\right) - \sqrt{1 + \frac{1}{a^2}} + \frac{1}{a}, \tag{A.1.4}$$

If S is a circle of radius r, $I/2l$ will depends on only r/l because is the only adimensional variable that can be constructed with r and l. In analogy with the geometric mean distance we can write

$$\frac{I}{2l} = F\left(\frac{l}{d_e}\right) \tag{A.1.5}$$

where $d_e = K(l/r)r$

For solving I for every r and l we need to find the function $K(l/r)$ that can be found solving the equation

$$\frac{1}{S^2}\int_S\int_S F(a)dS_i dS_j = F(b) \tag{A.1.6}$$

where $a = l/d$ and $b = l/(Kr)$.

If we use polar coordinate we can write

$$\frac{1}{(\pi r^2)^2}\int_0^r\int_0^{2\pi}\int_0^r\int_0^{2\pi} F(a)\rho_i\rho_j d\vartheta_i d\rho_i d\vartheta_j d\rho_j = F(b) \tag{A.1.7}$$

with

$$a = \frac{l}{d} = \frac{l}{\sqrt{\rho_i^2 + \rho_j^2 - 2\rho_i\rho_j\cos(\vartheta_i - \vartheta_f)}} \tag{A.1.8}$$

and

$$b = \frac{l}{d_e} = \frac{l}{Kr}. \tag{A.1.9}$$

We know that

$$\lim_{l/r\to\infty} K(l/r) = \frac{1}{S^2}\int_S\int_S \log(d/r)dS_i dS_j = \frac{1}{\sqrt[4]{e}}. \tag{A.1.10}$$

The numerical evaluation of the integral (A.1.8) or (A.1.10) can be approximated in:

$$\begin{aligned}&\frac{1}{(\pi r^2)^2}\int_0^r\int_0^{2\pi}\int_0^r\int_0^{2\pi} f\Big(d\big(\rho_i,\vartheta_i,\rho_j,\vartheta_j\big)\Big)\rho_i d\rho_i d\vartheta_i\rho_j d\rho_j d\vartheta_j \approx \\ &\frac{1}{\pi^2 r^4}\sum_{n_1=1}^{N_\rho}\sum_{n_2=1}^{N_\vartheta}\sum_{n_3=1}^{N_\rho}\sum_{n_4=1}^{N_\vartheta} f\Big(d\big(\bar\rho(n_1),\bar\vartheta(n_2),\bar\rho(n_3),\bar\vartheta(n_4)\big)\Big)S(n_1)S(n_3),\end{aligned} \tag{A.1.11}$$

where

$$\begin{aligned}\rho(n) =& r\frac{n}{N_\rho}\\ \bar\rho(n) =& \frac{\rho(n)+\rho(n-1)}{2} = r\frac{2n-1}{2N_\rho}\\ \vartheta(n) =& 2\pi\frac{n}{N_\vartheta}\\ \bar\vartheta(n) =& \frac{\vartheta(n)+\vartheta(n-1)}{2} = 2\pi\frac{2n-1}{2N_\vartheta}\\ S(n) =& \bar\rho(n)\big(\rho(n)-\rho(n-1)\big)\big(\vartheta(n^*)-\vartheta(n^*-1)\big) = \bar\rho(n)\frac{r}{N_\rho}\frac{2\pi}{N_\vartheta}.\end{aligned} \tag{A.1.12}$$

In other words the integral is the average of the function in the iper surface. The use of polar coordinate render necessary the weights $S(n)$. In the figure A.1.1 there is a sketch of the dicretization of the circle.

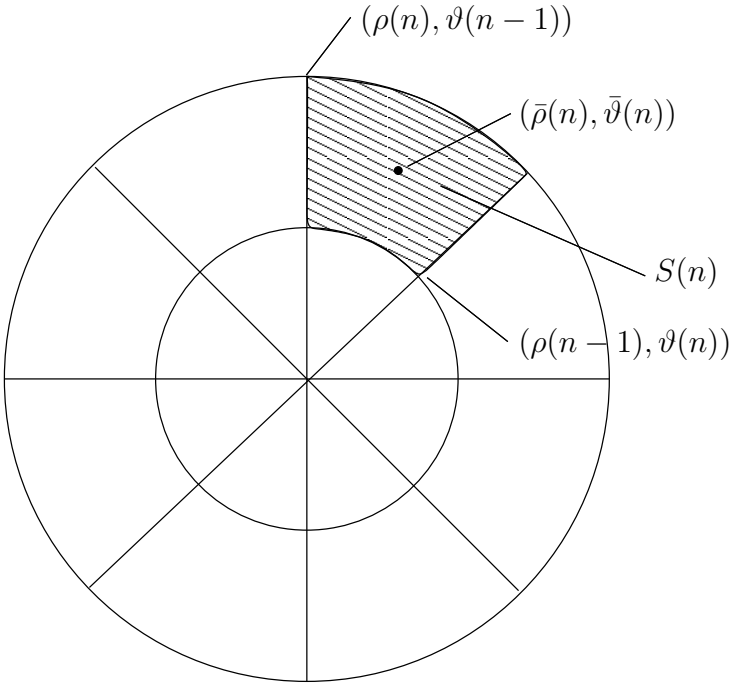

Figure A.1.1 Discrete circle for numerical integration.

In order to avoid the singular points, the point are kept out of phase by a value $\Delta\vartheta/N_\vartheta$ that goes to zero when the number of points goes to infinity. The value of $\Delta\vartheta$ it is chosen to make the results for great l be equal to the analytic formula.

The results of this procedure are confronted with numerical value obtained from Mathematica Softare using a pseudo Montecarlo method. There is agreement between the two methods. Nevertheless it is not clear how the singularity treatment can influence the final results, in particular for the limit of l/r to 0. For this case there is no analytical calculation that can confirm the result.

Appendix B

LHC current cycle

LHC current cycle is made of four segment (see [SAB+01], [SBBE02]): parabolic, exponential, linear, parabolic (PELP). It is defined from the parameters:

- T_i: initial time;
- I_i: starting current;
- I_f: final current;
- A: acceleration;
- D: deceleration;
- R: ramp rate;
- T_e: exponential starting time.

The exponential segment makes the sextupole components constant and the parabolic deceleration avoid overshoots to the power supply.

The first segment accelerate at the time T_i from a flat plateau at I_i with a parabolic function:

$$I_a(t) = \frac{A}{2}(t - Ti)^2 + I_i. \tag{B.1.1}$$

The first segment stop at T_e when the exponential segments starts. Its function is:

$$I_e(t) = ae^{bt}. \tag{B.1.2}$$

The segments are and have their derivative continuous. Thus

$$\begin{aligned} I_e(T_e) =& I_a(T_e) \\ I'_e(T_e) =& I'_a(T_e), \end{aligned} \tag{B.1.3}$$

this implies

$$\begin{aligned} b &= I_a'(T_e)/I_a(T_e) \\ a &= I_a(T_e)/e^{bT_e}. \end{aligned} \tag{B.1.4}$$

The exponential segment stops when it reaches the ramp rate R. Thus

$$I_e'(t_l) = R \quad \Rightarrow \quad t_l = \frac{1}{b}\log\left(\frac{R}{ab}\right). \tag{B.1.5}$$

If there is no exponential, conventionally $T_e = 0$, then t_l is such that the parabolic segment reaches the ramp rate R, that is

$$I_a'(t_l) = R \quad \Rightarrow \quad t_l = R/A + T_i. \tag{B.1.6}$$

Resuming:

$$t_l = \begin{cases} \frac{1}{b}\log\left(\frac{R}{ab}\right) & \text{if } T_e \neq 0, \\ \frac{R}{A} + T_i & \text{if } T_e = 0. \end{cases} \tag{B.1.7}$$

The last case defines the upper limit of the exponential starting time:

$$T_i \leq T_e \leq \frac{R}{A} + T_i \tag{B.1.8}$$

The linear segment has the equation

$$I_l(t) = R(t - t_l) + i_l, \tag{B.1.9}$$

where I_l is defined by the continuity, that is

$$i_l = \begin{cases} I_e(t_l) & \text{if } T_e \neq 0, \\ I_a(t_l) & \text{if } T_e = 0. \end{cases} \tag{B.1.10}$$

When the linear ramp approaches to I_f begins the parabolic deceleration defined by:

$$I_d(t) = -\frac{D}{2}(t_f - t)^2 + I_f, \tag{B.1.11}$$

where t_f is the final time. The parabolic deceleration starts at t_p in order to match the ramp rate. These time is related to the final time by:

$$t_f = t_d + D/R. \tag{B.1.12}$$

The parabolic deceleration time is defined by the continuity:

$$I_l(t_p) = I_d(t_p) \quad \Rightarrow \quad t_d = \frac{I_f - i_l}{R} + t_l - \frac{R}{2D}. \tag{B.1.13}$$

.

Resuming the new parameters that let a complete description of the current cycle are:

- $Ia(Te) = \frac{A}{2}(Te - Ti)^2 + I_i$: acceleration final current;
- $Ia'(Te) = A(Te - Ti)$: acceleration derivative final current;
- $b = I'_a(T_e)/I_a(T_e)$: exponential parameter;
- $a = I_a(T_e)/e^{bT_e}$: exponential parameter;
- $t_l = \frac{1}{b}\log\left(\frac{R}{ab}\right)$ if $T_e \neq 0$ or
  $t_l = \frac{R}{A} + T_i$ if $T_e = 0$: linear ramp starting time;
- $i_l = e^{bt_l}$ if $T_e \neq 0$ or
  $i_l = \frac{A}{2}(t_l - Ti)^2 + I_i$ if $T_e = 0$: linear ramp starting current;
- $t_d = \frac{I_f - i_l}{R} + t_l - \frac{R}{2D}$: deceleration starting time;
- $t_f = t_d + D/R$: deceleration final time.

and the function is:

$$I(t) = \begin{cases} I_i & \text{if } t < T_i, \\ \frac{A}{2}(t - Ti)^2 + I_i & \text{if } T_i \leq t < T_e, \\ ae^{bt} & \text{if } T_e \leq t < t_l, \\ R(t - t_l) + i_l & \text{if } t_l \leq t < t_d, \\ -\frac{D}{2}(t_f - t)^2 + I_f & \text{if } t_d \leq t < t_f, \\ I_f & \text{if } t \geq t_f. \end{cases} \tag{B.1.14}$$

Bibliography

[ABB+00] A. Akhmetov, I. Balaazi, L. Bottura, M. Gateau, and L. Walckiers. Energy loss in mbsmt7/v1 short dipole magnet at 1.8 k for different current cycles and parameters of the power supply. *CERN internal note*, LHC-MTA-IN-2000-120, 2000.

[ABB01] A. Akhmetov, L. Bottura, and M. Breschi. A continuum model for current distribution in rutherford cables. *IEEE Transactions on Applied Superconductivity*, 11(1):2138–2141, 2001.

[ABBR00] A. Akhmetov, L. Bottura, M. Breschi, and P. L. Ribani. A theoretical investigation on current imbalance in flat two-layer superconducting cables. *Cryogenics*, 40(8-10):627–635, 0 2000.

[ADMS93] A. A. Akhmetov, A. Devred, R. Mints, and R. Schermer. Current loop decay in rutherford-type cables. *Superconducting Super Collider Laboratory*, 485, 5 1993.

[ADO94] A. A. Akhmetov, A. Devred, and T. Ogitsu. Periodicity of crossover currents in a rutherford-type cable subjected to a time-dependent magnetic field. *Journal of Applied Physics*, 75(6):3176–3183, 1994.

[AIS98] A. A. Akhmetov, S. S. Ivanov, and I. O. Shchegolev. The network approach to calculation of characteristic time constants of the flat two-layer superconducting cable. *Physica C: Superconductivity*, 310(1-4):382–386, 12 1998.

[Akh98] A. A. Akhmetov. Network models of superconducting cables and the results of the matrix approach to their description. *Physica C: Superconductivity*, 310(1-4):309–315, 12 1998.

[Akh00a] A. A. Akhmetov. Compatibility of two basic models describing the a.c. loss and eddy currents in flat superconducting cables. *Cryogenics*, 40(7):445–457, 2000.

[Akh00b] A. A. Akhmetov. Further analysis of the eigen-frequency spectrum of a flat two-layer superconducting cable. *Supercond. Sci. Technol.*, 13:127–133, 2000.

[Akh01] A. A. Akhmetov. General 2d equation for coupling currents in a flat superconducting cable subjected to a time-dependent magnetic field in the face-on orientation. *Cryogenics*, 41(9):649–655, 9 2001.

[Akh02] A. A. Akhmetov. Ac loss in a stack of flat superconducting cables. *IEEE Transactions on Applied Superconductivity*, 12(1):1595–1598, 2002.

[AKOT95] A. A. Akhmetov, K. Kuroda, K. Ono, and M. Takeo. Eddy currents in flat two-layer superconducting cables. *Cryogenics*, 35(8):495–504, 8 1995.

[BBF03] L. Bottura, M. Breschi, and M. Fabbri. An analytical benchmark for the calculation of current distribution in superconducting cables. *Cryogenics*, 43(3-5):241–248, 0 2003.

[BBR03] L. Bottura, M. Breschi, and C. Rosso. Analysis of electrical coupling parameters in superconducting cables. *Cryogenics*, 43(3-5):233–239, 0 2003.

[BBSS02] L. Bottura, M. Buzio, P. Schnizer, and N. Smirnov. A tool for simulating rotating coil magnetometers. *IEEE Transactions on Applied Superconductivity*, 12(1):1680–1683, 2002.

[BGK+91] H. Bruck, D. Gall, J. Krzywinski, R. Meinke, H. Preissner, M. Halemeyer, P. Schmuser, C. Stolzenburg, R. Stiening, D. ter Avest, and L.J.M. van de Klundert. Observation of a periodic pattern in the persistent-current fields of the superconducting hera magnets. In *Proceedings of IEEE Particle Accelerator Conference*, 1991.

[BRB00] L. Bottura, C. Rosso, and M. Breschi. A general model for thermal, hydraulic and electric analysis of superconducting cables. *Cryogenics*, 40(8-10):617–626, 0 2000.

[BRR79] P. A. Brennan, N. Raver, and A. E. Ruehli. Three-dimensional inductance computations with partial element equivalent circuits. *IBM Journal of Research and Development*, 23(6):661, 1979.

[BRW+95] J. Buckley, D. Richter, L. Walckiers, R. Wolf, and A. Verweij. Dynamic magnetic measurements of superconducting magnets for the lhc. *IEEE Transactions on Applied Superconductivity*, 5(2):1024–1027, 1995.

[BWA97] L. Bottura, L. Walckiers, and Z. Ang. Experimental evidence of boundary induced coupling currents in prototypes. *IEEE Transactions on Applied Superconductivity*, 7(2):801–804, 1997.

[Cam80] A. M. Campbell. ac losses in cables of twisted multifilment superconductors. *Cryogenics*, 20(11):651–654, 11 1980.

[Cam81] A. M. Campbell. The effect of transport current and saturation on the losses of multifilamentary superconducting wires. *Cryogenics*, 21(2):107–112, 2 1981.

[Cam82] A.M. Campbel. A general treatment of losses in multifilamentary supeconductors. *Cryogenics*, 22:3–16, 1982.

[Car75] W. J. Jr. Carr. Conductivity, permeability, and dielectric constant in a multifilament superconductor. *Journal of Applied Physics*, 46(9):4043–4047, 09 1975.

[Car77] W. J. Jr. Carr. Longitudinal and transverse field losses in multifilament superconductors. *IEEE Transactions on Magnetics*, 13(1):192–197, 1977.

[Car04] W. J. Jr. Carr. Calculation of the surface charge on a circular type-ii superconducting wire carrying transport current. *Physica C: Superconductivity*, 402(3):293–302, 2 2004.

[CWM75] W. J. Jr. Carr, M. S. Walker, and J. H. Murphy. Alternating field loss in a multifilament superconducting wire for weak ac fields superposed on a constant bias. *Journal of Applied Physics*, 46(9):4048–4052, 09 1975.

[DO95] A. Devred and T. Ogitsu. Influence of eddy currents in superconducting particle accelerator magnets using rutherford-type cables. *CAS-CERN Accelerator School : Superconductivity in Particle Accelerators*, pages 93–122, 1995.

[Gro46] Frederick W. Grover. *Inductance Calculations*. Dover, 1946.

[HKdO+01] M. Haverkamp, A. Kuijper, A. den Ouden, B. ten Haken, L. Bottura, and H. H. J. ten Kate. Interaction between current imbalance and magnetization in lhc cables. *IEEE Transactions on Applied Superconductivity*, 11(1):1609–1612, 2001.

[HSS03] C. Harlander, R. Sabelka, and S. Selberherr. Efficient inductance calculation in interconnect structures by applying the monte carlo method. *Microelectronics Journal*, 34(9):815–821, 9 2003.

[Kam98] Mattan Kamon. *Fast Parasitic Extraction and Simulation of Three-dimensional Interconnect via Quasistatic Analysis*. PhD thesis, Massachusetts Institute of Technology, 1998.

[KS95] L. Krempasky and C. Schmidt. Theory of "supercurrents" and their influence on field quality and stability of superconducting magnets. *Journal of Applied Physics*, 78(9):5800–5810, 1995.

[KS96] L. Krempasky and C. Schmidt. Ramp-rate limitation in large superconducting magnets due to "supercurrents". *Cryogenics*, 36(6):471–483, 6 1996.

[Mes96] Karl Hubert Mess. *Superconducting Accelerator Magnets*. World Scientific, 1996.

[Mor73] G. H. Morgan. Eddy currents in flat metal-filled superconducting braids. *Journal of Applied Physics*, 44(7):3319–3322, 1973.

[MS96] G. Martinelli and M. Salerno. *Fondamenti di elettrotecnica*. Siderea, 1996.

[PTVF01] W. H. Press, S.A. Teukolsky, W. T. Vetterling, and B. P. Flannery. *Numerical recipes*. Cambridge University Press, 2001.

[Rue74] A. E. Ruehli. Equivalent circuit models fir three-dimensional multiconductor systems. *IEEE Transactions on Microwave Theory and Techniques*, 22(3):216–221, 1974.

[Rus99] S. Russenschuck. Roxie : routine for the optimization of magnet x-sections, inverse field calculation and coil end design.

In *1st International Roxie Users Meeting and Workshop*. CERN, 1999.

[Saa96] Yousef Saad. *Iterative Methods for Sparse Linear System*. PWS Publishing Co., 1996.

[SAB+01] S. Sanfilippo, A. Akhmetov, L. Bottura, M. Buzio, M. Gateau, F. Patru, N. Smirnov, and L.Walckiers. Magnetic measurements for 15 m long dipoles - standard program of cold tests. *CERN internal note*, MTA-IN-2001-169, 2001.

[SBBE02] S. Sanfilippo, L. Bottura, M. Buzio, and E. Effinger. Magnetic measurements for 15-m long dipoles - extended program of tests. *CERN internal note*, MTA-IN-2002-183, 2002.

[SM97] M. Shimada and N. Mitchell. Simulation of the iter-cs coil operation including the effect of the ramp rate limitation. *IEEE Transactions on Applied Superconductivity*, 7(2):759–762, 6 1997.

[Tur74] B. Turck. Influence of a transverse conductance on current sharing in a two-layer superconducting cable. *Cryogenics*, 14(8):448–454, 8 1974.

[Ver95] Arjan Verveij. *Electrodynamics of superconducting cables in accelerator magnets*. PhD thesis, Twente University, 1995.

[VtK95] A. P. Verweij and H. H. J. ten Kate. Super coupling currents in rutherford type of cables due to longitudinal nonhomogeneities of db/dt. *IEEE Transactions on Applied Superconductivity*, 5(2):404–407, 1995.

[VtKL+95] A. P. Verweij, H. H. J. ten Kate, D. Leroy, L. Oberli, and A. Siemko. Ramp rate induced quenches in the one-metre dipole model magnets for the. *IEEE Transactions on Applied Superconductivity*, 5(2):1020–1023, 1995.

[Wil97] M. N. Wilson. Superconducting magnets for accelerators: a review. *IEEE Transactions on Applied Superconductivity*, 7(2):727–732, 1997.

[WLR+97] R. Wolf, D. Leroy, D. Richter, A. Verweij, and L Walckiers. Determination of interstrand contact resistance from loss and field measurements in lhc dipole prototypes and correlation with measurements on cable samples. *IEEE Transactions on Applied Superconductivity*, 7(2):797–800, 1997.

[XD98] S. Li Xiaoye and J. W. Demmel. Making sparce gaussian elimination scalable by static pivoting. In *Proceedings of SC 98*, 1998.